INSTYTUT FIZYKI JĄDROWEJ
IM. HENRYKA NIEWODNICZAŃSKIEGO
POLSKIEJ AKADEMII NAUK

# Theory and phenomenology of transverse momentum dependent parton distribution functions

written
by

Tomoki Goda

under the supervision
of
dr hab. Sebastian Sapeta

submitted in the process of seeking for a degree
of
Doctor of Philosophy
at
Instytut Fizyki Jądrowej
im. Henryka Niewodniczańskiego Polskiej Akademii Nauk

# Contents

## Streszczenie

Chromodynamika Kwantowa (*Quantum Chromodynamics, QCD*) została zaproponowana jako teoria oddziaływań silnych w latach 1972-1973 i przez następne pięćdziesiąt lat była intensywnie testowana w eksperymentach. Prawdopodobnie najbardziej intrygującymi własnościami QCD są *uwięzienie kwarków* i *asymptotyczna swoboda*. Pierwsza z nich oznacza, że naładowane kolorowo stopnie swobody teorii nie mogą być wyizolowane. Druga własność sprawia, że oddziaływania między kwarkami i gluonami stają się słabsze wraz ze wzrostem skali energetycznej. Powyższe cechy QCD w sposób naturalny doprowadziły do badania silnych oddziaływań w granicy wysokich energii, w której stosowane może być podejście perturbacyjne (pQCD). W ciągu kilku minionych dekad prowadzone były liczne badania w takich eksperymentach jak Stanford Linear Accelerator Center (SLAC), Hadron–Electron Ring Accelerator (HERA) w DESY, Large Hadron Collider (LHC) w ośrodku CERN, i wielu innych. Obecnie, w fazie planowania i konstrukcji znajduje się nowy akcelerator Electron-Ion Collider (EIC), zlokalizowany Brookhaven National Laboratory (BNL) w USA.

Jednym z głównych celów wymienionych wyżej badań jest poznanie i zrozumienie struktury hadronów, w szczególności protonu. Mimo, że obiekty te posiadają immanentny składnik nieperturbacyjny, związany z uwięzieniem koloru, dzięki teoriom faktoryzacyjnym efekty te mogą być wyizolowane i zmierzone. Co więcej, własności hadronów mogą być badane w znaczniej mierze przy pomocy metod perturbacyjnej QCD, dzięki równaniom ewolucji mających swe źródło w resumacji dużych logarytmów. W perturbacyjnej Chromodynamice Kwantowej obliczane są tzw. elementy macierzowe, rząd po rzędzie w rozwinięciu względem silnej stałej sprzężenia $\alpha_s$. Podczas gdy wiodący rząd takiego rozwinięcia może dać pewien wgląd w dany proces, zazwyczaj konieczne jest liczenie kolejnych rzędów. Złożoność rachunków w wyższych rzędach wzrasta jednak eksponencjalne i niezbędne staje się używanie algorytmów zaimplementowanych w formie programów komputerowych.

Podsumowując, badania struktury protonu związane są z dwoma aspektami: perturbacyjnym i nieperturbacyjnym. Efekty nieperturbacyjne opisywane są zwykle przy pomocy modeli fenomenologicznych, których parametry ustalane są przez fity do danych eksperymentalnych. Podejście perturbacyjne natomiast pozwala na zrozumienie wielu cech protonu, takich jak zależność od twardej skali, poprzez systematyczne rozwinięcie w stałej sprzężenia. Istotne jest jednak, że opis danych doświadczalnych nie może być kompletny bez uwzględnienia obu z powyższych aspektów. Modele fenomenologiczne są zazwyczaj prostsze niż rachunki perturbacyjne ale obydwa podejścia są do siebie komplementarne.

Niniejsza rozprawa doktorska oparta jest na badaniach przeprowadzonych przeze

mnie we współpracy z osobami wymienionymi poniżej i bazuje na następujących oryginalnych publikacjach:

- **"Sector Decomposition Scheme for N$^3$LO Beam Function"**
  T. Goda and P. Müllender
  Acta Phys. Polon. B, vol. 52, no. 8, p. 947, 2021

- **"Sudakov effects and the dipole amplitude"**
  T. Goda, K. Kutak and S. Sapeta,
  Nucl. Phys. B, vol. 990, p. 116155, 2023

- **"Effects of gluon kinematics and the Sudakov form factor on the dipole amplitude"**
  T. Goda, K. Kutak and S. Sapeta
  arXiv:2305.14025, wysłane do European Physical Journal C

Badania przedstawione w rozprawie przeprowadzone zostały zasadniczo w dwóch obszarach w ramach QCD: efektywnej teorii miękkich i kolinearnych gluonów (*Soft-Collinear Effective Theory, SCET*) oraz obszaru kinematycznego w którym dominują partony niosące mały ułamek, $x$, całkowitego pędu protonu. Pierwszy artykuł na powyższej liście publikacji zawiera badania w ramach SCET a dwa pozostałe dotyczą fizyki małych $x$.

Prezentowana rozprawa posiada następującą strukturę. W rozdziale pierwszym dyskutowane są zagadnienia istotne dla obu z wyżej wymienionych obszarów. Celem tego rozdziału jest wyjaśnienie kluczowych pojęć i ustalenie notacji. W drugiej części rozdziału pierwszego skupiamy się na bardziej szczegółowym wprowadzeniu do zagadnień badanych w kolejnych rozdziałach.

Drugi rozdział poświęcony jest badaniom funkcji beam w rzędzie N$^3$LO. Kluczowym dla tego zagadnienia problemem jest zrozumienie skomplikowanej struktury rozbieżności podczerwonych oraz efektywna ich ekstrakcja. Dwa wprowadzone w tym celu narzędzia to tzw. *selector functions* oraz rozkład na sektory. W rozdziale drugim przedstawiony jest kompletny algorytm umożliwiający wykonywanie wszystkich całek pojawiających się rachunku funkcji beam w rzędzie N$^3$LO. Algorytm jest następnie przetestowany i użyty do wyliczenia części biegunowej powyższej funkcji.

Trzeci rozdział rozprawy skupia się na dwóch zagadnieniach z obszaru fizyki małych $x$. Badania te przeprowadzane zostały w ramach modeli saturacyjnych, które w niniejszej pracy zostały rozszerzone poprzez dodanie ważnych efektów fizycznych. Pierwszym z nich był czynnik Sudakova, który został włączony do dwóch znanych modeli przekrojów dipolowych tzw. modeli Golec-Biernat–Wüstoff (GBW) i Bartels–Golec-Biernat–Kowalski (BGK). W drugiej części rozdziału dyskutujemy natomiast znaczenie dokładnej kinematyki w ramach faktoryzacji wysokich energii. Pokazujemy, że jej uwzględnienie ma znaczenie dla opisu danych oraz używamy tak rozszerzonych modeli do wyliczenia przewidywań dla projektowanego obecnie akceleratora EIC. Rozprawa zakończona jest podsumowaniem oraz trzema dodatkami.

## Abstract

Quantum Chromodynamics (QCD) was proposed as a theory of strong interactions in the years 1972-1973 and, for over the next fifty years, it has been tested extensively in experiments. Probably the most puzzling and characteristic of QCD are the *confinement* and *asymptotic freedom*. The former means that colour-charged degrees of freedom of the theory cannot be isolated, while the latter causes interactions to become weaker as a relevant energy scale increases. These features of QCD naturally led to studying strong interactions in the high energy limit, in which perturbation theory (pQCD) is applicable. In the last several decades, numerous international efforts have been made, most notably at the Stanford Linear Accelerator Center (SLAC), Hadron–Electron Ring Accelerator (HERA) at DESY, and the Large Hadron Collider (LHC) at CERN, among others. A new accelerator, Electron-Ion Collider (EIC), is currently under development at the Brookhaven National Laboratory (BNL).

One of the main objectives of these studies is to reveal the structure of hadrons, particularly the proton. While QCD is inherently non-perturbative due to colour-confinement, factorization theorems allow the non-perturbative effects to be isolated and measured. Although the hadron structure involves a non-perturbative component, its behaviour can still be studied in pQCD, most importantly via resummation of large logarithms. In perturbative QCD, one computes operator matrix elements, order by order in the strong coupling constant, $\alpha_s$. While the leading order (LO) approximation may give some insights into the processes, it is also important to go beyond. However, such computations become exponentially complex as the orders increase and use of automated algorithms implemented in computer programs is indispensable.

To summarize, the study of the proton structure has two aspects: perturbative and non-perturbative. On the non-perturbative side, models are built and fitted to experimental data. On the perturbative side, some specific behaviours, for example, the hard-scale dependence can be studied by calculating series expansion in the strong coupling constant. As we discuss in this thesis, descriptions of experimental data is incomplete, if either of the above aspects is missing. In general, phenomenological models are much simpler to implement than perturbative calculations, while perturbative calculations are more precise, and they can motivate some specific forms of models. Therefore it is important to approach the problem of hadron structure from both sides.

This thesis is based on the research conducted by myself in collaboration with people listed below. The list of the original publications is as follows:

- **"Sector Decomposition Scheme for N$^3$LO Beam Function"**
  T. Goda and P. Müllender
  Acta Phys. Polon. B, vol. 52, no. 8, p. 947, 2021

- **"Sudakov effects and the dipole amplitude"**
  T. Goda, K. Kutak and S. Sapeta,
  Nucl. Phys. B, vol. 990, p. 116155, 2023

- **"Effects of gluon kinematics and the Sudakov form factor on the dipole amplitude"**

T. Goda, K. Kutak and S. Sapeta
arXiv:2305.14025, submitted to European Physical Journal C

The research presented in this thesis involves two distinct areas of QCD, namely the field of Soft-Collinear Effective Theory (SCET), and the field of small-$x$ physics. The first item in the above list of publications belongs to the former, while the rest of the items belong to the latter.

The structure of the thesis is as follows. In the first chapter, we discus general topics which are related to both of the above fields, intended to outline some basic concepts and fix terminology and notation. In the latter half of the first chapter, we discuss in depth, the issues relevant for the specific problems.

The second chapter is devoted to studies of the calculative techniques for the $\mathrm{N^3LO}$ beam functions. In this chapter, two main ideas are introduced: selector functions and sector decomposition. A complete algorithm for calculation of phase space integrals appearing at $\mathrm{N^3LO}$ is presented and successfully used to compute the pole part of the $\mathrm{N^3LO}$ beam functions.

The third chapter is devoted to the two projects in the area of small-$x$ physics. Since they share some common background, the introductory part, which is focused on specific models of the dipole cross section, is be given jointly for the two studies. After the introductory sections, we discuss effects of the Sudakov form factor on the dipole cross section models, with special reference to the Golec-Biernat–Wüstoff (GBW) and Bartels–Golec-Biernat–Kowalski (BGK) models. Finally, in the latter part of the chapter, effects of exact gluon kinematics in the $k_T$-factorization formula of the $F_2$ structure function are investigated in the context of the aforementioned models. These effects which are reflected in the fit parameters of the models, along with the Sudakov form factor, are further studied in the context of the future Electron-Ion Collider. The thesis is concluded by the summary chapter, which is followed by appendices.

# Acknowledgement

I would like to express my deepest gratitude to my supervisor, dr hab. Sebastian Sapeta, for his support and numerous invaluable pieces of advice. I am also indebted to every member of the division of theoretical physics at Institute Fizyki Jądrowej, and people with whom I had the pleasure to collaborate. In particular, I would like to thank prof. Michał Czakon, prof. Krzysztof Kutak and Philipp Müllender for collaboration, discussions and many insightful comments over the course of my studies. I would also like to thank Rajeev Singh and Etienne Blanco for all the encouragement. Without the support of my family and friends I would have not been able to carry out the research I am presenting in this thesis.

# Chapter 1

# Introduction to the structure of the proton

## 1.1 QCD summary

Let us first summarize the fundamentals of Quantum Chromodynamics (QCD). It extracts essential parts from Refs. [1–6] related to the following sections and thus the references will not be given unless necessary. Throughout this thesis, $\hbar = c = 1$ is to be understood.

There are four fundamental forces in Nature, namely electromagnetic, weak, strong, and gravitational. In the short scale ($\sim 1\ \mathrm{GeV}^{-1}$) physics, the strong force dominates over other forces by orders of magnitude. QCD is a field theory which describes strong interactions of quarks, $q$, and their corresponding anti-particles, antiquarks, $\overline{q}$. The force is mediated by gluons, $g$.

The QCD Lagrangian reads

$$\mathcal{L}_{\mathrm{QCD}} = \sum_f \overline{\psi}_{f\,i} \left( i \not{\partial} - m_f \right)_{ij} \psi_{f\,j} + \frac{1}{4} F^{a\mu\nu} F^a_{\mu\nu}, \tag{1.1}$$

for the quarks of flavour $f \in \{u, d, s, c, b, t\}$, represented by $\psi_f$, and the gluons described by the field $A$, for which the covariant derivative and field strength tensor are given as

$$D_{\mu\,ij} = \delta_{ij}\partial_\mu - i g_s A^a_\mu t^a_{ij}, \tag{1.2}$$

$$F^a_{\mu\nu} = \partial_\mu A^a_\nu - \partial_\nu A^a_\mu + g f^{abc} A^b A^c, \tag{1.3}$$

and the quark mass $m_{q\,ij} = \delta_{ij} m_q$. Generators of the SU(3) Lie group, $t^a = \lambda_a/2$, where $\lambda_a$ are the Gell-Mann matrices, satisfy the commutation relation

$$\left[ t^a, t^b \right] = i f^{abc} t^c, \tag{1.4}$$

where $f_{abs}$ are totally antisymmetric structure constants. We use the Feynman slash notation $\not{p} \equiv p^\mu \gamma_\mu$ with the Dirac gamma matrices $\gamma^\mu$.

The gauge coupling $g_s$ and mass $m_q$ are free parameters of the theory, and it is

customary to define

$$\alpha_s \equiv \frac{g_s^2}{4\pi}. \tag{1.5}$$

The third term in Eq. (1.3) defines QCD as a non-abelian gauge theory, in which gauge bosons carry the colour-charge, and interact among themselves. This additional term gives rise to the three- and four- gluon vertices. The self-interaction is one of the main differences from QED, in which photons do not interact with themselves at leading order. A consequence of this is the well-known asymptotic freedom, which will be discussed shortly.

Another notable difference from QED is the presence of colour factors appearing in the algebra of $t^a$. The colour factors, which are related to splitting probability strengths of a gluon off a quark, a gluon to two gluons, and a gluon to a quark anti-quark pair are respectively denoted by $C_F = (N_c^2 - 1)/(2N_c)$, $C_A = N_c$ and $T_F = 1/2$, for a number of colours $N_c$. While, in principle, $N_c = 3$, it is often useful to keep it free so that the large $N_c$ limit can be studied.

The Lagrangian (1.1) respects local gauge symmetry. Under the local SU(3) gauge transformation

$$U(x) \equiv e^{-i\theta_a(x)t^a}, \tag{1.6}$$

the field $A$ transforms as

$$A \to U(x)AU^\dagger(x) + \frac{i}{g}\left[\partial U(x)\right]U^\dagger(x). \tag{1.7}$$

Additionally, gauge invariance forbids mass term for the gluons $m_g^2 A_\mu^a A^{a\mu}$, and thus the gluons are massless particles, which is consistent with experimental findings.

While one can choose gauge freely, in the following sections, mostly a special class of gauges called *axial* (*physical*) *gauges* are considered. The characteristics of this gauge is that only transversely polarized gluons propagate. Consequently, the ghost field, which may be required in other gauges, is not necessary in the axial gauge. The gauge-fixing term for an axial gauge with a condition $n \cdot A^a = 0$ is given by

$$\mathcal{L}_{\text{fix}} = -\frac{1}{2\xi}(n \cdot A^a)(n \cdot A^a), \tag{1.8}$$

and, for this gauge, the gluon propagator reads

$$\frac{i}{p_i^2 \epsilon}\left(-\eta^{\mu\nu} + \frac{n^\mu p\nu + p^\mu n^\nu}{n \cdot p} - (n^2 + \xi p^2)\frac{p^\mu p^\nu}{(n \cdot p)^2}\right), \tag{1.9}$$

where, in the following chapters, a choice $n^2 = 0$ and $\xi = 0$ is understood. Since, with this choice, the vector $n^\mu$ is on the light-cone, the term *light-cone gauge* will be also used interchangeably.

Unlike in QED, the coloured objects (anti-)quarks and gluons cannot be observed as free particles. Instead, experimentally, they are observed only as constituents of colourless hadrons. This property of QCD is called *colour confinement*.

As a consequence of the self-interacting nature of the gluons, anti-screening effects

lead the coupling to run. As it will be discussed below, because of anti-screening, the partons are asymptotically free in the high-energy limit. This is a vital building block for the perturbation theory. For this reason, one categorizes QCD processes into two types: *perturbative* and *non-perturbative*. The former is computed order by order in the coupling constant $\alpha_s$, while the latter is usually modelled. A scale $\Lambda_{\mathrm{QCD}} \sim 200 - 300$ MeV denotes a characteristic scale of QCD, below which the coupling is too strong and the perturbation theory fails.

Another important concept which we will discuss in Sec. 1.2.1 is *factorization*. The main idea is to factorize a cross section into a perturbative part and non-perturbative part, such that non-perturbative effects are confined within some factors and the remaining part can be computed as a series in $\alpha_s$.

Feynman rules and Feynman diagrams, which represent interactions and propagations of particles, form one of the main tools used in perturbative calculations. It is a set of rules and diagrams.

The Feynman rules in the light-cone gauge are given as follows [1]. Firstly, the incoming quarks are expressed by Dirac spinors of following types

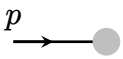


$$u(p), \qquad \overline{u}(p), \tag{1.10}$$

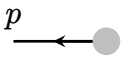


$$v(p), \qquad \overline{v}(p), \tag{1.11}$$

whereas, external gluons are expressed by the polarization vectors,

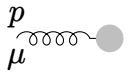


$$\epsilon^{\mu}(p), \qquad \epsilon^{*\mu}(p). \tag{1.12}$$

Quarks and gluons propagating internally are represented by the respective propagators,

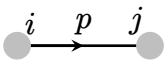


$$i\frac{(\not{p}+m)\delta_{ij}}{(p^2-m^2+i\epsilon)}, \tag{1.13}$$

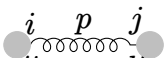


$$i\frac{\delta_{ij}}{(p^2+i\epsilon)}\left(-g^{\mu\nu}+\frac{p^{\mu}n^{\nu}+p^{\nu}n^{\mu}}{p\cdot n}\right). \tag{1.14}$$

Interactions of fields, the vertices, are given by

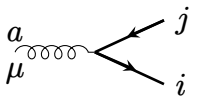


$$-ig_s t^a_{ij}\gamma^\mu, \tag{1.15}$$

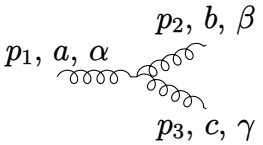


$$g_s f_{abc}\left(g^{\alpha\beta}(p_1-p_2)_\gamma + g^{\beta\gamma}(p_2-p_3)_\alpha + g^{\alpha\gamma}(p_3-p_1)_\beta\right), \tag{1.16}$$

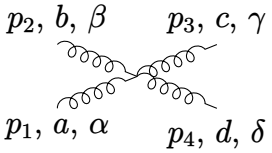


$$\begin{aligned} ig_s^2\Big(&f_{abe}f_{cde}(g^{\alpha\gamma}g^{\beta\delta}-g^{\alpha\delta}g^{\beta\gamma}) \\ &+ f_{ace}f_{dbe}(g^{\alpha\delta}g^{\beta\gamma}-g^{\alpha\beta}g^{\gamma\delta}) \\ &+ f_{ade}f_{bce}(g^{\alpha\beta}g^{\gamma\delta}-g^{\alpha\gamma}g^{\beta\delta})\Big). \end{aligned} \tag{1.17}$$

In Fig. 1.1 we show the so-called self-energy diagram, where time flows from left to right. In this diagram a quark-line, →—, emits a gluon ∿∿∿, which is absorbed back by the quark line. The letters $k$ and $l$ denote four-momenta of the particles. The corresponding scattering amplitude is given by

$$i\mathcal{M} = -g_s^2\overline{u}(l-k)\gamma^\mu t^a_{ij}\frac{1}{k^2}\left(g^{\mu\nu}-\frac{n^\mu k^\nu + k^\mu n^\nu}{n\cdot k}\right)\frac{(\not{l}-\not{k})}{(l-k)^2}\gamma^\mu t^a_{jk}u(l), \tag{1.18}$$

where we consider massless quarks and omit $i\epsilon$ in the denominator.

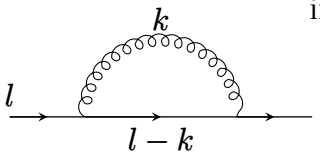


Figure 1.1: An example of self-energy "bubble" diagram.

In the diagram shown in Fig. 1.1, one encounters a loop-integral of the type (*cf.* Fig. A.1) [7]

$$I_{\text{bubble}} = \int \frac{d^4k}{k^2(k-l)^2}. \tag{1.19}$$

This integral is divergent in four dimensions. In dimensional regularization, which is commonly used in high-energy physics, the integration is performed in $d = 4-2\epsilon$ dimensions and divergences appear as poles at $\epsilon = 0$. As shown in App. A.1, the dimensionally regularized bubble integral yields [7]

$$I_{\text{bubble}} = i(-1)^{\frac{d-2}{2}}\pi^{\frac{d}{2}}\Gamma\left(2-\frac{d}{2}\right)\left(l^2\right)^{\frac{d}{2}-2}B\left(\frac{d}{2}-1,\frac{d}{2}-1\right). \tag{1.20}$$

Then, one can see that the integral is singular at $d = 4$. Additionally, one notices that

in the on-shell limit $l^2 \to 0$, the integral (1.20) vanishes. Such integrals of the form

$$\int \frac{d^d k}{k^{2n}}, \tag{1.21}$$

are called *scaleless* integrals, and they vanish in dimensional regularization [7–9].

The diagram of Fig. 1.1 gives higher-order correction to the quark propagator (1.13). As mentioned above, loop integrals are divergent in QCD. One class of the divergences is called *ultraviolet* (UV). The UV divergences, which also appear in Eq. (1.20) at $k \to \infty$ as

$$\Gamma(\epsilon) = \frac{1}{\epsilon} - \gamma_E, \tag{1.22}$$

where $\gamma_E$ is the Euler–Mascheroni constant $\approx 2.718$ are treated by *renormalization*. The renormalization procedure cancels UV divergences by multiplying the fields, the masses and the couplings in the Lagrangian by renormalization factors $Z_i$:

$$\psi_q^0 = Z_2^{1/2}\psi_q \qquad A^{0^a}_{\ \mu} = Z_3^{1/2} A^a_\mu \qquad g_s^0 = \frac{Z_1}{Z_2 Z_3}\mu^{\frac{4-d}{2}} g_s, \tag{1.23}$$

where the energy scale $\mu$ is introduced in order to keep the coupling constant dimensionless, and the superscript 0 denotes the bare objects, which were introduced in the original Lagrangian (1.1). What Eq.(1.23) effectively does is that it introduces the counter-terms which subtract the UV divergences.

The bare quantities and counter-terms are individually divergent, while their combination is finite. However, one has some freedom in choosing the coefficients of the counter-terms. One of the most popular choices is the minimal-subtraction (MS) scheme, in which only the $\epsilon$-pole terms are cancelled by the counter-terms. The modified MS scheme ($\overline{\text{MS}}$) is another popular scheme, in which the terms proportional to $1/\epsilon + \ln(4\pi) - \gamma_E$ are cancelled.

Unsurprisingly, the physical observables, such as cross sections, cannot depend on the scale $\mu$, which was introduced in Eq. (1.23). Therefore, dependences on $\mu$ which appear at intermediate steps of calculations have to cancel. The sets of equations called *renormalization group equations* (RGE) are very powerful tools based on this idea. For example, the coupling $\alpha_s$ satisfies

$$\mu^2 \frac{\partial \alpha_s}{\partial \mu^2} = \beta = -\alpha_s(\beta_0 + \beta_1 \alpha_s + \cdots), \tag{1.24}$$

where the ellipsis stands for higher orders in $\alpha_s$, and the first coefficient is

$$\beta_0 = \frac{11 C_A - 4 T_F n_f}{12\pi} = \frac{33 - 2n_f}{12\pi}. \tag{1.25}$$

It is important to note that, because the number of flavours $n_f = 6$ at most, hence $\beta < 0$. That is to say the coupling weakens as the scale rises. As previously mentioned, the colour factor $C_A$ is related to a splitting of a gluon to a pair of gluons, and thus one sees here that the asymptotic freedom, as a result of the positive term of $\beta_0$, is indeed related to the self-interacting nature of the gluons.

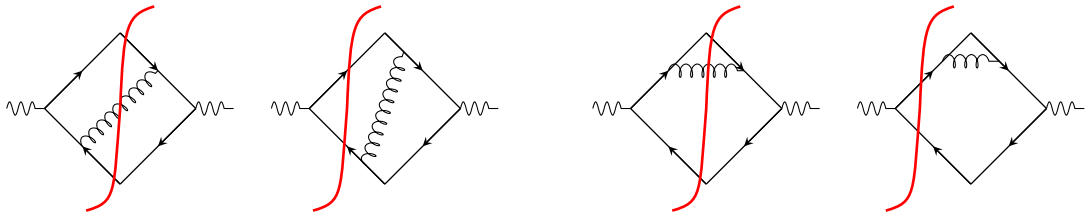

Figure 1.2: Cut diagrams of $\gamma^* \to$ hadrons at $\mathcal{O}(\alpha_s)$ [1]. The cancelling contributions can be seen as the same diagrams of squared amplitudes which are cut at different places to form virtual or real contributions. Note that the fourth diagram vanishes for massless quark since the loop integral is scaleless.

While the UV divergences are removed by the counter-terms and renormalization, one also faces another type of divergences called *infrared* (IR). These divergences correspond to a region where radiative corrections are soft ($|p| = 0$) or collinear ($p_1 \parallel p_2$).

IR divergences appear also in loop integrals. As desired, cancellations of IR divergences from real and virtual contributions is guaranteed by the Kinoshita-Lee-Nauenberg (KLN) theorem [10, 11]. This has a simple intuitive interpretation that experiments cannot distinguish, for example, the final state $q$ from $q + g$, when the angle between $q$ and $g$ is too small. An example of contributions discussed in Ref. [1], which shows cancellation of IR divergences are given in Fig. 1.2. The diagrams shown in there are called *cut diagrams*, and represent squared amplitudes, where, for example, the first diagram represents one of the contributions in $\left|M^{(0)}_{\gamma^* \to q\bar{q}g}\right|^2$, whereas the second diagram contributes to $M^{(1)*}_{\gamma^* \to q\bar{q}} M^{(0)}_{\gamma^* \to q\bar{q}}$. The superscripts (0) and (1) indicate the number of loops. As we shall discuss later, the IR singularities also appear in the initial state radiation. The KLN theorem cannot be applied here and another treatment is required. Since we are interested in the high-energy processes, the masses of light flavours $\{u, d, s\}$ will often be ignored.

## 1.2 Deep inelastic scattering

As we discussed, on the one hand, processes whose scales are sufficiently larger than a characteristic scale of QCD ($Q \gg \Lambda_{\mathrm{QCD}}$) can be computed as perturbative series in the strong coupling thanks to the asymptotic freedom. On the other hand, processes which are characterized by lower scales ($Q \lesssim \Lambda_{\mathrm{QCD}}$) cannot be computed in pQCD.

One of such objects which receives genuinely non-perturbative contribution is the *parton distribution function* (PDF), which describes the structure of a hadron. The PDFs can be extracted from experiments, and throughout the history of QCD, a type of experiments called *deep inelastic scattering* (DIS) played a crucial role in revealing the structure of the proton.

Two important types of DIS processes are depicted in Fig. 1.3 and they correspond to

$$e^-(k) + P(p_P) \to \begin{cases} e^-(k') \ + \ X(p_X), \\ e^-(k') \ + \ X(p_X) \ + \ Y(p_Y), \end{cases} \tag{1.26}$$

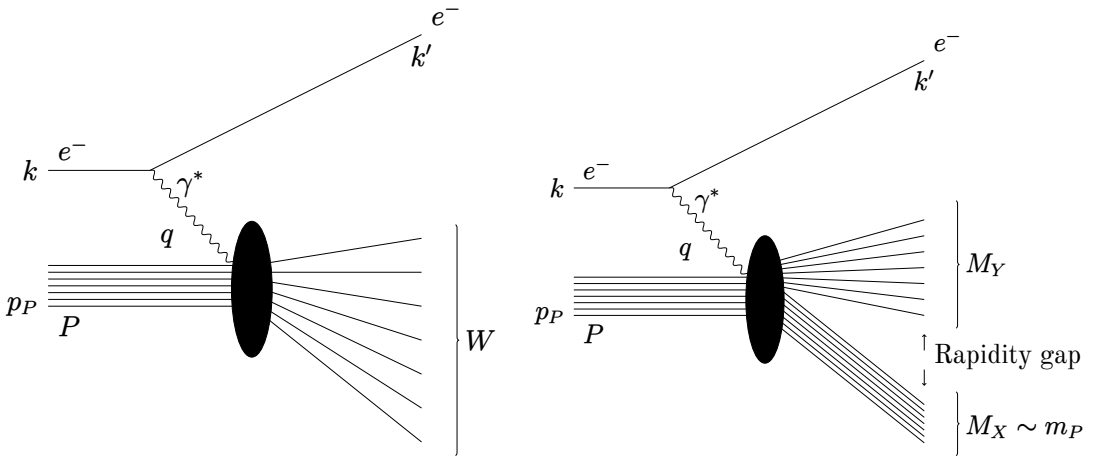


Figure 1.3: Schematic view of DIS (Left: Inclusive, Right: Diffractive) in the single-photon channel.

in both of which, an electron and a proton collide by exchanging a space-like virtual photon with momentum transfer $q = k - k'$ and $q^2 < 0$. In the left-hand-side picture, inclusive DIS process is shown. Here, only the scattered electron is singled out, while all the final-state hadronic activity is summed up. In the right-hand-side picture, the process of diffractive DIS is depicted. It is characterized by the rapidity gap in the final state, in which the system $X$ has an invariant mass near the proton mass, thus the proton remains (almost) intact. It is also possible to exchange charged vector bosons $W^{\pm}$, in which case, the process is called charged-current DIS, in contrast to the neutral-current one. In this section, we will consider only neutral-current, inclusive DIS.

Let us start by summarizing the kinematic variables of DIS for convenience [12]

$$\begin{aligned}
q^2 = (k-k')^2 \quad &= -Q^2, & s = (p_P + k)^2, \qquad & W^2 = p_X^2, \\
\nu = \frac{p_P \cdot q}{m_P} \quad &= \frac{W^2 + Q^2 - m_P^2}{2m_P} \quad &= (E_e - E_e'), \\
x = \frac{-q^2}{2p_P \cdot q} \quad &= \frac{Q^2}{2m_P \nu} \quad &= \frac{Q^2}{W^2 + Q^2 - m_P^2}, \\
y = \frac{p_P \cdot q}{p_P \cdot k} \quad &= \frac{2m_P \nu}{(s - m_P^2)} \quad &= \frac{W^2 + Q^2 - m_P^2}{(s - m_P^2)} \quad = 1 - \frac{E_e'}{E_e},
\end{aligned} \tag{1.27}$$

where the energies of the initial and final state electrons $E_e$ and $E_e'$ are given in the proton rest frame, in which $y \in [0, 1]$ is the fractional energy loss of the colliding electron, whereas $\nu$ is the energy of the photon. $\sqrt{s}$ is, as usual, the centre-of-mass energy of the incoming $e^- + P$ system, and $W$ is the invariant mass of the hadronic final state.

Let us also introduce two important limits: the so-called *Bjorken limit*, in which $Q^2 \to \infty$ for fixed $x$, and the *Gribov-Regge limit*, where $x \to 0$ for fixed $Q^2$. DIS is commonly described in the so-called infinite-momentum frame (IMF) [13], where the proton is boosted along the $z$ axis, and its momentum is given by $p_P = (P, 0, 0, P)$, for large $P \gg m_P$ compared to the proton mass. The importance of this frame is, as

we will discuss in more detail in Sec. 1.2.1, that the proton appears as a frozen, thin disk, due to the Lorentz contraction and time dilation. The Breit frame [13], which is also a common frame, is characterized by the photon momentum being given by $q = (0, 0, 0, Q)$.

At leading order in $\alpha_{\text{em}}$, the scattering amplitude for the process depicted in the left-hand side of Fig. 1.3 is given by [12, 14]

$$i\mathcal{M} = (ie)^2 \overline{u}(k')\gamma^\mu u(k) \frac{ig^{\mu\nu}}{q^2} \langle X| J^\nu |P\rangle , \tag{1.28}$$

where $X$ denotes "anything" in the final state, and for which the cross section (electron spin averaged) is given by

$$d\sigma = \frac{1}{\text{flux}} \frac{d^3k'}{(2\pi^3)2E'} \sum_X (2\pi)^4 \delta^4(k - p_P - p_X) \frac{1}{2} \sum_{\text{spins}} |\mathcal{M}|^2 , \tag{1.29}$$

where the flux factor in the proton rest frame is $\text{flux} = 4E_e m_P$ [14]. This can be expressed in terms of a leptonic tensor $L^{\mu\nu}(k, q)$ and a hadronic tensor $W_{\mu\nu}(p, q)$ [4, 12, 14]:

$$\sum_{\text{spins}} |\mathcal{M}|^2 = \frac{e^4}{(q^2)^2} L_{\mu\nu} \langle P| J^\mu |X\rangle \langle X| J^\nu |P\rangle , \tag{1.30}$$

where

$$W^{\mu\nu} = \frac{1}{4\pi} \sum_X (2\pi)^4 \delta^4(q + p_P - p_X) \langle P| J^\mu |X\rangle \langle X| J^\nu |P\rangle . \tag{1.31}$$

The leptonic tensor describes the emission of a photon from the electron, while the hadronic tensor describes the process where the photon interacts with the proton. The leptonic tensor is calculable in QED, while the hadronic part is not a perturbative object. Nonetheless, it has a general form [4, 12, 14–16][1]

$$\begin{aligned} W^{\mu\nu}(p, q) = &- \left( g^{\mu\nu} - \frac{q^\mu q^\nu}{q^2} \right) W_1 \left( x, Q^2 \right) \\ &+ \left( p_P^\mu - q^\mu \frac{p_P \cdot q}{q^2} \right) \left( p_P^\nu - q^\nu \frac{p_P \cdot q}{q^2} \right) W_2 \left( x, Q^2 \right) \\ &- i\epsilon^{\mu\nu\lambda\sigma} p_{P\lambda} q_\sigma W_3 \left( x, Q^2 \right), \end{aligned} \tag{1.32}$$

which follows from the conservation of the electromagnetic current

$$q_\mu W^{\mu\nu} = q_\nu W^{\mu\nu} = 0. \tag{1.33}$$

The third term of Eq. (1.32) vanishes (parity violating structure function) [4, 12, 14] if we only consider the photon case, therefore, in what follows, we will focus on the first two terms. The scalar functions, $W_1$ and $W_2$ are commonly replaced by the so-

[1] Details of a full form for the weak interaction with non-zero quark mass can be found in Ref. [16], p.357.

called *structure functions* [4, 12, 14]

$$F_1(x, Q^2) = W_1(x, Q^2) \qquad \text{and} \qquad F_2(x, Q^2) = \nu W_2(x, Q^2). \tag{1.34}$$

One can express the cross section for inclusive DIS in terms of $F_1$ and $F_2$ as

$$\begin{aligned}\frac{d\sigma}{dW dQ^2} =& \frac{4\pi\alpha^2 m_P}{(s - m_P^2)^2 Q^2} F_1(x, Q^2) \\ &+ \left( \frac{(s - m_P^2)(s - W^2 - Q^2)}{m_P^2 Q^2} - 1 \right) \frac{2m_P}{W^2 + Q^2 - m_P^2} F_2(x, Q^2).\end{aligned} \tag{1.35}$$

It was observed that, at sufficiently large $Q$, the structure functions depend only on a scaling variable $x$ (commonly refereed to as Bjorken $x$) [4, 12, 14]. This motivated the idea of the parton model [4], in which the proton consists of point-like partons [4, 12, 14]. Moreover, the structure functions $F_1$ and $F_2$ are related at leading order by [4, 12, 14]

$$F_2(x, Q^2) = 2xF_1(x, Q^2). \tag{1.36}$$

This relation, called Callan-Gross relation, originates from the nature of spin-1/2 partons [4, 12, 14]. We can also define the structure functions for transversely (T) and longitudinally (L) polarized photons:

$$2xF_1 = F_T = \frac{Q^2}{4\pi^2\alpha}\sigma_T, \tag{1.37}$$

$$F_2 - 2xF_1 = F_L = \frac{Q^2}{4\pi^2\alpha}\sigma_L, \tag{1.38}$$

therefore

$$F_2 = F_T + F_L. \tag{1.39}$$

In the parton model, one naively[2] writes

$$F_2(x) = x \sum_f e_f^2 \left( f(x) + \overline{f}(x) \right), \tag{1.40}$$

where $e_f$ are the parton charges and $f(x)$ are the parton distribution functions (PDFs), and the sum runs over the (active) flavours, $f \in \{u, d, s, \cdots\}$ of the partons. In this case, the PDFs are the probabilities of finding a parton which carries the momentum fraction $x$ of the proton.

### 1.2.1 Factorization

In the Bjorken limit, where $Q \to \infty$ for a fixed value of $x$, the relevant time scale is $\sim 1/Q$, while the typical time scale of interactions inside the proton is $\sim 1/\Lambda_{\text{QCD}}$. In what is called the *impulse approximation* [4, 12, 17], the photon interacts with the proton which is practically frozen. As mentioned earlier, in the infinite momentum

[2] This definition is exact in the so-called DIS scheme [2, 4]. However, throughout this thesis, we shall use PDFs in $\overline{\text{MS}}$ scheme.

frame, where the proton is boosted, the proton pictorially looks as if it was a frozen flat disk [4]. The idea that in the Bjorken limit, the interaction of the photon with the proton is independent of the mutual interactions of quarks is vital in the following discussion.

When we consider the photon-parton interaction to be decoupled from the low-scale partonic interactions, the matrix elements can be factorized at the level of probabilities. Then, the factorized formula for the structure function reads [2]

$$F_2 = \sum_a \int_x^1 \frac{d\xi}{\xi} f_{a/A}(\xi, \mu_F) H_a(x/\xi, \mu_F, q) + \text{higher twists}, \tag{1.41}$$

in which the hard, perturbative part is described by the partonic cross section $H_a$ and the non-perturbative effects are encoded entirely in the parton distribution functions, $f_{a/A}$, for the parton species $a$. It is also important to note that $H_a$ is the same for different types of colliding hadrons $A$. The remainder, which is of the order of $\mathcal{O}(\Lambda^2_{\text{QCD}}/Q^2)$ [2,13], is called the "higher twist contributions". The name comes from the terminology introduced in the operator product expansion approach [2,12,13].

One notices that in Eq. (1.41), $\mu_F$ dependence was added in the PDFs. This is the factorization scale which effectively controls the resolution of the probe. In fact, while it was discussed previously that the KLN theorem guarantees the cancellation of divergences in the real and virtual corrections, the singularities originating from collinear emissions in the initial state remain. The initial emissions are therefore absorbed inside the definition of the PDFs which acquire scale dependence. Because physical quantities, like $F_2$, cannot depend on the additional scale $\mu_F$, similarly to the case of renormalization, one obtains a set of equations for the PDFs, which describe the factorization scale dependence. These are called the Dokshitzer–Gribov–Lipatov–Alterelli–Parisi (DGLAP) evolution equations [17–21],

$$\mu^2 \frac{\partial f}{\partial \mu^2}(x, \mu^2) = \int_x^1 \frac{dz}{z} \frac{\alpha_s}{2\pi} \left[ \sum_{f'} P^{(0)}_{ff'}(z) f'(x/z, \mu^2) \right], \tag{1.42}$$

where the LO Altereli–Parisi (AP) spilliting kernels are given by

$$P^{(0)}_{qq}(z) = C_F \left( \frac{1+z^2}{1-z} \right)_+, \tag{1.43}$$

$$P^{(0)}_{qg}(z) = T_F \left( z^2 + (1-z)^2 \right), \tag{1.44}$$

$$P^{(0)}_{gg}(z) = 2C_A \left( \frac{z}{(1-z)_+} + \frac{1-z}{z} + z(1-z) \right) + \frac{11C_A - 4n_f T_F}{6} \delta(1-z), \tag{1.45}$$

$$P^{(0)}_{gq}(z) = C_F \frac{1+(1-z)^2}{z}. \tag{1.46}$$

In the above expressions, $()_+$ denotes the so-called *plus-distribution*:

$$\left( \frac{1}{x} \right)_+ f(x) = \frac{f(x) - f(0)}{x}, \tag{1.47}$$

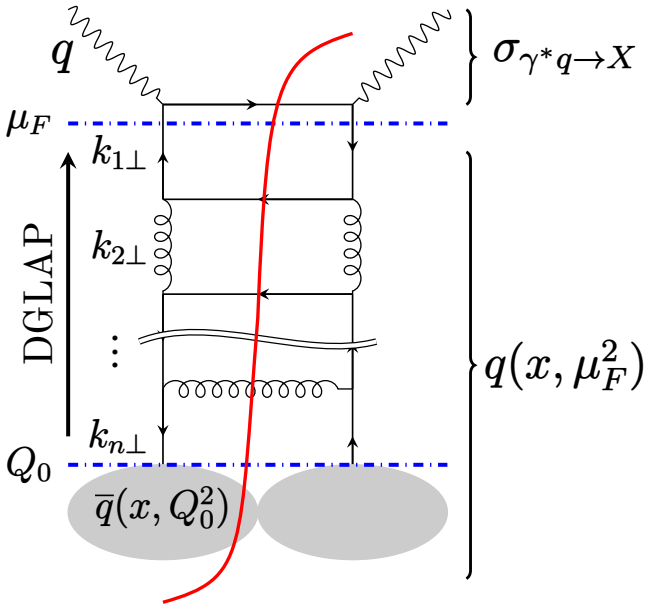


Figure 1.4: An example of a ladder diagram, in which $k_T$s are ordered as $\mu_F \gg k_{1T} \gg k_{2T} \gg \cdots$. The splittings below the factorization scale $\mu_F$ are absorbed inside the PDFs. Notice that due to the flavour mixing in Eq. (1.42), this diagram is only one of many contributions to DGLAP evolution.

for some regular function $f(x)$.

As one can see, the evolution (1.42) mixes PDFs of different parton species. DGLAP evolution can be pictured as a ladder diagram shown in Fig. 1.4. In this diagram, the photon probes a quark, while the evolution involves different types of partons by a series of splittings. The leading contributions correspond to situations where, at each step, the transverse momentum scale increases strongly, and eventually reaches the factorization scale, $\mu_F$. That is to say, the leading contribution is characterized by the strong ordering,

$$\mu_F \gg k_{1T} \gg k_{2T} \gg \cdots \gg Q_0 \,, \tag{1.48}$$

where we set the starting scale of the evolution to be $Q_0 \sim 1$ GeV. Also, it is a common practice to set $\mu_F = Q$, which we will employ. The configuration (1.48), is enhanced by large logarithms, $\ln(Q/Q_0)$, which are effectively resummed by the DGLAP equations. Configurations in which one or more of $\gg$ orderings from Eq. (1.48) are replaced by $\simeq$ correspond to subleading corrections to the DGLAP equation.

Let us see how we can get an intuitive picture of DGLAP evolution [13]. One first considers a distribution at scale $Q_0$, $f(x, Q_0^2)$. The parton branches, thus reducing its $x$, while increasing its virtuality $\mu^2$. Eventually, the parton reaches the scale $Q^2$, where it enters the hard process. The increase in $f(x, \mu^2)$, for a small increase in $\mu^2$, is expressed as (for now considering no mixing with different types of partons)

$$\delta f_{\text{in}}(x, \mu^2) = \frac{\delta\mu^2}{\mu^2} \int_x^1 dx' dz \frac{\alpha_s}{2\pi} \hat{P}(z) f(x', \mu^2) \delta(x - zx') \tag{1.49}$$

which is simply all splittings from $f(x, \mu^2)$ weighted by the splitting probability $\hat{P}(z)$

(unregularized splitting function). On the other hand, the decrease is given by

$$\delta f_{\text{out}}(x,\mu^2) = \frac{\delta\mu^2}{\mu^2} f(x,\mu^2) \int_x^1 dx' dz \frac{\alpha_s}{2\pi} \hat{P}(z) \delta(x - zx'). \tag{1.50}$$

Therefore, in total, the change of the parton distribution reads

$$\delta f(x,\mu^2) = \frac{\delta\mu^2}{\mu^2} \int_x^1 dz \frac{\alpha_s}{2\pi} \hat{P}(z) \left[ f(x/z,\mu^2)/z - f(x,\mu^2) \right]. \tag{1.51}$$

One can see now that the expression in the square bracket makes the limit $z \to 1$ regular. Using the plus distribution, one arrives at

$$\mu^2 \frac{\partial f(x,\mu^2)}{\partial \mu^2} = \int_x^1 \frac{dz}{z} \frac{\alpha_s}{2\pi} P(z) f(x/z,\mu^2). \tag{1.52}$$

This, when generalised to multiple parton spices, yields the DGLAP equations (1.42). This view of DGLAP evolution, called *parton branching*, is popular in Monte-Carlo simulations [13].

Let us now introduce a function called the *Sudakov form factor* [13]:

$$\Delta(\mu_0^2,\mu^2) = \exp\left[ - \int_{\mu_0^2}^{\mu^2} \frac{d\mu'^2}{\mu'^2} \int dz \frac{\alpha_s}{2\pi} \hat{P}(z) \right]. \tag{1.53}$$

With this, Eq. (1.51) can be written as

$$\delta f(x,\mu^2) = \frac{\delta\mu^2}{\mu^2} \int_x^1 dz \frac{\alpha_s}{2\pi} \hat{P}(z) \left[ f(x/z,\mu^2)/z \right] - \frac{f(x,\mu^2)}{\Delta(\mu_0^2,\mu^2)} \mu^2 \frac{\partial}{\partial\mu^2} \Delta(\mu_0^2,\mu^2), \tag{1.54}$$

for which we obtain, with the initial distribution $f(x,\mu_0^2)$

$$f(x,\mu^2) = \Delta(\mu_0^2,\mu^2) f(x,\mu_0^2) + \int_{\mu_0^2}^{\mu^2} \frac{d\mu'^2}{\mu'^2} \frac{\Delta(\mu_0^2,\mu^2)}{\Delta(\mu_0^2,\mu'^2)} \int \frac{dz}{z} \frac{\alpha_s}{2\pi} \hat{P}(z) f(x/z,\mu'^2). \tag{1.55}$$

Due to the absence of plus distribution in the above Eq. (1.55), the $z$-integral requites some upper cut-off. Above this cut-off, the branching is considered to be unresolvable. The Sudakov form factor has a simple interpretation in this picture as a probability of evolving from $\mu_0^2$ to $\mu^2$ without resolvable emissions, thus it is often termed as the *survival factor* [13, 22].

What is remarkable about the collinear factorization is that the PDFs defined in Eq. (1.41) are universal. That is to say, the factorization of the Drell-Yan (DY) process

$$p + p \to l + \bar{l} + X, \tag{1.56}$$

involves the same PDFs as those obtained in the DIS processes:

$$\frac{d\sigma_{DY}}{dQ^2 dy} = \sum_f \int_{x_A}^1 d\xi_A \int_{x_B}^1 d\xi_B f_{f/A}(\xi_A, Q^2) f_{\bar{f}/B}(\xi_B, Q^2) \sigma_{f\bar{f}\to l\bar{l}}(x_A/\xi_A, x_B/\xi_B, Q^2), \tag{1.57}$$

where $\sigma_{f\bar{f}\to l\bar{l}}(x_A/\xi_A, x_B/\xi_B, Q^2)$ are the partonic cross sections for the lepton-pair production processes $f + \overline{f} \to l + \bar{l}$.

Indeed, the leading order collinear PDFs can be thought of as number densities, and can be obtained from the creation-annihilation operators, where, for quarks, we have [2, 4, 23]

$$f_{q/A}(\xi, \mu^2) = \frac{1}{(2\pi)^2} \int d^2 k_T \, \langle P | \, b^\dagger(\xi p_P, k_T) b(\xi p_P, k_T) \, | P \rangle \, . \tag{1.58}$$

From the above, the operator definition of collinear PDFs in the axial gauge is given by [2, 4, 23]

$$f_{q/A}(\xi, \mu^2) = \frac{1}{4\pi} \int dx^- e^{-i\xi P^+ x^-} \, \langle P | \, \overline{\psi}(0, x^-, 0_\perp) \gamma^+ \psi(0, 0, 0_\perp) \, | P \rangle \, , \tag{1.59}$$

$$f_{g/A}(\xi, \mu^2) = \frac{1}{2\pi\xi P^+} \int dx^- e^{-i\xi P^+ x^-} \, \langle P | \, F_a(0, x^-, 0_\perp)^{+\nu} F_b(0, 0, 0_\perp)^+_\nu \, | P \rangle \, , \tag{1.60}$$

where the superscripts $+$ and $-$ denote components given by the *Sudakov decomposition*

$$p^\mu = p^+ \frac{\overline{n}^\mu}{2} + p^- \frac{n^\mu}{2} + p^\mu_\perp, \tag{1.61}$$

where $n$ is a light like vector collinear to $p_P$, with a axillary light-like vector $\overline{n}$, which satisfies $n \cdot \overline{n} = 2$ and $n \cdot p_\perp = \overline{n} \cdot p_\perp = 0$.

## 1.3 Soft-collinear effective theory

### 1.3.1 Strategy of regions

Problems in QCD often involve several disparate scales, for example, an invariant mass of a lepton pair and its transverse momentum in the Drell-Yan (DY) processes in the back-to-back limit. In order to simplify the calculations, one may naively consider an expansion of an integrand around a small scale, for example, a ratio of small transverse momentum and the hard scale. However, it may happen that the integration and the expansion do not commute. The correct approach to that problem is provided by the so-called *strategy of regions* (*expansion by regions*) [24–27]. This, as the name suggests, decomposes the phase space into appropriate kinematic regions, and for each region, the integrand is expanded in the corresponding small parameter. When added, such integrals produce the correct asymptotic expansion of the original integral.

Consider a problem with two scales, $\Lambda_l$ and $\Lambda_h$, where $\Lambda_l \ll \Lambda_h$. In this case, the integration can be split into two parts, where the expansion around $\Lambda_l/k$ and $k/\Lambda_h$,

respectively, are considered:

$$I = \int_0^\Lambda dk\ f(k)|_{k/\Lambda_h \ll 1} + \int_\Lambda^\infty dk\ f(k)|_{\Lambda_l/k \ll 1}\ , \tag{1.62}$$

where $f(x)|_\lambda \ll 1$ means the Taylor expansion of $f(x)$in the small-$\lambda$ limit.

In fact, in the strategy of regions [24, 25], one considers

$$I = \int_0^\infty d^dk\ f(k)|_{k/\Lambda_h \ll 1} + \int_0^\infty d^dk\ f(k)|_{\Lambda_l/k \ll 1} - R_{\text{zero-bin}}, \tag{1.63}$$

where the integration is performed in $d$ dimensions, and thus the divergences are dimensionally regularized. The last term, called *zero-bin* [27], accounts for the overlapping region between the two integrals. Contributions from such overlaps are possible, in principle as the integrals in Eq. (1.63) run from 0 to $\infty$. The zero-bin contribution, however, often yields scaleless integrals which vanish in the dimensional regularization [26, 27]. One should note that the terms in Eq. (1.63) may generate, respectively, additional UV and IR divergences as $1/\epsilon$ poles, even if the original integral does not [26]. These poles are expected to cancel each other in the sum.

In order to apply this method, one first needs to identify the relevant regions with singularities. In the above example, Eq. (1.63), the integral was decomposed into two regions: hard and soft. For the problems we will discuss later, there are more regions with singularities.

The idea of expansion by regions gave rise to the Soft-Collinear Effective Theory (SCET) [27–30]. Let us introduce two light-like vectors

$$n^\mu = (1, 0, 0, 1), \qquad \overline{n}^\mu = (1, 0, 0, -1), \tag{1.64}$$

such that

$$n^2 = 0, \qquad \overline{n}^2 = 0, \qquad n \cdot \overline{n} = 2. \tag{1.65}$$

With these reference momenta, one decomposes a momentum as given in Eq. (1.61).

The two reference vectors (1.64) can be chosen differently, and there is, in fact, a certain freedom to do so, which is called *reparametrization invariance* [27, 31]. A sub-class of this invariance is that, under rescalings

$$n \to (1+\delta)\, n \qquad \text{and} \qquad \overline{n} \to (1-\delta)\, \overline{n}, \tag{1.66}$$

with an infinitesimal parameter $\delta$, the condition (1.65), remains unchanged.

It is also convenient to define the transverse size

$$p_\perp^2 = -p_T^2, \tag{1.67}$$

and label a momentum as

$$(p_+, p_-, p_T). \tag{1.68}$$

In this notation, the hard ($h$), $n$-collinear ($c$), $\overline{n}$-collinear/anti-collinear ($\overline{c}$) and soft

($s$) regions are, respectively, expressed as

$$(l_+, l_-, l_T)|_h \sim Q(1, 1, 1), \tag{1.69}$$
$$(l_+, l_-, l_T)|_c \sim Q(\lambda^2, 1, \lambda), \tag{1.70}$$
$$(l_+, l_-, l_T)|_{\bar{c}} \sim Q(1, \lambda^2, \lambda), \tag{1.71}$$
$$(l_+, l_-, l_T)|_{\mathrm{s}} \sim Q(\lambda^2, \lambda^2, \lambda^2), \tag{1.72}$$

where $\lambda \ll 1$ is a small parameter. In some cases, one needs to consider also a hard-soft region $\sim Q(\lambda, \lambda, \lambda)$. The theory which involves such region is termed as $\mathrm{SCET_{II}}$, whereas the hard-soft contribution is absent in $\mathrm{SCET_I}$ [27].

Once the regions are identified, one performs *derivative/multipole-expansions*. For example, in the collinear region of $k$, a scalar product can be expanded as

$$(k + l)^2 = 2k_- l_+ + \mathcal{O}(\lambda). \tag{1.73}$$

The small expansion parameter is commonly defined as $\lambda \simeq \frac{q_T}{Q}$ for some momentum $q$ and $Q^2 = |q^2|$ of, for example, a back-to-back lepton pair in the DY process. As we will see below, this parameter is a very useful tool in SCET, as the different fields are characterized by the scaling in terms of $\lambda$, as defined in Eqs. (1.69)–(1.72).

In an effective theory, one constructs an effective Lagrangian which reproduces the expanded integrands. Therefore, one can obtain expanded integrands directly from Feynman rules of the effective theory. In SCET, field operators are decomposed into collinear, anti-collinear and soft components. The hard field $\psi_{\mathrm{hard}}$ is integrated out and absorbed in factors called *Wilson coefficients*, which are coupling constants of the effective theory [27, 32]. In practice, however, the Wilson coefficients are calculated by matching to the full theory, *i.e.* QCD. In SCET, the effective Lagrangian reads

$$\mathcal{L} = \mathcal{L}_c + \mathcal{L}_{\bar{c}} + \mathcal{L}_s + \mathcal{L}_{s+c}, \tag{1.74}$$

and, it involves Wilson coefficients, which are adjusted such that the results obtained from the effective Lagrangian (1.74) agree with the full theory (1.1) results. Except for the soft-collinear interaction term, $\mathcal{L}_{s+c}$, the Lagrangians of respective degrees of freedom are copies of that of QCD [27, 32]. As a consequence, only operators which involve both of the two collinear fields gets matching corrections [27, 32].

$\mathcal{L}_{s+c}$ contains interaction terms between soft and (anti-)collinear fields. Which interactions between the fields are allowed in the Lagrangian is to be determined from momentum conservation. For example, the interaction of the soft and collinear fields is valid since

$$(\lambda^2, 1, \lambda) + (\lambda^2, \lambda^2, \lambda^2) \simeq (\lambda^2, 1, \lambda), \tag{1.75}$$

whereas the interaction of the anti-collinear and collinear fields is invalid since

$$(\lambda^2, 1, \lambda) + (1, \lambda^2, \lambda) \simeq (1, 1, \lambda), \tag{1.76}$$

which gives rise to the momentum in a region which is not any of the SCET fields (1.69)–(1.72).

When the Lagrangian is specified, one then needs to define operators. An impor-

tant concept in SCET is *power counting*, in which operators and fields are expanded in the parameter $\lambda$. The behaviour of the fields is obtained by considering a time-ordered product [27, 32]

$$\langle 0|\, T\left\{\psi_s(x)\overline{\psi}_s(0)\right\}|0\rangle = i\int \frac{d^4p}{(2\pi)^4}\frac{\not{p}}{p^2+i0}e^{-ip\cdot x}. \tag{1.77}$$

In the case of the soft quark field, the scaling of the momentum is $p \sim (\lambda^2, \lambda^2, \lambda^2)$, and its conjugate $x$ scales like $\sim (1/\lambda^2, 1/\lambda^2, 1/\lambda^2)$, thus the right-hand side is $\sim (\lambda^2)^4\frac{\lambda^2}{\lambda^4}$. One, therefore, obtains $\psi_s \sim \lambda^3$. The above case was simple due to the uniform scaling of the momentum. In the case of the collinear fields, one decomposes the fields with the projectors

$$P_+ = \frac{\not{n}\bar{\not{n}}}{4} \qquad \text{and} \qquad P_- = \frac{\bar{\not{n}}\not{n}}{4}, \tag{1.78}$$

which yields, for the quark field,

$$\xi_c \equiv P_+\psi_c \qquad \text{and} \qquad \eta_c \equiv P_-\psi_c. \tag{1.79}$$

The scaling can be found as

$$\begin{aligned}\langle 0|\, T\left\{\xi_c(x)\bar{\xi}_c(0)\right\}|0\rangle &= i\int \frac{d^4p}{(2\pi)^4}\frac{\not{n}\bar{\not{n}}}{4}\frac{\not{p}}{p^2+i0}\frac{\bar{\not{n}}\not{n}}{4}e^{-ip\cdot x}\\ &= i\int \frac{d^4p}{(2\pi)^4}\frac{p_-}{p^2+i0}\frac{\not{n}}{2}e^{-ip\cdot x},\end{aligned} \tag{1.80}$$

and similarly for $\eta_c$, which shows that they scale as $\xi_c \sim \lambda$ and $\eta_c \sim \lambda^2$. The small component $\eta_c$ can be integrated out [27, 32].

SCET inherits gauge invariance from QCD, however the gauge transformation is also decomposed into soft and collinear parts [27]:

$$\begin{aligned} V_s(x) &= e^{i\theta_s^a(x)t^a}, \qquad \text{where} \qquad \partial_\mu\theta_s^a(x) \sim (\lambda^2,\lambda^2,\lambda^2)\theta_s^a(x),\\ V_c(x) &= e^{i\theta_c^a(x)t^a}, \qquad \text{where} \qquad \partial_\mu\theta_c^a(x) \sim (\lambda^2,1,\lambda)\theta_c^a(x).\end{aligned} \tag{1.81}$$

On the one hand, the soft fields transform as

$$\begin{aligned}&\psi_s(x) \to V_s(x)\psi_s(x),\\ &A_s^\mu(x) \to V_s(x)A_s^\mu(x)V_s^\dagger(x) + \frac{i}{g}V_s(x)\left(\partial^\mu V_s^\dagger(x)\right),\end{aligned} \tag{1.82}$$

then $D_s^\mu(x) \to V_s(x)D_s^\mu(x)V_s^\dagger(x)$. On the other hand, the collinear fields transform as

$$\begin{aligned}&\psi_c(x) \to V_s(x_-)\psi_c(x),\\ &A_c^\mu(x) \to V_s(x_-)A_c^\mu(x)V_s^\dagger(x_-).\end{aligned} \tag{1.83}$$

Notice that the argument of the gauge transformation is $x_-$. This is due to the mul-

tipole expansion:

$$V_s(x) \simeq V(x_-) + \underbrace{x_\perp \partial_\perp V_s(x)}_{\mathcal{O}(\lambda)} + \underbrace{x_+ \partial_- V_s(x)}_{\mathcal{O}(\lambda^2)}, \tag{1.84}$$

where, for the collinear field, $x \sim (1, 1/\lambda^2, 1/\lambda)$. The transformation property of the gauge field $A_c^\mu(x)$ ensures that the mixed covariant derivative

$$D^\mu = D_c^\mu - ig\, n \cdot A_s(x_-), \tag{1.85}$$

transforms as

$$D^\mu(x) \to V_s(x_-) D^\mu(x) V_s^\dagger(x_-), \tag{1.86}$$

where the soft and collinear covariant derivatives are defined in analogy to Eq. (1.2) with appropriate fields replacing $A$.

For the collinear gauge transformation, the soft field is invariant [32], while the collinear field transforms as

$$\xi_c(x) \to V_c(x) \xi_c(x) \qquad \text{and} \qquad D^\mu \to V_c(x) D^\mu V_c^\dagger(x). \tag{1.87}$$

One notable feature of SCET is that the derivatives of fields may not be suppressed, for example,

$$\overline{n} \cdot \partial \psi_c(x) \sim 1. \tag{1.88}$$

The inclusion of infinite unsuppressed derivatives is achieved with [27]

$$\int dt C(t) \psi_c(x + tn) = \sum_{n=0}^{\infty} \frac{C_n}{n!} \left(\overline{n} \cdot \partial\right)^n \psi_c(x). \tag{1.89}$$

Because of this, SCET operators are non-local. Products of non-local operators are not gauge invariant, however, gauge invariance can be restored by the use of *Wilson lines* [27]:

$$\begin{aligned} W_c(x) &\equiv P \exp\left[ig \int_{-\infty}^{0} ds \overline{n} \cdot A_c(x + s\overline{n})\right], \\ S_n(x) &\equiv P \exp\left[ig \int_{-\infty}^{0} ds n \cdot A_s(x + sn)\right], \end{aligned} \tag{1.90}$$

which transform as

$$W_c(x) \to V_c(x) W_c(x), \tag{1.91}$$

$$\tag{1.92}$$

assuming $V_c^\dagger(-\infty \overline{n}) = 1$. With this, one can obtain gauge-invariant fields

$$\begin{aligned} \chi_c(x) &\equiv W_c^\dagger(x) \xi_c(x), \\ \mathcal{A}_c^\mu &\equiv W_c^\dagger \left(D_c^\mu W_c\right). \end{aligned} \tag{1.93}$$

Now, with the soft Wilson line, one re-defines the collinear fields as follows:

$$\begin{aligned} \xi_c(x) &\equiv S_n^\dagger(x_-)\xi_c^{(0)}(x), \\ A_c^\mu &\equiv S_n^\dagger(x_-)A_c^{\mu(0)}S_n(x_-). \end{aligned} \tag{1.94}$$

This allows the interaction term to be written as

$$\begin{aligned} \mathcal{L}_{c+s} &= \bar{\xi}_c \frac{\bar{n}\!\!\!/}{2} in\cdot D_{c+s}\xi_c = \bar{\xi}_c \frac{\bar{n}\!\!\!/}{2} n\cdot(iD_s + A_c)\,\xi_c \\ &= \bar{\xi}_c^{(0)} \frac{\bar{n}\!\!\!/}{2} n\cdot\left(i\partial + A_c^{(0)}\right)\xi_c^{(0)}, \end{aligned} \tag{1.95}$$

where the fact that the covariant derivative along the Wilson line is zero

$$n\cdot D_s S_n(x_-) = n\cdot D_{s-}S_n(x_-) = 0 \tag{1.96}$$

was used. The new interaction term in Eq. (1.95) is free of soft-collinear interactions, *cf.* (1.75), at leading order (also between collinear and soft gluons, see Ref. [27]).

Finally, one has

$$\mathcal{L}_{\text{SCET}} = \mathcal{L}_c^{(0)} + \mathcal{L}_{\bar{c}}^{(0)} + \mathcal{L}_s, \tag{1.97}$$

in which no interactions between different regions are present. The procedure of Eq. (1.94) is called *decoupling transformation* and it is a key step towards factorization in SCET. Due to the disappearance of soft-collinear interactions, the states are decomposed as

$$|X\rangle = |X_c\rangle \otimes |X_{\bar{c}}\rangle \otimes |X_s\rangle\,. \tag{1.98}$$

From now on, the super script $^{(0)}$ is dropped, but the re-defined fields of Eq. (1.94) should be understood. One should also keep in mind that the decoupling is correct only at the leading order in $\lambda$, and it does not mean that the soft effects disappear.

With the components presented above, the current, which is relevant for the SCET definition of hadronic matrix elements analogous to Eq. (1.29) is matched such that [33]

$$J^\mu = C_V(-q^2)g\;\bar{\chi}_{\bar{c}}\;S_{\bar{n}}^\dagger\;\gamma^\mu\;S_n\;\chi_c, \tag{1.99}$$

where $C_V$ is a corresponding Wilson coefficient. With Eq. (1.99) and the decomposition of Eq. (1.98), the hadronic matrix elements, which appear in the hadronic tensor of DY cross section factorize as [33]

$$\begin{aligned} \langle N_1(p)N_2(\bar{p})|\,J^{\dagger\mu}(x)J^\nu(0)\,|N_1(p)N_2(\bar{p})\rangle &= \left|C_V(Q^2,\mu^2)\right|^2 \\ &\times \hat{W}_{\text{DY}}(x)\quad \langle N_1(p)|\,\bar{\chi}_c(x)\frac{\bar{n}\!\!\!/}{2}\chi_c(0)\,|N_1(p)\rangle\,\langle N_2(\bar{p})|\,\bar{\chi}_{\bar{c}}(0)\frac{n\!\!\!/}{2}\chi_{\bar{c}}(x)\,|N_2(\bar{p})\rangle\,, \end{aligned} \tag{1.100}$$

where the soft Wilson-line correlator is defined as

$$\hat{W}_{\text{DY}}(x) = \frac{1}{N_c}\,\langle 0|\,\overline{T}\,\text{tr}\left(S_n^\dagger(x)S_{\bar{n}}(x)\right)T\left(S_{\bar{n}}^\dagger(x)S_n(x)\right)|0\rangle\,. \tag{1.101}$$

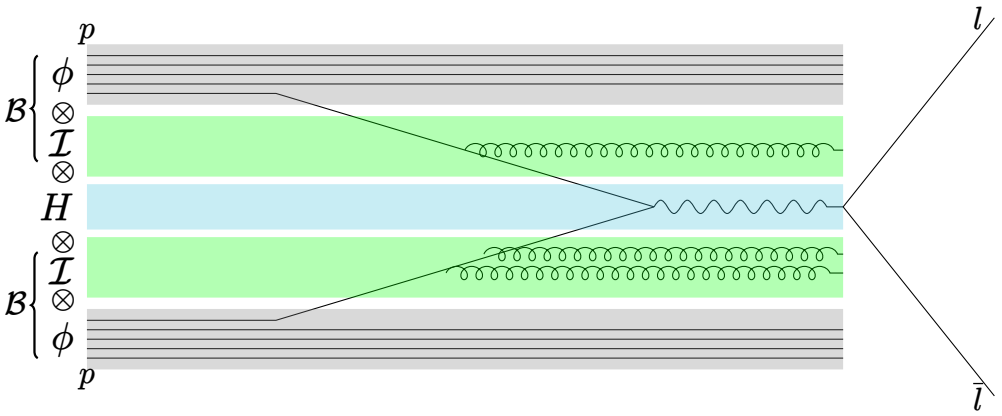


Figure 1.5: A schematic view of factorization of a Drell-Yan process with beam functions.

Multipole expansion with $x \sim (1, 1, 1/\lambda)$ for $q \sim (1, 1, \lambda)$ gives $\hat{W}_{\mathrm{DY}}(0) = 1$ [33]. This object resums soft, wide-angle radiation, and it is therefore called the *soft function*. The remaining factors in Eq. (1.100)

$$\langle N_1(p)|\,\overline{\chi}_c(x)\frac{\bar{n}\!\!\!/}{2}\chi_c(0)\,|N_1(p)\rangle \quad \text{and} \quad \langle N_2(\bar{p})|\,\overline{\chi}_{\bar{c}}(0)\frac{\bar{n}\!\!\!/}{2}\chi_{\bar{c}}(x)\,|N_2(\bar{p})\rangle\,, \tag{1.102}$$

are called the *beam functions*, respectively for the collinear and anti-collinear sectors. Factorization of Eq. (1.100) is schematically depicted in Fig. 1.5, in which $H$ corresponds to $|C_V|^2$, and either parts represented by $\mathcal{B}$ correspond to the matrix element of each sector: collinear and anti-collinear. The factorized hadronic matrix elements in Eq. (1.100) is the main object that will be studied in Chapter 2.

### 1.3.2 UV renormalization of SCET

In QCD, as we discussed earlier in Sec 1.1, the UV divergences, which appear in the loops, are renormalized by the replacement of the bare coupling with the renormalized coupling[3]. The remaining IR divergences cancel with IR divergences of real emissions, when the process under consideration is sufficiently inclusive.

Consider a scattering amplitude in QCD with on-shell external legs, $p_i^2 = 0$, and a corresponding amplitude in SCET. Since we are not summing up the unresolved real radiation, the amplitude in general divergent. Ignoring spin and colour indices, the matching of the Wilson coefficients, $C$, means

$$\mathcal{M}_{\mathrm{QCD}}(\{p_i\}, \epsilon) = C(\{p_i\}, \epsilon)\mathcal{M}_{\mathrm{SCET}}(\{p_i\}, \epsilon). \tag{1.103}$$

In the above, arbitrary number of loop corrections is understood:

$$\mathcal{M}_{\mathrm{QCD}}(\{p_i\}, \epsilon) = \mathcal{M}^{(0)}_{\mathrm{QCD}}(\{p_i\}, \epsilon) + \frac{\alpha_s}{4\pi}\mathcal{M}^{(1)}_{\mathrm{QCD}}(\{p_i\}, \epsilon) + \cdots\,. \tag{1.104}$$

[3] Unless otherwise stated, conventional dimensional regularization (*i.e.* all momenta and polarization are $d = 4 - 2\epsilon$ dimensions and gluons have $2 - 2\epsilon$ helicity states) and $\overline{\mathrm{MS}}$ scheme are considered hereafter.

It was shown in Refs. [34, 35] that there is one-to-one correspondence between the IR divergences in the on-shell amplitudes of QCD and the UV divergences of operator matrix elements of SCET. These UV divergences of SCET can be renormalized by a multiplicative factor $\boldsymbol{Z}$ [27, 34–36], which is a matrix in colour space:

$$\left|\mathcal{M}(\{p_i\},\mu^2)\right\rangle = \lim_{\epsilon\to 0} \boldsymbol{Z}^{-1}(\{p_i\},\epsilon,\mu^2)\left|\mathcal{M}(\{p_i\},\epsilon)\right\rangle. \tag{1.105}$$

This leads to the following RGE:

$$\frac{d}{d\ln\mu}\left|\mathcal{M}(\{p_i\},\mu^2)\right\rangle = \boldsymbol{\Gamma}(\{p_i\},\mu^2)\left|\mathcal{M}(\{p_i\},\mu^2)\right\rangle, \tag{1.106}$$

where the anomalous dimension $\boldsymbol{\Gamma}(\{p_i\},\mu^2)$ satisfies

$$\boldsymbol{\Gamma}(\{p_i\},\mu^2) = -\boldsymbol{Z}^{-1}(\{p_i\},\epsilon,\mu^2)\frac{d}{d\ln\mu}\boldsymbol{Z}(\{p_i\},\epsilon,\mu^2). \tag{1.107}$$

This, in turn, means that the Wilson coefficient of Eq. (1.100) satisfies

$$\frac{d}{d\ln\mu}C_V(Q^2,\mu^2) = \boldsymbol{\Gamma}(\{p_i\},\mu^2)C_V(Q^2,\mu^2). \tag{1.108}$$

In Ref. [34] it was conjectured that

$$\boldsymbol{\Gamma}(\{p_i\},\mu) = \sum_{i,j}\frac{\boldsymbol{T}_i\cdot\boldsymbol{T}_j}{2}\gamma_{\text{cusp}}\ln\left(\frac{\mu^2}{-s_{ij}}\right) + \sum_i^n \gamma_i, \tag{1.109}$$

to all orders, where

$$(\boldsymbol{T}_i^a)_{\alpha\beta} = \begin{cases} t^a_{\alpha\beta} & \text{quark} \\ -t^a_{\beta\alpha} & \text{anti-quark} \\ -if_{a\alpha\beta} & \text{gluon} \end{cases}, \tag{1.110}$$

and the first sum runs over combinations of external legs ($i \neq j$ and unordered), and $s_{ij} = \pm 2p_i\cdot p_j$ (the sign is negative if one is incoming and the other is outgoing). The cusp anomalous dimensions $\gamma_{\text{cusp}}$ and $\gamma_i \in \{\gamma_q,\gamma_g\}$ can be found in Ref. [36]. The renormalization factor $\boldsymbol{Z}$ is known up to $\mathcal{O}(\alpha_s^3)$ in the conventional dimensional regularization scheme [36], which we use here.

### 1.3.3 Operator definition of the beam function

In SCET [27], the transverse position dependent beam function is defined in terms of SCET operators as [33], *cf.* Eq. (1.100)

$$\mathcal{B}_{q/N}(z,x_T^2,\mu) = \frac{1}{2\pi}\int dt\, e^{-izt\bar{n}\cdot p}\sum_X \langle N(p)|\,\overline{\chi}(t\bar{n}+x_\perp)\,|X\rangle\,\frac{\bar{\not{n}}}{2}\,\langle X|\,\chi(0)\,|N(p)\rangle\,, \tag{1.111}$$

In comparison to the SCET definition of collinear PDFs *cf.* Eq. (1.59)

$$\phi_{q/N}(z,\mu) = \frac{1}{2\pi}\int dt\; e^{-izt\overline{n}\cdot p}\sum_X \langle N(p)|\,\overline{\chi}(t\overline{n})\,|X\rangle\,\frac{\not{\overline{n}}}{2}\,\langle X|\,\chi(0)\,|N(p)\rangle\,, \tag{1.112}$$

one can see that the difference is in the presence of the transverse separation $x_\perp$.

With the above beam functions, DY cross section naively factorizes as [33]

$$\begin{aligned}\frac{d^3\sigma}{dQ^2dq_\perp^2dy} =& \frac{4\pi\alpha}{3N_cQ^2s}\left|C_V(Q^2,\mu)\right|^2\frac{1}{4\pi}\int d^2x_\perp e^{-iq_\perp\cdot x_\perp}\\ &\times\sum_q e_q^2\left[\mathcal{B}_{q/N_1}(z_1,x_\perp^2,\mu)\mathcal{B}_{\overline{q}/N_2}(z_2,x_\perp^2,\mu)+(q\leftrightarrow\overline{q})\right]+\mathcal{O}\left(\frac{q_\perp^2}{M^2}\right),\end{aligned} \tag{1.113}$$

with a matching coefficient $C_V(Q^2,\mu)$, *cf.* Eq.(1.100).

Evaluation of Eq. (1.111) is often done in the axial gauge [33, 37, 38], where

$$\overline{n}\cdot A = 0, \tag{1.114}$$

thus the collinear Wilson lines, Eq. (1.90), reduce to unity. However, in this gauge, the gauge dependent part of the gluon propagator, Eq. (1.9), contains a linear denominator. This denominator is related to an additional type of singularities present in SCET, the so-called *rapidity (light-cone) singularities* [33, 37]. This singularity is not regularized by the standard dimensional regularization [33, 37, 39], and in Refs. [33, 39], an additional, *analytic regulator* $\alpha$ was proposed.

Introduction of $\alpha$ breaks the symmetry of $n \leftrightarrow \overline{n}$ and $p \leftrightarrow \overline{p}$, and thus the two beam functions are no longer symmetric, that is, one requires two different functions, $n$-collinear, $\mathcal{B}$, and $\overline{n}$-collinear (anti-collinear), $\overline{\mathcal{B}}$. While rapidity divergences cancel in a product of beam functions [33, 40], $Q$ dependence survives as a result [33, 39]. This phenomenon is called *collinear anomaly*. The hard-scale dependence, however, can be exponentiated by re-factorization into the form [33, 38]

$$\lim_{\alpha\to 0}[\mathcal{B}_{i/j}(z_1,x_T^2)\;\overline{\mathcal{B}}_{\bar{i}/k}(z_2,x_T^2)]_Q = \left(\frac{x_T^2Q^2}{4e^{-2\gamma_E}}\right)^{-F^b_{i\bar{i}}(x_T^2)} B^b_{i/j}(z_1,x_T^2)B^b_{\bar{i}/k}(z_2,x_T^2), \tag{1.115}$$

where $B^b_{i/j}(z,x_T^2)$ are the bare (re-factorized) beam functions. Notice that, after re-factorization, the beam functions recover symmetry between the collinear and anti-collinear sectors. At this point, the beam function contains UV and IR divergences [4]. The UV divergences are removed by the $Z$-factor [34, 38, 41, 42],

$$B^b_{i/j}(z,x_T^2) = Z_i^B(x_T^2,\mu)B_{i/j}(z,x_T^2,\mu), \tag{1.116}$$

$$F^b_{i\bar{i}}(x_T^2) = F_{i\bar{i}}(\mu) + Z_i^F(\mu), \tag{1.117}$$

[4] As previously discussed, UV divergences of SCET operator matrix elements corresponds to IR divergence of QCD.

and in $\overline{\text{MS}}$ scheme,

$$\alpha_s^b = \left(\frac{\mu^2 e^{\gamma_E}}{4\pi}\right)^{\epsilon} Z_\alpha(\mu)\alpha_s(\mu), \tag{1.118}$$

thus obtain renormalized beam function $B_{i/j}(z, x_T^2, \mu)$, which is free of the UV divergences.

Renormalization scale invariance of the cross section with Eq. (1.108) implies [33]

$$\frac{d}{d\ln\mu} C_V(Q^2,\mu^2) = \left[\Gamma^F_{\text{cusp}} \ln\left(\frac{Q^2}{\mu^2}\right) + 2\gamma^q\right] C_V(Q^2,\mu^2), \tag{1.119}$$

$$\frac{d}{d\ln\mu} F_{q\bar{q}}(x_T^2,\mu^2) = 2\Gamma^F_{\text{cusp}}, \tag{1.120}$$

$$\frac{d}{d\ln\mu} B_{q/N}(z,x_T^2,\mu^2) = \left[\Gamma^F_{\text{cusp}} \ln\left(\frac{x_T^2\mu^2}{4e^{-2\gamma_E}}\right) - 2\gamma^q\right] B_{q/N}(z,x_T^2,\mu^2), \tag{1.121}$$

where $\Gamma^F_{\text{cusp}}$ is the cusp anomalous dimension in the fundamental representation and $\gamma^q$ is the quark anomalous dimension. For the case of gluon-initiated processes, $B_{g/N}$, $\Gamma^F_{\text{cusp}}$ and $\gamma^q$ are replaced with $\Gamma^A_{\text{cusp}}$ and $\gamma^g$ respectively.

When $x_T \ll \Lambda^{-1}_{\text{QCD}}$, $B_{i/j}(z, x_T^2)$ can be expressed by the operator product expansion of the form [33, 38]

$$B_{i/N} = \sum_j I_{i/j} \otimes \phi_{j/N} + \mathcal{O}\left(x_T^2 \Lambda^2_{\text{QCD}}\right), \tag{1.122}$$

where $\phi_{j/N}$ are the collinear PDFs, and $\otimes$ denotes Mellin convolution

$$A(z) \otimes B(z) \equiv \int_z^1 \frac{d\xi}{\xi} A(z/\xi) B(\xi). \tag{1.123}$$

Factorization (1.113) and matching (1.122) described above are schematically shown in Fig. 1.5.

Naturally, one cannot compute the hadronic matrix elements of Eq. (1.111) perturbatively. However, Eq. (1.122) (or an analogous expansion of $\mathcal{B}_{i/N}(z, x_T^2)$) enables one to obtain the matching kernels $I_{i/j}$ from the parton-to-parton beam functions $B_{i/j}$. Hadron-to-parton beam functions can then be constructed from the convolution of these matching kernels with standard collinear PDFs.

## 1.4 Sector decomposition and selector functions

As we will see in Chapter 2, phase-space integrals of scattering amplitudes involve expansion around singularities. The objective of this section is to introduce techniques, that enable one to transform integrands in which the divergences are factorised as simple monomials.

To introduce the key concepts, we will use a toy model which simulates the inte-

grand in $d$ dimensions:

$$I = \int_0^1 dx_1 dx_2 ((x_1 - x_2)^2)^{-\frac{1}{2}+\epsilon} (x_1 + x_2)^{-1} (1 - x_2)^{-1-\epsilon}. \tag{1.124}$$

In the above one can consider also an implicit factor which is regular everywhere, but as it does not affect the argument, it will be left implicit. This integral cannot be evaluated numerically since the integrand is divergent when

$$x_1 = x_2, \tag{1.125}$$
$$x_1 = 0 \;\&\; x_2 = 0, \tag{1.126}$$
$$x_2 = 1\,. \tag{1.127}$$

Thus, one has to first extract the divergences as $1/\epsilon$ poles in the Laurent expansion, and only after that can one evaluate the coefficient numerically. To this end, one first needs the divergences to be factorized as monomials. In general, the integrands at hand have complex structure of divergences, where Eq. (1.124) exhibits three types of non-monomial divergences. Here, the case corresponding to $x_1 - x_2$ and $x_1 + x_2$ are termed *manifold* and *overlap* type singularities respectively. The condition (1.125) correspond to the former, whereas, the condition (1.126) corresponds to the latter. The divergence of the type (1.127) is called *end-point* singularity.

In order to transform the integrand such that all the divergences occur in the monomial form, two techniques are to be introduced here. One is called *sector decomposition* [43, 44] and the other is known as *selector functions* [45–47].

Let us start with sector decomposition. The idea of sector decomposition is that one cuts the phase space into sectors, such that, in each sector, the divergences are at the end point of phase space, and by applying changes of variables, one can construct a set of sectors in which the divergences are all in simple forms of monomials. The schematic view of the process is depicted in Fig. 1.6a. One can demonstrate this in Eq. (1.124) as follows. Firstly, one inserts

$$1 = \theta(x_1 - x_2) + \theta(x_1 - x_2)\,, \tag{1.128}$$

thus cutting along the line $x_1 = x_2$. Then, applying the changes of variables $x_1 \to (1 - x'_1)x_2$ and $x_2 \to x_1(1 - x'_2)$ to the respective sectors yields

$$\begin{aligned} I = &\int_0^1 dx'_1 \int_0^1 dx_2\; x_2^{-1-\epsilon} x'^{-1-\epsilon}_1 (2 - x'_1)^{-1} (1 - x_2)^{-1-\epsilon} \\ &- \int_0^1 dx_1 \int_0^1 dx'_2\; x_1^{-1-\epsilon} x'^{-1-\epsilon}_2 (2 - x'_2)^{-1} (1 - x_1 + x_1 x'_2)^{-1-\epsilon}. \end{aligned} \tag{1.129}$$

Let us first consider the first term. Here, one has the divergences at $x_1 = 0$ and $x'_2 = 0$ as desired, and another at $1 - x_2 = 0$, which can be turned into the divergence at 0 simply by cutting the sector at $x_2 = 1/2$ and applying $x_2 \to x'_2/2$ and $x_2 \to (1 - x'_2/2)$, respectively. In this method, one cuts the phase space as demonstrated above and obtains a set of sectors with simple, explicit form of divergences.

Now, let us turn to the case of the second term in Eq. (1.129). The two poles

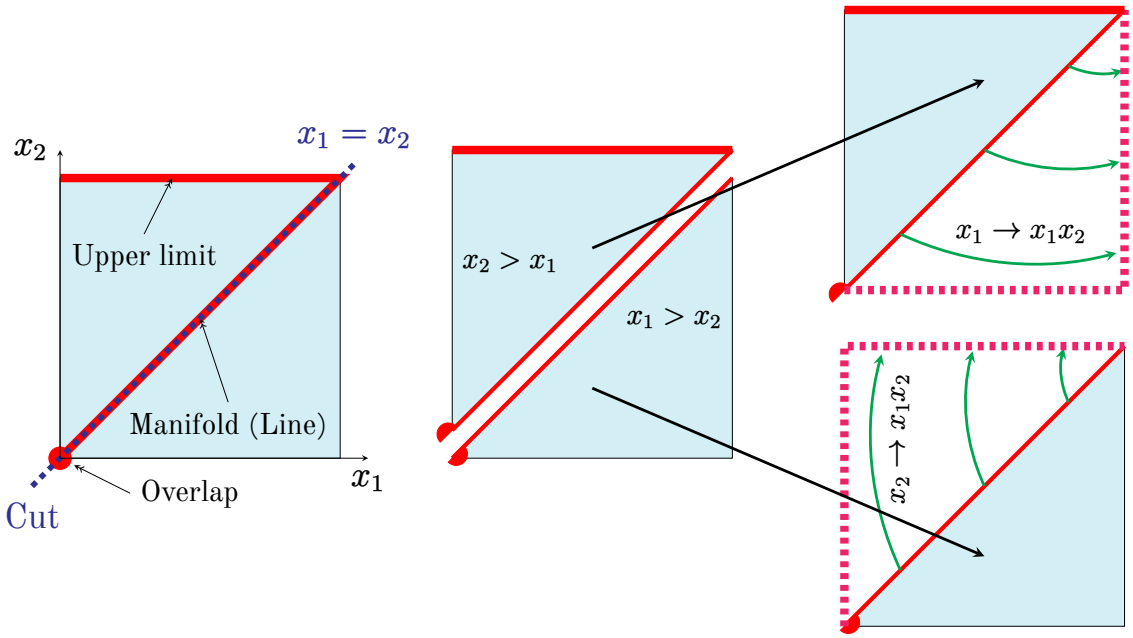


(a) Schematic view of sector decomposition. Various types of divergences are shown in red. After changes of variables, the overlap and manifold types become end-point singularities (pink dashed).

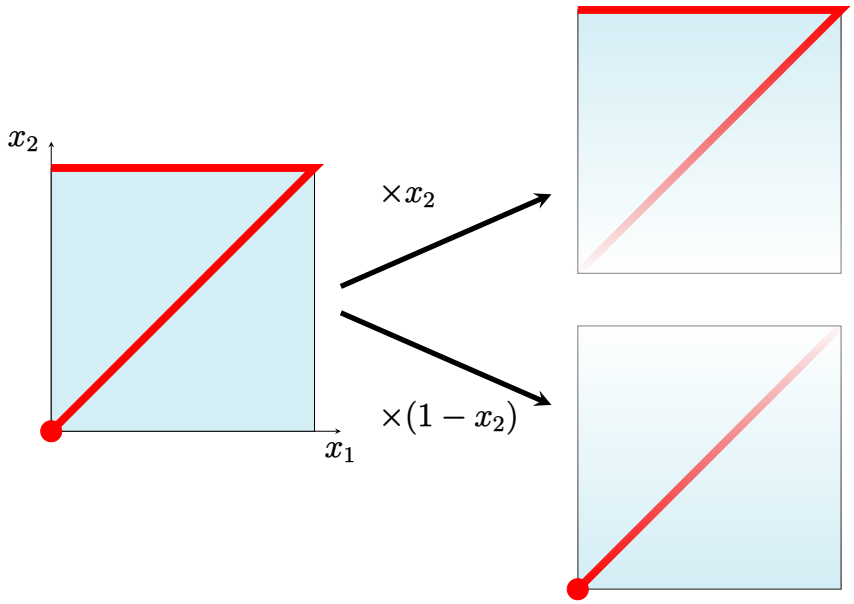


(b) Schematic view of decomposition by the selector functions. Selector functions do not deform the space but simply select subsets of singularities. One applies the sector decomposition on those selected singularities.

Figure 1.6

of $x_1^{-1-\epsilon}$ and $x_2^{-1-\epsilon}$ are in the required from, however, we have another one which is an overlapping-type divergence. Naturally, one may use the above technique until all the divergences are sorted out, but it may be simpler if, instead of using theta functions, one used smooth functions which can selectively suppresses the divergences (Fig. 1.6b). This is the idea of the selector functions. The advantage of the method is that one does not necessarily need to use changes of variables thus there is less danger of complicating the expressions, which make the integration prone to numerical inaccuracies. Another benefit is that one can keep track of the physical meanings of each divergence. For the above case, instead of going straight to the sector decomposition, let us multiply the integral (1.124), by the selector functions

$$1 = x_2 + (1 - x_2). \tag{1.130}$$

One can see that the first term suppresses the divergence at $x_2 = 0$ and the second term suppresses the one at $x_2 = 1$. Let us first consider the term multiplied by $(1-x_2)$, which, after the sector decomposition $x_1 \to x_1 x_2$ and $x_2 \to x_1 x_2$, is given by

$$\begin{aligned} I_{1-x_2} = &\int_0^1 dx_1 dx_2\, x_2^{-1+\epsilon}(1-x_1)^{-\epsilon}(1-x_1)^{-1+2\epsilon}(1+x_1)^{-1-\epsilon} \\ &+ \int_0^1 dx_1 dx_2\, x_1^{-1+\epsilon}(1-x_1x_2)^{-\epsilon}(1-x_2)^{-\epsilon}(1-x_2)^{-1+2\epsilon}(1+x_2)^{-1-\epsilon}. \end{aligned} \tag{1.131}$$

This form contains only the divergences at 0 and 1, and what was not in a simple form is suppressed by the selector function. Similarly, the other term becomes

$$\begin{aligned} I_{x_2} = &\int_0^1 dx_1 dx_2\, x_2^{-1+\epsilon}(1-x_1)^{-1+2\epsilon}\frac{1-x_2}{((1-x_1x_2)+(1-x_2))^{1+\epsilon}} \\ &+ \int_0^1 dx_1 dx_2\, x_1^{-1+\epsilon}x_2^{-1-\epsilon}(1-x_2)^{-1+2\epsilon}\frac{1-x_1x_2}{((1-x_1)+(1-x_1x_2))^{1+\epsilon}}. \end{aligned} \tag{1.132}$$

Again, all the divergences occur at 0 or 1.

Once all the divergences are factored out in the monomial form, one can extract the poles as a Laurent expansion. This is achieved by the so-called *plus prescription*:

$$\begin{aligned} \int_0^1 dx x^{-1-\epsilon} f(x;\epsilon) &= -\frac{1}{\epsilon} f(0;\epsilon) + \int_0^1 dx \frac{f(x;\epsilon) - f(0;\epsilon)}{x^{1+\epsilon}} \\ &= -\frac{1}{\epsilon}\int_0^1 dx \delta(x) f(x;\epsilon) + \int_0^1 dx \left[x^{-1-\epsilon}\right]_+ f(x;\epsilon), \end{aligned} \tag{1.133}$$

where $f(x;\epsilon)$ is regular everywhere and $[\dots]_+$ is the plus distribution.

Integrands which appear on the right-hand side of Eq. (1.133) are regular, and all remaining integrations can be performed numerically by expanding the integrand around $\epsilon = 0$. While, in principle, the integral $\int_0^1 dx \left[x^{-1}\right]_+ f(x)$ is finite, one needs to pay extra attention near the point $x = 0$, as the integrand behaves as $\sim 0/0$ and having a good control of the numerical accuracy is critical.

As demonstrated above, one can limit the use of sector decompositions only to the cases of manifold and overlap types of singularities and the rest can be treated with the

selector functions. Moreover, as it will be discussed later, evaluation of $\lim_{x\to 0} f(x)$ becomes highly non-trivial at N$^3$LO.

## 1.5 Small-$x$ and gluon density

As discussed in Sec 1.2.1, in the moderate-$x$ regions the parton distribution functions are obtained from the starting distribution $f(x, Q_0)$ and the DGLAP evolution. The evolution equations determine the $Q$ dependence of the PDFs and resum large logarithms of $Q$. By examining the AP splitting kernels, Eqs. (1.43)–(1.45), one sees that, as $x \to 0$ (Regge–Gribov limit), the emissions of gluons dominate due to the denominator $z$. In this region, therefore, one is primarily concerned about gluon densities in the proton [12].

In the small-$x$ limit, the Regge theory predicts [13]

$$F_2 \sim \beta_P x^{\alpha_P - 1} + \beta_R x^{\alpha_R - 1}, \tag{1.134}$$

where $\alpha_P \sim 1$ and $\alpha_R \sim 1/2$ are the Pomeron and Reggeon trajectories, respectively. One can interpret the two terms in the following way. The first, Pomeron term, determines the effects of flavour singlet sea-quarks and gluons, while the second, the Reggeon term, determines the valence-quarks contributions [13]. In Eq. (1.134), the limit $x \to 0$ is approximately a constant: $x^{\alpha_P - 1} \sim x^0$. However, experimental data (see Fig. 4.2 of Ref [13]) show a rise with decreasing $x$. We will see presently that this can be partially described by the double asymptotic limit of DGLAP evolution, where one takes double-leading-logarithm approximation (DLLA), namely resumming $(\alpha_s \ln(Q/Q_0) \ln(1/x))^n$. For this analysis, it is convenient to move to Mellin space:

$$\tilde{f}(j) = \int_0^\infty x^{j-1} f(x) dx, \tag{1.135}$$

$$f(x) = \frac{1}{2\pi i} \int_{c-i\infty}^{c+i\infty} x^{-j} \tilde{f}(j) dj. \tag{1.136}$$

A key feature of the above transformation is that the convolution of Eq. (1.123) becomes a simple product. Therefore, noticing that the small-$x$ limit corresponds to $j = 1$, and the Mellin moments of the splitting functions, $\gamma_{gg}^{(0)}$ and $\gamma_{qq}^{(0)}$, are divergent, the DGLAP equation for the gluon PDF takes the form

$$\mu \frac{\partial \tilde{g}(j,\mu)}{\partial \mu} = \frac{\alpha_s(\mu)}{2\pi} \gamma_{gg}^{(0)}(j) \tilde{g}(j,\mu), \qquad \gamma_{gg}^{(0)}(j) \approx \frac{2C_A}{j-1}, \tag{1.137}$$

and its solution reads

$$\tilde{g}(j,\mu^2) = \tilde{g}(j,\mu_0^2) \exp\left[\frac{\xi}{(j-1)}\right], \quad \text{where} \quad \xi = \frac{C_A}{\pi\beta_0} \ln\left(\frac{\ln(\mu^2/\Lambda^2)}{\ln(\mu_0^2/\Lambda^2)}\right). \tag{1.138}$$

The inverse Mellin transform gives

$$xg(x,\mu) = \frac{-i}{2\pi}\int dj \tilde{g}(j,\mu_0^2)\exp\left[(j-1)\ln(1/x) + \frac{\xi}{(j-1)}\right]. \tag{1.139}$$

This integral can be approximated by expanding the integrand in $j$ around the saddle point $j_0 = 1+\sqrt{\frac{\xi}{\ln(1/x)}}$. Then, the asymptotic solution reads [13]

$$xg(x,\mu^2) \approx \tilde{g}(j_0,\mu_0^2)\exp\left[2\sqrt{\xi\ln(1/x)}\right]. \tag{1.140}$$

The $x$ dependence can be characterized by the exponent if the initial distribution, $\tilde{g}(j_0,\mu_0^2)$, is approximately a constant, and this solution is only valid if $\tilde{g}(j_0,\mu_0^2)$ does not behave too steeply in the limit $x \to 0$ [13]. (The growth is weaker than power of $1/x$, yet stronger than any power of $\ln(1/x)$, as noted in Ref. [48].)

Therefore, in the large-$Q^2$, small-$x$ limit, DGLAP evolution predicts a rise of the structure function. However, as one reaches even smaller-$x$ or low-$Q^2$ regions, one needs the full leading-$\ln(1/x)$ approximation which is described by the Balisky–Fadin–Kraev–Lipatov (BFKL) equation. The BFKL equation resums leading $\ln(1/x)$ with not only the leading $\ln(Q^2)$, which was the case in DLLA, but with full $Q^2$ dependence [13]. The phase space has a strong $x$-ordering,

$$x \ll x_1 \ll x_2 \ll \cdots \ll x_0, \tag{1.141}$$

instead of the strong $k_T$-ordering (1.48), which was present in the DGLAP case. The BFKL equation is a linear evolution equation in $x$, and can be schematically written as [13]

$$\frac{\partial\mathcal{F}}{\partial\ln(1/x)} = \mathcal{K}_{\mathrm{BFKL}}\otimes\mathcal{F}, \tag{1.142}$$

where the *unintegrated gluon density*, $\mathcal{F}$, appears in the $k_T$-factorization formula, which we will discuss in more detail in Sec. 1.6, and $\mathcal{K}_{\mathrm{BFKL}}$ is the BFKL evolution kernel.

The BFKL equation has two well-known problems [13, 49]. One of them is that when it reaches high rapidity $Y = \ln(1/x)$, the transverse momentum may enter non-perturbative region [13, 49, 50]. This effect is called *infrared diffusion*. The other problem concerns more with what we are interested in here: the well-known prediction of leading order BFKL equation is a power-like rise of the structure function

$$F_2 \sim x^{-\frac{4C_A\alpha_s}{\pi}\ln(2)}, \tag{1.143}$$

in the small-$x$ limit. Asymptotically, however, the unitarity (Froissart) bound restricts the rise to be [13, 49]

$$\sigma_{\mathrm{total}} \lesssim \ln^2(s), \tag{1.144}$$

which is clearly in disagreement with the BFKL prediction. While the unitarity bound does not tell whether the cross section grows maximally or slower, the analysis of

Ref. [49] suggests, indeed, the $\ln^2(1/x)$ behaviour. The disagreement will not be resolved even when higher order results are included [51].

In an attempt to account for saturation, Gribov, Levin and Ryskin [52] and Muller and Qiu [53] proposed a nonlinear extension to DGLAP equation [12]:

$$\begin{aligned}\frac{\partial g(x,Q^2)}{\partial \ln(Q^2)} = \frac{\alpha_s C_A}{\pi}\int_x^1 \frac{dy}{y} y g(y,Q^2) \\ -\frac{4\pi^3}{N_c^2-1}\left(\frac{\alpha_s C_A}{\pi}\right)^2 \frac{1}{Q^2}\int_x^1 \frac{dy}{y} y^2 g^{(2)}(y,Q^2),\end{aligned} \tag{1.145}$$

where the two-gluon correlation function $g^{(2)}(x,Q^2)$ is often expressed as

$$x g^{(2)}(x,Q^2) = \frac{\left(x g(x,Q^2)\right)^2}{\pi R^2}, \tag{1.146}$$

with an effective proton radius $R$. The main feature of Eq. (1.145) is the second term, which compensates the rise of $g(x,Q^2)$ as the gluon density becomes high. At the scale $Q \sim Q_s$, the first and the second term become similar in strength, thus the growth of the gluon density is tamed. The scale, $Q_s$, characterising transition to the saturation regime is called the *saturation scale*.

A similar extension to the BFKL equation was proposed by Balitsky and Kovchegov (BK), in which the recombination term was included to be [54–56]

$$\begin{aligned}\frac{\partial \mathcal{N}(r_0,Y)}{\partial Y} = \int \frac{d^2z}{2\pi} K_{\mathrm{BFKL}}(r_0,r_1,r_2) \\ \times\left[\mathcal{N}(r_1,Y)+\mathcal{N}(r_2,Y)-\mathcal{N}(r_0,Y)-\mathcal{N}(r_1,Y)\mathcal{N}(r_2,Y)\right],\end{aligned} \tag{1.147}$$

where

$$K_{\mathrm{BFKL}}(r_0,r_1,r_2) = \frac{\alpha_s N_c}{\pi}\frac{r_0^2}{r_1^2 r_2^2}, \tag{1.148}$$

and

$$r_0 = x-y, \qquad r_1 = x-z, \qquad r_2 = z-y, \tag{1.149}$$

where $x$ and $y$ are the transverse positions of $q$ and $\bar{q}$ in the colour dipole, and $z$ is the transverse position of additionally emitted gluon. The above form of the BK equation is given in the so-called *dipole formalism*, with the dipole amplitude $\mathcal{N}$, which is directly related to the gluon density as we shall discuss further in the next section. The BFKL equation (1.148) can also be formulated in this framework, which corresponds to Eq. (1.148) without the last non-linear term. [13]. As it was pointed out in Ref. [57], also the running coupling in Eq. (1.148) has considerable effects.

It was shown in Ref. [58] that the BK evolution equation exhibits asymptotic solution at large $Y$, a property called *geometric scaling* [59]. It means that in the saturated region, the dipole amplitude depends only on one variable:

$$\mathcal{N}(r,Y) \to \mathcal{N}(rQ_s), \tag{1.150}$$

where $\ln(Q_s) \sim Y$.

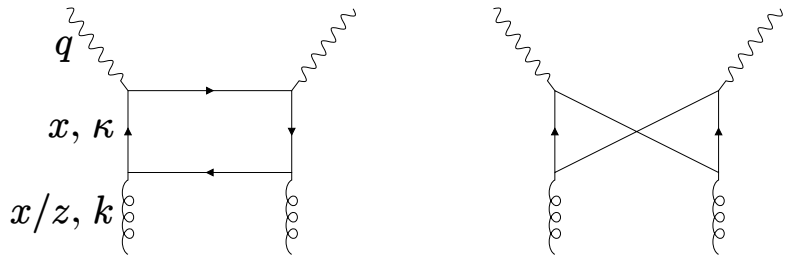


Figure 1.7: Kinematic variables of the gluon contribution to $F_2$. The momentum fraction of the gluon is $x/z$ as it has to contribute via the quark box. While, in the DGLAP case, the crossed rung digrams were sub-leading, in the small-$x$ case, the diagram on the right-hand side contributes at the leading order.

## 1.6 DIS at small $x$ and the dipole formalism

In this section, the inclusive DIS process depicted in Fig. 1.3,

$$e + p \to \gamma^*(q) + p(p) \to e + X, \tag{1.151}$$

will be considered. In the region where $x \sim 0.3$, the dominant contribution comes from the valence quarks (see for example MMHT PDFs [60, 61]). As $x$ decreases, the sea quarks come into play. However, it was observed that the momentum fractions carried by the quarks and anti-quarks do not add up to 1, and about a half of the total proton momentum is carried by the gluons [12]. At LO, gluons do not interact directly with the photon, and thus are suppressed. However, as $x$ decreases further, gluons quickly dominate over other partons (see for example Refs. [60–62]), which can be seen from the divergent term of the AP evolution kernels (1.43)–(1.46). For this reason, in the small-$x$ region, it is reasonable to only consider gluons. The evolution, therefore, occur predominately via the process $g \to gg$, and the LO DIS interaction happens through a quark box depicted in Fig. 1.7.

For a moderate to large $x$, inclusive DIS is described sufficiently well with collinear factorization (1.41). As one approaches the small-$x$ region, resummation of the large logarithms, $\log(1/x)$, is necessary, thus a new type of factorization, called the $k_T$-factorization (high-energy factorization) [63–68], should be used. In this section, $k_T$-factorization of the $F_2$ structure function is outlined.

The Sudakov decompositions of $k$ and $\kappa$ (Fig. 1.7), with $p$ and $q' \equiv q + xp$, read

$$\kappa = \alpha p - \beta q' + \kappa_T \qquad \text{and} \qquad k = ap - bq' + k_T. \tag{1.152}$$

Then, the contributions to the structure function $F_2$, depicted in Fig. 1.7 for trans-

versely and longitudinally polarized photons, factorize in the form [62, 69]

$$F_T(x,Q^2) = \sum e_f^2 \frac{Q^2}{4\pi} \int \frac{dk_T^2}{k_T^2} \int_0^1 d\beta \int d\kappa_T^2 \frac{d\phi}{2\pi} \alpha_s(\mu^2) \mathcal{F}^{\text{dipole}}(x/z, k_T^2, \mu^2)$$
$$\Theta(1-x/z) \times \left[ \left[\beta^2 + (1-\beta)^2\right] \left( \frac{\boldsymbol{\kappa}_T}{D_1} - \frac{\boldsymbol{\kappa}_T - \mathbf{k}_T}{D_2} \right)^2 + m_f^2 \left( \frac{1}{D_1} - \frac{1}{D_2} \right)^2 \right], \tag{1.153}$$

$$F_L(x,Q^2) = \sum e_f^2 \frac{Q^2}{4\pi} \int \frac{dk_T^2}{k_T^2} \int_0^1 d\beta \int d\kappa_T^2 \frac{d\phi}{2\pi} \alpha_s(\mu^2) \mathcal{F}^{\text{dipole}}(x/z, k_T^2, \mu^2)$$
$$\Theta(1-x/z) \times \left[ 4Q^2\beta^2(1-\beta)^2 \left( \frac{1}{D_1} - \frac{1}{D_2} \right)^2 \right], \tag{1.154}$$

where

$$\frac{1}{z} = 1 + \frac{\kappa_T'^2 + m_f^2}{\beta(1-\beta)Q^2} + \frac{k_T^2}{Q^2}, \tag{1.155}$$

and

$$\begin{aligned} D_1 &= \kappa_T^2 + \beta(1-\beta)Q^2 + m_f^2, \\ D_2 &= (\boldsymbol{\kappa}_T - \mathbf{k}_T)^2 + \beta(1-\beta)Q^2 + m_f^2. \end{aligned} \tag{1.156}$$

In $k_T$-factorization, the long-distance effects are absorbed into the dipole gluon density (unintegrated gluon density) $\mathcal{F}^{\text{dipole}}$. The unintegrated gluon density is related to the integrated gluon density, for large $Q$, hence in the DLLA limit, by [48, 70–72]

$$xg(x,Q^2) = \int_0^{Q^2} dk_T^2 \mathcal{F}^{\text{dipole}}(x, k_T^2). \tag{1.157}$$

More precisely, in Eqs. (1.153) and (1.154) $F_T$ and $F_L$ are factorized into the hard part describing $\gamma^* g \to q\bar{q}$ (Fig. 1.7) and the gluon density $\mathcal{F}^{\text{dipole}}$. The dipole gluon density here is described by the BFKL evolution equation [13], which resums large $\ln(1/x)$. One should note that, since the gluons are not directly probed by the photon, the argument of $\mathcal{F}^{\text{dipole}}$ is $x/z$ instead of $x$.

Now, let us revisit the derivation of the dipole-factorization formula in Refs. [69, 70] and show that the difference boils down to replacing $x/z$ with $\tilde{x} \equiv x\left(1 + 4m_f^2/Q^2\right)$ of Ref. [73].

With the result of Refs. [69, 70], outlined also in App. C.1, one has

$$\int \frac{d^2\boldsymbol{\kappa}_T}{2\pi} \left( \frac{1}{D_1} - \frac{1}{D_2} \right)^2 = \int \frac{d^2\mathbf{r}}{2\pi} \left| 1 - e^{i\mathbf{k}_T \cdot \mathbf{r}} \right|^2 K_0^2(N_1 r), \tag{1.158}$$

$$\int \frac{d^2\boldsymbol{\kappa}_T}{2\pi} \left( \frac{\boldsymbol{\kappa}_T}{D_1} - \frac{\boldsymbol{\kappa}_T - \mathbf{k}_T}{D_2} \right)^2 = N_1^2 \int \frac{d^2\mathbf{r}}{2\pi} \left| 1 - e^{i\mathbf{k}_T \cdot \mathbf{r}} \right|^2 K_1^2(N_1 r). \tag{1.159}$$

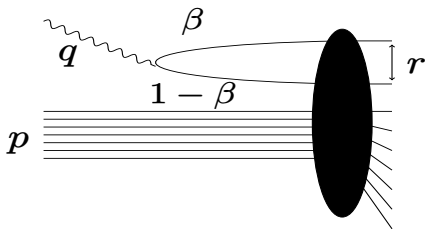


Figure 1.8: The dipole picture of DIS and its kinematic variables.

Inserting the above back to Eqs. (1.153) and (1.154), one obtains

$$\sigma_{\text{dipole}}(x/z,r)=\frac{2\pi}{3}\int\frac{d^2\mathbf{k}_T}{k^2}\alpha(\mu^2)\mathcal{F}^{\text{dipole}}(x/z,k_T^2)\left|1-e^{i\mathbf{k}_T\cdot\mathbf{r}}\right|^2. \tag{1.160}$$

Then, assuming no implicit $k_T$ dependence, one arrives at the dipole factorization formula of Refs. [69, 73]

$$\begin{aligned}F_T(x,Q^2)=6\sum e_f^2\frac{Q^2}{4\pi^2}\int_0^1 d\beta\int\frac{d^2\mathbf{r}}{(2\pi)^2}\sigma_{\text{dipole}}(x/z,r)\Theta(1-x/z)\\ \left[\left[\beta^2+(1-\beta)^2\right]N_1^2K_1^2(N_1r)+m_f^2K_0^2(N_1r)\right],\end{aligned} \tag{1.161}$$

$$\begin{aligned}F_L(x,Q^2)=6\sum e_f^2\frac{Q^2}{4\pi^2}\int_0^1 d\beta\int\frac{d^2\mathbf{r}}{(2\pi)^2}\sigma_{\text{dipole}}(x/z,r)\Theta(1-x/z)\\ \left[4Q^2\beta^2(1-\beta)^2K_0^2(N_1r)\right].\end{aligned} \tag{1.162}$$

Hence, factorization of the structure function Eqs. (1.161) and (1.162), can be written compactly in the from [69, 73]

$$F_p\left(x,Q^2\right)=\sum_f e_f\frac{Q^2}{4\pi^2}\int_0^1 d\beta\int\frac{d^2\mathbf{r}}{(2\pi)^2}\left|\Psi_p\left(\tilde{x},\beta,Q^2\right)\right|^2\sigma_{\text{dipole}}\left(\tilde{x},r\right), \tag{1.163}$$

where $p=T$ or $L$, the photon wave function, $\left|\Psi\left(x,\beta,Q^2\right)\right|^2$, describes a splitting of the incoming photon into a $q\bar{q}$ pair with light-cone momenta fractions $\beta$ and $1-\beta$ respectively, and the dipole cross section, $\sigma_{\text{dipole}}\left(x,r\right)$, describes the interaction of the colour dipole with the proton. Eq. (1.163) tells us that in the small-$x$ limit, the DIS process can be seen as an interaction between a proton and a $q\bar{q}$ colour-dipole, as depicted in Fig. 1.8.

In the above derivation, it was assumed that only $e^{i\boldsymbol{\kappa}_T\cdot(\mathbf{r}-\mathbf{r}')}$ depends on $\boldsymbol{\kappa}_T$, which resulted in $\delta^2\left(\mathbf{r}-\mathbf{r}'\right)$ ( see App. C.1). This means that the dipole size is constant throughout the process [70]. This assumption is indeed not true if we consider the definition of $z$ in Eq. (1.155). It is a subtle but an important difference between the two schemes. In Ref. [73], $\tilde{x}=x_{Bj}\left(1+\frac{4m_f^2}{Q^2}\right)$ was used to suppress the regions, where $Q<2m_f$, such that the photo-production limit ($Q^2\to 0$) can be studied. From the derivation above, it is now clear that $\tilde{x}$ naturally arises from $x/z$ in Eqs. (1.153) and

(1.154). Comparing with Eq. (1.155), this is the minimum value of $1/z$ where $k_T = \kappa' = 0,\ \beta = 1/2$. This assumption motivates one to introduce massive light quarks to replace the non-zero $k_T$ and $\kappa'_T$. Another subtlety is that in the above derivation, the coupling $\alpha_s$ was considered to be independent of $\boldsymbol{\kappa}_T$, if not constant. If one considers the running coupling with $\boldsymbol{\kappa}_T$ dependence, *cf.* Refs. [62, 74], the dipole factorization becomes incorrect [70].

In Eq. (1.160), the term multiplied by 1 corresponds to the case where the gluons (wave function and the complex conjugate) connect to the same quark/anti-quark, and the term multiplied by $e^{i\mathbf{k}_T\cdot\mathbf{r}}$ corresponds to the case where the gluons connect to different quark/anti-quark (*cf.* Fig. 1.7). Eq. (1.160) can be inverted, and thus the dipole cross section, $\sigma_{\text{dipole}}(x, r)$, and the dipole unintegrated gluon distribution, $\mathcal{F}^{\text{dipole}}(x, k_T^2)$, are related to each other by [69, 70, 75]

$$\sigma_{\text{dipole}}(x, r) = \frac{4\pi}{N_c}\int \frac{d^2\mathbf{k}_T}{k_T^2}\alpha_s\mathcal{F}^{\text{dipole}}(x, k_T^2)(1 - e^{i\mathbf{k}_T\cdot\mathbf{r}}), \tag{1.164}$$

$$\alpha_s\mathcal{F}^{\text{dipole}}(x, k_T^2) = \frac{N_c}{4\pi}\int \frac{d^2\mathbf{r}}{(2\pi)^2}e^{i\mathbf{k}_T\cdot\mathbf{r}}\nabla_{\mathbf{r}}^2\sigma_{\text{dipole}}(x, r). \tag{1.165}$$

Using Eqs. (1.165) (1.157), it is straight-forward to see that [70]

$$\begin{aligned}\lim_{r\to 0}\sigma_{\text{dipole}} &\simeq \frac{\pi^2 r^2}{N_c}\int_0^{1/r^2} dk_T^2\alpha_s\mathcal{F}(x, k_T^2)\\ &\simeq \frac{\pi^2 r^2\alpha_s x g(x, 1/r^2)}{N_c}.\end{aligned} \tag{1.166}$$

The behaviour of the dipole cross section in this region, $\sigma_{\text{dipole}} \sim r^2$, is referred to as *colour transparency* [69, 76], which means that the dipole effectively becomes colourless as it gets smaller.

In dipole factorization, the dipole cross section is an object which describes the long distance effects. While there are evolution equations, most notably the BK equation, which describe dependences on $x$, the dipole cross section requires, to an extent, a model. In Sec. 3.1.1, a brief overview of some successful models will be given.

Before ending the section, let us outline a few important points on another type of gluon density[5], called the Weizsäker-Williams (WW). The WW gluon density is a number density of gluons [79, 80]. It was shown in Ref. [81], that in the large-$N_c$ limit, various gluon densities appearing in the (I)TMD factorization (*cf.* Sec. 1.8) can be expressed in terms of the WW and dipole gluon densities.

Furthermore, when one considers the assumption that the colour charge density distribution of the target is Gaussian [80, 82], the WW gluon density can be obtained from [79, 80, 83, 84]

$$\alpha_s\mathcal{F}^{\text{WW}}(x, k^2) = \frac{C_F}{\pi^2}2\int d^2b\int \frac{d^2r}{(2\pi)^2}\frac{1}{r^2}e^{-ik\cdot r}\mathcal{N}_{\text{Adj}}, \tag{1.167}$$

[5]For more involved processes such as double-virtual Compton scattering, one need to consider Generalized Parton Distributions (GPDs) [77, 78]. However for our discussion, we will only consider two, namely the dipole and WW gluon densities.

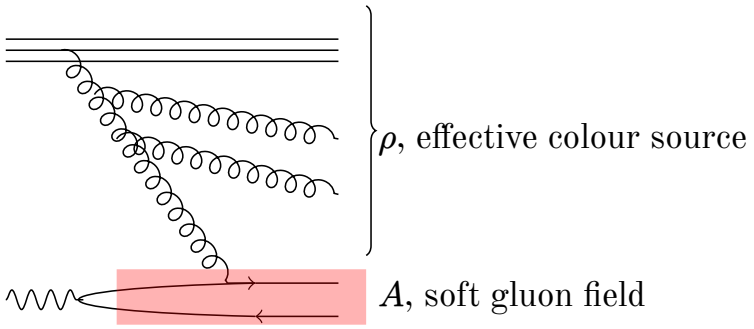


Figure 1.9: CGC view of the dipole-proton interaction [86]. Proton valence quarks (three lines at the top) emit particles with momenta $p_+ > xp_P$, which become effective colour source, $\rho$, inducing a gluon field $A$. The interaction of a dipole with $A$ is described by Wilson lines.

where the adjoint dipole amplitude is related to the fundamental one by [83, 85]

$$\mathcal{N}_{\text{Adj}} = 1 - (1 - \mathcal{N})^{C_A/C_F}. \tag{1.168}$$

In the large-$k_T$ limit, both of the above two gluon densities are expected to behave similarly like $\sim k_T^{-2}$ [80]. However, in the small-$k_T$ limit, their behaviour differs substantially: $\mathcal{F}^{\text{dipole}} \sim k_T^2$ and $\mathcal{F}^{\text{WW}} \sim \log(k_T^2)$ [80].

## 1.7 Colour glass condensate

Color Glass Condensate (CGC) [48, 49, 86, 87] is an effective theory of high density gluon system. Let us consider $\gamma - p$ collision in the infinite momentum frame, where the hadron carry the most of the momentum, *cf.* Fig. 1.9. Two degrees of freedom are defined in CGC: the colour source (fast partons), $\rho$, frozen in time, and a dynamical soft gluon field induced by the source, $A$ as depicted in Fig. 1.9. For the soft gluons with high occupational number, the classical description is valid. These two degrees of freedom are separated in the corresponding light-cone momentum by a scale $\Lambda_+$. (Notice the strong ordering in $x$ means strong ordering in the light cone momentum $p_+$.) The classical equation of motion reads:

$$\left(D_\mu F^{\mu\nu}\right)_a (x) = \delta^{\mu+} \rho_a (x_-, x_\perp) . \tag{1.169}$$

The physical observables, such as cross sections, are weighted averages of the solution of this equation. The non-linear effects in Eq. (1.169) describe recombinations of gluons.

The expectation value of an operator $O$ is obtained from a functional integral

$$\langle O \rangle_{\Lambda_+} \equiv \int [D\rho] \, W_{\Lambda_+} [\rho] \, O [\rho] , \tag{1.170}$$

with the weight functional $W_{\Lambda_+}[\rho]$ of colour charge density $\rho$. The integral in Eq. (1.170) averages the expectation value $O[\rho]$ over a random distribution of $\rho$. The weight $W$ is universal, like PDFs, while it contains all twist contribution.

For example, in the McLerran–Venugopalan (MV) model for large nucleus $A$, a

Gaussian weight is given by [86]

$$W_A[\rho] = \mathcal{N} \exp\left[-\frac{1}{2}\int d^3x \frac{\rho_a^2(x^-, x_\perp)}{\lambda_A(x^-)}\right], \tag{1.171}$$

where $\lambda_a(x^-)$ is the average of $\rho_a^2(x^-, x_\perp)$.

As we go lower in $x$, the dominant colour sources become gluons. The MV weight can be evolved in the separation scale $\Lambda_+$ in a RGE called the JIMWLK equation [49, 86]:

$$\frac{\partial W_{\Lambda_+}[\rho]}{\partial \ln(\Lambda_+)} = -\mathcal{H}\left[\rho, \frac{\delta}{\delta\rho}\right] W_{\Lambda_+}[\rho] \tag{1.172}$$

were the evolution kernel, $\mathcal{H}$, is called the JIMWLK Hamiltonian.

The BK and JIMWLK equations are related to each other such that the BK equation is a large-$N_c$ limit of a mean field approximation of the JIMWLK equation. In fact, it was observed that the differences, despite of the approximations, are small [49].

The dipole cross section in CGC can be viewed as a scattering cross section of a colour dipole with the field of soft gluons induced by the charged source $\rho$. Recalling that the Wilson line resums interactions of a quark with soft gluons in eikonal approximation, the $S$ matrix for the dipole cross section can be written in terms of the fundamental representation Wilson line $U$ [6] as

$$\sigma_{\text{dipole}} = 2\int d^2b\,(1-S) = 2\int d^2b\left(1 - \frac{1}{N_c}\left\langle \operatorname{tr} U(x)U^\dagger(y)\right\rangle_{x_g}\right). \tag{1.173}$$

Consequently, in CGC, the dipole gluon density is defined as [80, 88]

$$xG^{(2)} = \frac{q_\perp^2 N_c}{2\pi^2\alpha_s} S_\perp \int \frac{d^2r_\perp}{(2\pi)^2} e^{-iq_\perp\cdot r_\perp} \frac{1}{N_c}\left\langle \operatorname{tr} U(0)U^\dagger(r_\perp)\right\rangle_{x_g}. \tag{1.174}$$

From the JIMWLK equation, one obtains

$$\begin{aligned}\frac{\partial}{\partial Y}\left\langle \operatorname{tr} U(x)U^\dagger(y)\right\rangle_{x_g} = &-\frac{\alpha_s}{2\pi^2 N_c}\int d^2z \frac{(x-y)^2}{(x-z)^2(y-z)^2} \\ &\times\left[\left\langle U^\dagger(x)U(y)\right\rangle_{x_g} - \frac{1}{N_c}\left\langle \operatorname{tr}\left(U^\dagger(x)U(y)\right)\operatorname{tr}\left(U^\dagger(z)U(y)\right)\right\rangle_{x_g}\right].\end{aligned} \tag{1.175}$$

The above form requires the knowledge of a four-point function, which in turn leads to an infinite hierarchy of equations, called the Balitsky hierarchy [86]. However, in the large-$N_c$ limit, one has [86]

$$\left\langle \operatorname{tr}\left(U^\dagger(x)U(y)\right)\operatorname{tr}\left(U^\dagger(z)U(y)\right)\right\rangle_{x_g} \approx \left\langle \operatorname{tr}\left(U^\dagger(x)U(y)\right)\right\rangle_{x_g}\left\langle \operatorname{tr}\left(U^\dagger(z)U(y)\right)\right\rangle_{x_g}, \tag{1.176}$$

[6] $U = P\exp\left[-ig\int dx^- A_a^+(x^-, x_\perp)T_a\right]$, where $A^+[\rho]$ is the solution of Eq. (1.169) in the covariant gauge, $-\nabla_\perp^2 A^+ = \rho$ and $A$ represents the last gluon with momentum $k_+ \ll p_+$ of the cascade (when $p_+$ is fast parton).

thus Eq. (1.175) reduces to the BK equation (1.147).

## 1.8 Improved TMD factorization

In the small-$x$ physics there are two commonly used factorization schemes, namely the transverse momentum dependent (TMD) factorization [89] and the high-energy ($k_t$) factorization [64]. Both of these factorizations decompose cross sections into gluon densities and hard kernels, which can be schematically written as

$$\frac{d\sigma}{d\text{P.S.}} = \sum_i G_i(x, k_T^2) H_i(x, k_T^2, Q), \tag{1.177}$$

where on the left-hand side we have differential cross section over the phase-space, P.S., and we denote gluon densities by $G_i$, and the hard kernels by $H_i$.

The TMD factorization is in general not restricted to the small-$x$ region, while the formalism assumes kinematic region of $Q_s^2 \sim k_T \ll P_T$, where the momentum imbalance $k_T$ is small compared to the individual jet momentum $P_T$. In contrast, the high-energy factorization is valid in the small-$x$ region, and the kinematic region of validity is $Q_s^2 \ll k_T \sim P_T$.

As we saw earlier in Eqs. (1.153) and (1.154), which are instances of the high-energy factorization formulae, the relevant gluon density in the high-energy factorization is the dipole gluon density (1.174), whereas in the TMD factorization, several gluon densities appear [81]. Most notably, in the large-$N_c$ limit, TMD factorization involves two gluon densities, namely the dipole and Weizsäcker-Williams gluon densities.

Due to the condition $k_T \ll P_T$, the TMD hard functions ignore the $k_T$-dependence [81], that is, the partonic cross sections are on-shell, and $k_T$-dependence is solely in the TMD PDFs. In the high-energy factorization, in contrast, the impact factor, as we saw earlier in Eqs. (1.153) and (1.154), is dependent on $k_T$, that is the hard function is off-shell and both the hard function and the PDFs are $k_T$-dependent.

Therefore, one sees these two schemes as complementary, and the Improved Transverse-Momentum-Dependent (ITMD) [81,90] can be viewed as an unification of the high-energy factorization and TMD factorization. The key point which differentiate ITMD from the TMD is the off-shell hard functions which carry the $k_T$-dependence. This, in other words, removes the constraint of $Q_s \sim k_T \ll P_T$, and thus allowing for description of the full range of momenta $Q_s \lesssim k_T < P_T$. As proven in Ref. [91], ITMD framework resums all kinematic twists of $(Q_s/k_T)^n$ and $(k_T/P_T)^n$, and equivalence of CGC and and ITMD can be found when the genuine twist (multi-parton interactions) are ignored.

## 1.9 Summary of the chapter

In this chapter, we have addressed fundamental concepts which form a basis of description of particle interactions at high energies. In the low-scale domain, QCD is non-perturbative, and hence the expansion in the coupling constant is inapplicable.

The factorization theorem allows one to isolate the long-distance (low-energy) phenomena, from the short-distance (high-energy) phenomena for which the perturbative approach is valid.

In processes such as DIS and DY, the objects which describe the low-scale physics are called the parton distribution functions (PDFs). In the high energy limit, the fully inclusive cross sections are described by the collinear PDFs, which depend on the Bjorken scaling variable $x$. In the collinear factorization, the Bjorken scaling is logarithmically violated, which in turn makes it necessary to resum the large logarithms $\ln \mu^2$, which renders the PDFs factorization-scale-dependent.

In the small-$x$ limit, another type of large logarithms, $\ln(1/x)$, appear, which must also be resummed. This is achieved by the BFKL equation which predicts a sharp rise of the gluon density, and hence the rise of cross sections, with decreasing $x$, which eventually violates the Froissart bound.The problem is solved by the BK equation, which incorporates the phenomenon of saturation by introducing a non-linear correction on top of the BFKL equation.

Descriptions of less inclusive observables also require another type of PDFs called the transverse-mementum-dependent (TMD) PDFs. The universality is violated in this case and one requires multiple species of TMDs in the description. In the region of moderate $x$, a type of TMDs called the beam functions can be computed in perturbation theory, in which the non-perturbative effects are contained inside the standard collinear PDFs. Operator definitions of the beam functions can be provided by the soft-collinear effective theory (SCET), in which the fields are decomposed into soft, collinear and anti-collinear parts, which do not interact with each other at leading order in the expansion parameter $\lambda$. The hard degrees of freedom are integrated out and absorbed inside the Wilson coefficients, which are obtained from matching to the full theory, *i.e.* QCD.

In the following chapters, we will discuss how, in practice, the beam functions are obtained, and how the models of gluon densities describing the saturation effects can be improved by incorporating additional physical effects.

# Chapter 2

# Towards the N$^3$LO beam functions

## 2.1 Phasespace integration for real emissions

### 2.1.1 Overview

At leading order, the partonic beam functions are simply given by [38]

$$\mathcal{B}^{(0)}_{i/j}(z, x_T) = \delta_{ij}\delta(1-z). \tag{2.1}$$

Beyond LO, one needs to evaluate Eq. (1.111). Pure-virtual diagrams do not contribute to the beam function, since they involve only scaleless integrals [38], thus, at NLO, only single-real emissions are needed [33, 38]. The NLO beam functions were computed for the DY process ($q \to qg$ and $g \to q\bar{q}$ channels) in Ref. [33]. The NNLO beam functions were computed in Refs. [38, 92], for which the real-virtual (RV) and double-real (RR) contributions were needed. Recently, in Refs. [93–98], N$^3$LO beam functions of quarks and gluons were obtained.

While the beam functions can be obtained using the methods of loop calculations [38, 92–98], which yields analytic result in terms of multiple polylogarithms, the complexity of the problem makes numerical approach an appealing option. In this chapter, a scheme for calculation of the beam functions based on numerical integration at N$^3$LO is discussed.

In this study we consider the channels depicted in Fig. 2.1, and, in particular, the contribution proportional to the colour factor $n_f C_F^2 T_F$. In order to evaluate the beam functions, one first needs to calculate collinear splitting amplitudes. While the splitting amplitude was computed independently for this project [99], later it was also computed in Ref. [100]. Since for our calculation, we need a space-like splitting amplitude, the above result of Ref. [100] has to be crossed, as we shall discuss in Sec. 2.1.2.

The diagram in Fig. 2.2 is an example of a cut diagram with triple-real emissions. As discussed later in Sec. 2.3, one additionally needs diagrams which involve virtual emissions which correspond to cutting relevant diagrams at different places in analogy to the cases depicted in Fig. 1.2. The main interest of this study is the method of phase space integrals for real emissions, and this involves extraction of the divergences which arise when emitted particles become soft or collinear to one another. Additional

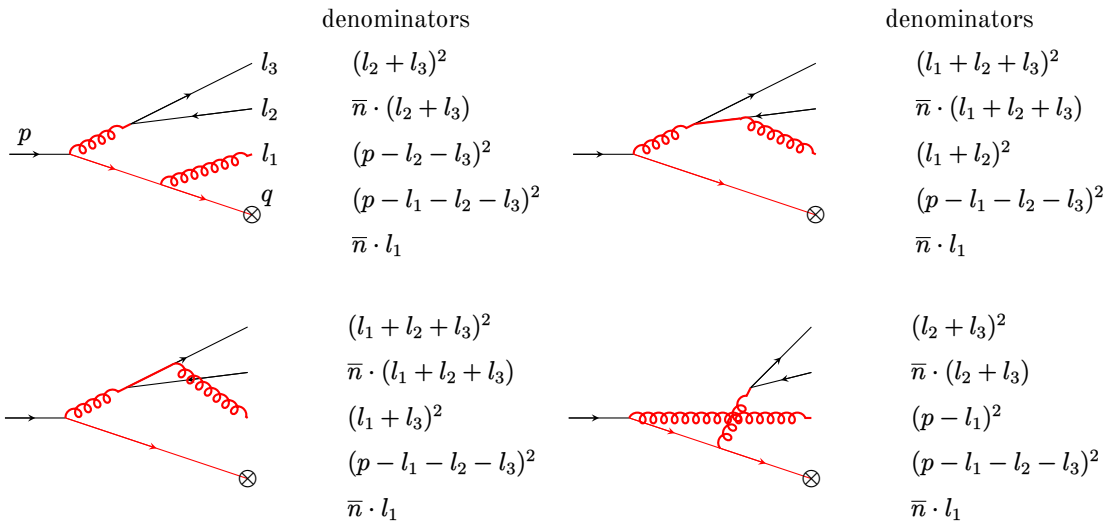


Figure 2.1: Kinematical variables and Feynman diagrams of N$^3$LO splittings contributing to the term proportional to $n_f T_F C_F^2$, in the $q \to qq'\bar{q}'g$ channel. Divergent propagators are highlighted in red and the corresponding denominators are listed.

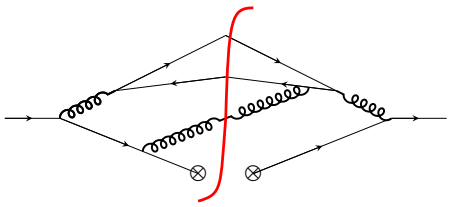

Figure 2.2: An example of cut diagrams at N$^3$LO splitting in the $q \to qq'\bar{q}'g$ channel.

divergences, called the rapidity divergences, appear as a consequence of expansion by regions. The divergences, in the case of the former, can be regularized by dimensional regularization, that is, by integrating in $d = 4-2\epsilon$ dimensions. In the case of the latter, divergences are regularized with help of additional analytic regulator, $\alpha$, as we shall discuss in Sec. 2.1.3 . With these regulators, the integrals can be Laurent-expanded around $\epsilon = 0$, $\alpha = 0$, *cf.* Eq. (1.133). However, as we shell see shortly, in practice, the integrand is not guaranteed to behave well in the $x_i \to 0$ limit.

### 2.1.2 Matrix elements

The starting point of our calculation is obtaining the matrix element defined in analogy to Eq. (1.111), in which the proton $N(p)$ is replaced by a quark $q(p)$. As previously mentioned, in the SCET framework, the Lagrangians of the respective regions after the decoupling transformation, Eq. (1.94), are simply the copies of the QCD Lagrangian. Hence we can effectively use the standard Feynman rules of QCD (1.10)–(1.17).

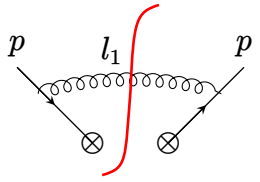


Figure 2.3: A cut diagram of $q \to qg$ contribution for the beam function at NLO.

At NLO, the matrix element for the contribution de-

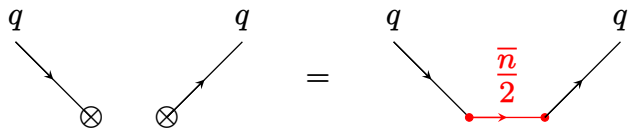


Figure 2.4: Schematic view of the replacement of the propagator (2.4).

picted in Fig. 2.3 is given in the covariant gauge by [27]

$$|M_{q\to qg}|^2 = -\frac{g_s^2}{2} C_F \,\mathrm{tr}\left[(\not{p} - \not{l}_1)\gamma^\mu \not{p} \gamma_\mu (\not{p} - \not{l}_1)\frac{\not{\bar{n}}}{2}\right] \frac{1}{(p-l_1)^4}, \tag{2.2}$$

where $q$ is the incoming quark and $l_1$ is the emitted gluon momentum. While the exact role of this matrix element will become clear in Eq. (2.19), for the moment, it should be understood as an object closely related to the hadronic matrix elements of Eq. (1.111).

One immediately notices that the difference between Eq. (2.2) and the regular squared splitting matrix element is the presence of $\frac{\not{\bar{n}}}{2}$. As it was previously mentioned, squared amplitudes can be conveniently depicted by the cut diagrams, Fig. 2.1. A regular cut diagram in QCD can be obtained with the Feynman rules by placing the lines (propagators), which are cut, on mass-shell. This effectively means applying the replacement

$$\frac{i}{l_i^2} \to 2\pi\delta^+\left(l_i^2\right) \equiv 2\pi\delta\left(l_i^2\right)\theta\left(E_i\right), \tag{2.3}$$

for the propagators which are cut. This is known as the *unitarity cuts* [7]

The replacement (2.3) should be used for the lines which are cut in Fig. 2.2, however the lines terminating at the convolution sign $\otimes$ require special treatment. The correct matrix element at the level of the Feynman diagrams can be obtained by attaching a spinor $u(\bar{n}/2)$ (or possible other spinors depending on the diagram) to the either side of the legs. That is to say, instead of the replacement (2.3), we replace the propagator as

$$\frac{\not{q}}{q^2} \to \frac{\not{q}}{q^2}\bar{u}\left(\frac{\bar{n}}{2}\right) u\left(\frac{\bar{n}}{2}\right)\frac{\not{q}}{q^2} = \frac{\not{q}}{q^2}\frac{\not{\bar{n}}}{2}\frac{\not{q}}{q^2}, \tag{2.4}$$

for the line going into the hard process, (represented by $\otimes$) as depicted in Fig. 2.4.

An equivalent method is to use QCD splitting amplitudes. Let us consider a QCD scattering amplitude with $n$ on-shell external legs carrying the momenta $p_i$

$$|M_n(p_1, p_2, \ldots, p_n)\rangle\,. \tag{2.5}$$

The collinear factorization [101, 102] tells us that in the collinear limit, for example $p_1 \parallel p_2$, the amplitude factorizes to

$$|M_n(p_1, p_2, \ldots, p_n)\rangle \simeq \mathbf{Sp}(p_1, p_2, \tilde{P})\left|M_{n-1}(\tilde{P}, p_3 \ldots, p_n)\right\rangle, \tag{2.6}$$

where $\left|M_n(\tilde{P}, p_3 \ldots, p_n)\right\rangle$ is a reduced amplitude, with $n-1$ external legs in this case. The splitting matrix $\mathbf{Sp}(p_1, p_2, \tilde{P})$ describes the collinear splitting, which we are

interested in. More specifically, we need a triple-collinear splitting function $P$ which is the colour-averaged splitting matrix squared

$$P(p_1,p_2,p_3,p_4,\tilde{P}) = \overline{\left|\mathbf{Sp}(p_1,p_2,p_3,p_4,\tilde{P})\right|^2}. \tag{2.7}$$

Following the prescription of Refs. [102, 103], one can obtain **Sp** by computing a matrix element for the process

$$q\left(\frac{n}{2}p_-\right) \to q\left(\tilde{P}\right) + g(l_1) + \overline{q}'(l_2) + q'(l_3), \tag{2.8}$$

with standard Feynman rules, where the momenta are as labelled in the top-left diagram of Fig. 2.1, except for $q$, which is replaced by

$$\tilde{P} = (p - \sum_{i=1}^{3} l_i) - \frac{(p-\sum_{i=1}^3 l_i)^2}{2zp_-}\overline{n} = q - \frac{q^2}{2zp_-}\overline{n}. \tag{2.9}$$

This can be thought of as a modified unitarity cut, (2.3):

$$i\frac{\not{q}}{q^2} \to 2\pi \tilde{\not{P}}\delta^+(\tilde{P}^2). \tag{2.10}$$

We have verified that the above two prescriptions (2.4) and (2.10) are the same up to a factor, in the following way. We first decompose the right-hand side of (2.4) into gamma matrices and momenta:

$$\frac{\not{q}}{q^2}\frac{\overline{\not{n}}}{2}\frac{\not{q}}{q^2} = \frac{1}{2q^4}\left[\gamma^\alpha\gamma^\beta\gamma^\gamma\right] q^\alpha \overline{n}^\beta q^\gamma. \tag{2.11}$$

Using the the identity

$$\gamma^\beta\gamma^\gamma\gamma^\delta = g^{\beta\gamma}\gamma^\delta + g^{\gamma\delta}\gamma^\beta - g^{\beta\delta}\gamma^\gamma - i\epsilon^{\sigma\beta\gamma\delta}\gamma^\sigma\gamma^5, \tag{2.12}$$

and noticing that the there is a symmetry under the exchange of $q^\beta \leftrightarrow q^\delta$, for which the term with the Levi-Civita tensor vanish, one can rewrite

$$\begin{aligned}\frac{1}{2q^4}\left[\gamma^\alpha\gamma^\beta\gamma^\gamma\right] q^\beta\overline{n}^\gamma q^\delta =& \frac{1}{2q^4}\left[\gamma^\alpha\right](2q\cdot\overline{n}q - q^2\overline{n})^\alpha \\ =& \frac{q_-}{q^4}(\not{q} - \frac{q^2}{2q\cdot\overline{n}}\overline{\not{n}}) \\ =& \frac{q_-}{q^4}\tilde{\not{P}}.\end{aligned} \tag{2.13}$$

In the end, we get

$$\frac{\not{q}}{q^2}\frac{\overline{\not{n}}}{2}\frac{\not{q}}{q^2} = \frac{q_-}{q^4}\tilde{\not{P}}. \tag{2.14}$$

Then we find that the two prescriptions (2.4) and (2.10), respectively, can be

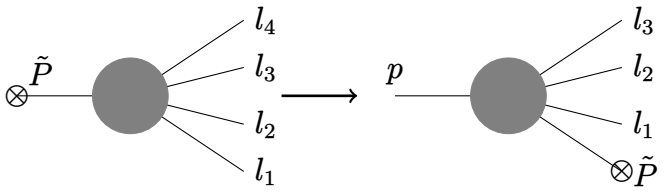


Figure 2.5: Conversion between time-like and space-like splitting functions amounts to exchanging one of the outgoing leg with the incoming leg.

reformulated to produce the same results

$$\frac{\not{q}}{q^2} \to \frac{zp_-}{q^4}(\not{q} - \frac{q^2}{2q\cdot\overline{n}}\not{\overline{n}}) \qquad \text{and} \qquad \frac{\not{q}}{q^2} \to \frac{1}{2q^4}\not{q}\not{\overline{n}}\not{q}, \tag{2.15}$$

where the on-shellness of $\tilde{P}$ is guaranteed by the definition (2.9). In the above, we have used the fact $\overline{n}\cdot q = zp_-$. The factor differentiating the two prescriptions needs to be included if one is to use the QCD splitting functions to compute the beam functions.

While the process (2.8), we considered above corresponds to a space-like splitting, in Refs. [100–102, 102], the splitting functions are time-like. In our calculation, we need a space-like splitting function, for which the appropriate conversion amounts to crossing the incoming momenta and one of the outgoing momenta, depicted in Fig. 2.5. We note that, the incoming momentum on the left-hand side diagram is defined as

$$\tilde{P} = (\sum_{i=1}^{4} l_i) - \frac{(\sum_{i=1}^{4} l_i)^2}{2\overline{n}\cdot(\sum_{i=1}^{4} l_i)}\overline{n}, \tag{2.16}$$

whereas $\tilde{P}$ on the right-hand side diagram is given by Eq. (2.9).

With the method (2.15) described above, the calculation of the matrix elements can be carried out following the standard Dirac-Clifford and colour algebra. Computation of the squared amplitude is a tedious task, and it is most efficiently done with help of computer programs such as FeynArts/FeynCalc [104–108]. The pure-real N$^3$LO splitting amplitude was computed independently for this project [99] and, it was also computed later in Ref. [100].

### 2.1.3 Phase space integration

Consider the definition of the parton-to-parton beam function following Eq. (1.111), where the hadron $N$ is replaced by a parton. An anti-collinear beam function, $\overline{\mathcal{B}}_{i/j}(z, x_T^2)$ is defined also analogously to Eq. (1.111), whereas $\overline{n}$ and $p$ are replaced with $n$ and $\overline{p}$.

Eq. (1.111) can be rearranged as follows:

$$\begin{aligned}\mathcal{B}_{q/q}(z,x_T^2,\mu) &= \frac{1}{2\pi}\int dt\, e^{-izt\bar{n}\cdot p} \\ &\quad \sum_X \langle q(p)|\, e^{i\hat{p}\cdot(t\bar{n}+x_\perp)}\overline{\chi}(0)e^{-i\hat{p}\cdot(t\bar{n}+x_\perp)}\,|X\rangle \frac{\not{\bar{n}}}{2}\langle X|\,\chi(0)\,|q(p)\rangle \\ &= \frac{1}{2\pi}\sum_X \int dt e^{it\bar{n}\cdot((1-z)p-k)}\int d^dk e^{-ik_\perp\cdot x_\perp} \\ &\quad \times \langle q(p)|\,\overline{\chi}(0)\,|X\rangle \frac{\not{\bar{n}}}{2}\langle X|\,\chi(0)\,|q(p)\rangle \\ &= \sum_X \int d^dk e^{-ik_\perp\cdot x_\perp}\delta(\bar{n}\cdot((1-z)p-k)) \\ &\quad \times \langle q(p)|\,\overline{\chi}(0)\,|X\rangle \frac{\not{\bar{n}}}{2}\langle X|\,\chi(0)\,|q(p)\rangle\,,\end{aligned} \tag{2.17}$$

where $\hat{p}$ is a momentum operator which returns $p$ and $k$ respectively of the initial quark and the final emissions. In the second equality, we used the relations

$$p\cdot x_\perp = 0 \qquad \text{and} \qquad k\cdot x_\perp = k_\perp\cdot x_\perp\,. \tag{2.18}$$

Let us now consider the case of triple real emissions

$$\begin{aligned}\mathcal{B}_{q/q}^{(3,3)}(z,x_T) &= \int d^dk\left[\prod_{i=1}^n\int_0^\infty \frac{d^dl_i}{(2\pi)^{d-1}}\delta^+(l_i^2)\right] \\ &\quad \times \delta^d(k-\sum_j^n l_j)\delta(\bar{n}\cdot(k-(1-z)p))e^{-ik_\perp\cdot x_\perp}|M(q\to qq'\bar{q}'g)|^2,\end{aligned} \tag{2.19}$$

where $|M(q\to qq'\bar{q}'g)|^2$ is the matrix element we have discussed in the previous section.

The phase-space integral of Eq. (2.19) can be written explicitly in the light-cone coordinates and $4-2\epsilon$ dimensions:

$$\begin{aligned}&\left[\prod_{i=1}^n \frac{1}{(2\pi)^{3-2\epsilon}}\int_0^\infty dl_{i-}\int_0^\infty d|l_{i\perp}|\int d^{1-2\epsilon}\Omega_{l_i}\ \frac{|l_{i\perp}|^{1-2\epsilon}}{l_{i-}}\delta^+(l_i^2)\right] \\ &\qquad \times \delta(\bar{n}\cdot(\sum_j^n l_j-(1-z)p))|\sum_j^n l_{j\perp}|^2 e^{-|\sum_j^n l_{j\perp}|^2}.\end{aligned} \tag{2.20}$$

One can see here that the $l_-$ component is not regularized by $\epsilon$. Indeed, as previously mentioned, this divergence (rapidity/light-cone divergence) in the region where $l_{i-}\to 0$ requires additional regulator [33, 38, 39]. We employ here the method of Ref. [39], which introduces a factor

$$\left(\frac{\nu}{l_{i+}}\right)^\alpha, \tag{2.21}$$

for each emission $i$. One should, however, keep in mind that the limit $\alpha \to 0$ has to be taken before the limit $\epsilon \to 0$. More importantly, this regulator has to be the same for the collinear and anti-collinear beam functions, thus the two are no longer symmetric under the exchange of $n \leftrightarrow \overline{n}$, $p \leftrightarrow \overline{p}$. The symmetry is only recovered after the re-factorization, Eq. (1.115), where this divergences are cancelled and the $\alpha \to 0$ limit is taken.

On top of introduction of (2.21), in order to simplify the integration, we replace

$$e^{-ik_\perp \cdot x_\perp} \qquad \text{with} \qquad |k_\perp|^2 e^{-|k_\perp|^2}, \tag{2.22}$$

as a consequence, the result differs by a factor

$$\begin{aligned} \frac{\int d^{d-2}k_\perp (k_T^2)^\sigma e^{-ik_\perp \cdot x_\perp}}{\int d^{d-2}k_\perp (k_T^2)^{\sigma+1} e^{-k_T^2}} &= \left(\frac{4}{x_T^2}\right)^{\frac{d-2}{2}+\sigma} \frac{\Gamma\left(\frac{d-2}{2}\right)}{\left(\frac{d-2}{2}+\sigma\right)\Gamma(-\sigma)} \\ &= \left(\frac{x_T^2}{4}\right)^{r\alpha+n\epsilon} \frac{\epsilon\Gamma(1-\epsilon)}{(r\alpha+n\epsilon)\,\Gamma(1-\epsilon+(r\alpha+n\epsilon))}, \end{aligned} \tag{2.23}$$

where in the last line, $r$ stands for the number of real emissions, $n$ is the order in $\alpha_s$, and also the contribution from $\alpha$-regulator, Eq. (2.21), was restored.

In summary, in order to calculate a pure-real correction to a beam function at order $n$, we nee to evaluate the integral

$$\begin{aligned} I^{(r)}_{\mathcal{B}_{q/q}} = \int_0^\infty d^d k \left[\prod_{i=1}^r \int_0^\infty \frac{d^d l_i}{(2\pi)^{d-1}} \delta^+(l_i^2) \left(\frac{\nu}{l_{i+}}\right)^\alpha\right] \\ \times \delta^d(k - \sum_{j=1}^r l_j)\delta(k_- - (1-z))|k_\perp|^2 e^{-|k_\perp|^2} |M(q \to q + X)|^2, \end{aligned} \tag{2.24}$$

where the scale-dependence has been extracted by rescaling

$$l_+ \to l_+/p_-, \qquad\qquad l_- \to l_- p_-. \tag{2.25}$$

Eq. (2.24) is related to the beam function, Eq. (2.19), by

$$\mathcal{B}^{(n)}_{i/j} = p_-^{r\alpha} \nu^{r\alpha} C(x_T^2, n, r, \alpha, \epsilon) I^{(n)}_{\mathcal{B}_{i/j}}, \tag{2.26}$$

$$\overline{\mathcal{B}}^{(n)}_{i/j} = \overline{p}_+^{-r\alpha} \nu^{r\alpha} C(x_T^2, n, r, 0, \epsilon) \overline{I}^{(n)}_{\mathcal{B}_{i/j}}, \tag{2.27}$$

where

$$C(x_T, r, n, \alpha, \epsilon) = \left(\frac{x_T^2}{4}\right)^{r\alpha+n\epsilon} \frac{\epsilon\Gamma(-\epsilon)}{(r\alpha+n\epsilon)\,\Gamma(1-\epsilon+(r\alpha+n\epsilon))}. \tag{2.28}$$

Using the notations of Ref. [38]

$$L_c = \ln\left(\frac{x_T^2 p_- \nu}{4e^{-2\gamma_E}}\right), \qquad L_a = \ln\frac{\nu}{\overline{p}_+}, \qquad L_\perp = \ln\frac{\mu^2 x_T^2}{4e^{-2\gamma_E}}, \tag{2.29}$$

and $\overline{p}_+ = p_- = Q$, one finally gets

$$\mathcal{B}_{i/j}^{(n,r)}(z, x_T^2, Q\nu, \mu^2) = (4\pi)^{-n\epsilon} e^{r\alpha L_c + n\epsilon L_\perp} e^{-(2r\alpha + n\epsilon)\gamma_E} \times \frac{\epsilon\Gamma(-\epsilon)}{(r\alpha + n\epsilon)\Gamma(1 - \epsilon + (r\alpha + n\epsilon))} I_{\mathcal{B}_{i/j}}^{(n,r)}(z), \tag{2.30}$$

$$\overline{\mathcal{B}}_{i/j}^{(n,r)}(z, x_T^2, \frac{Q}{\nu}, \mu^2) = (4\pi)^{-n\epsilon} e^{r\alpha L_a + n\epsilon L_\perp} e^{-n\epsilon\gamma_E} \frac{\Gamma(-\epsilon)}{n\Gamma(1 - (1-n)\epsilon))} \overline{I}_{\mathcal{B}_{i/j}}^{(n,r)}(z), \tag{2.31}$$

where we have generalized the notation for $r$ real emissions at N$^n$LO. Notice that the scales $x_T^2$ and $Q^2$ are absorbed inside the prefactor and the integrals $I_{\mathcal{B}_{i/j}}^{(r,n)}$ and $\overline{I}_{\mathcal{B}_{i/j}}^{(r,n)}$ are only functions of $z$.

The main challenge in the evaluation of integral (2.24) is its complex structure of divergences.

### 2.1.4 Phase space parametrization

Let us now consider a general phase space integrations of real emissions. One can parametrize the momenta of real emissions $l_i = (E_i, \vec{l}_i)$ such that [41]

$$\begin{aligned}
\vec{l}_1 &= \left|\vec{l}_1\right| (0,\ \ldots, 0, 0,\ \sin\theta_1,\ \cos\theta_1), \\
\vec{l}_2 &= \left|\vec{l}_2\right| (0,\ \ldots, 0,\ \sin\phi_2\ \sin\theta_2,\ \cos\phi_2 \sin\theta_2,\ \cos\theta_2), \\
\vec{l}_3 &= \left|\vec{l}_2\right| (0,\ \ldots, \\
&\qquad \sin\chi_3\ \sin\phi_3\ \sin\theta_3, \cos\chi_3\ \sin\phi_3\ \sin\theta_3,\ \cos\phi_3\ \sin\theta_3,\ \cos\theta_3), \\
&\ \ \vdots
\end{aligned} \tag{2.32}$$

where the mass-shell condition $l_i^2 = 0$ fixes $\left|\vec{l}_i\right| = E_i$. Then, the relevant scalar products become

$$\begin{aligned}
l_1 \cdot n &= E_1(1 - \cos\theta_1), & l_1 \cdot \overline{n} &= E_1(1 + \cos\theta_1), \\
l_2 \cdot n &= E_2(1 - \cos\theta_2), & l_2 \cdot \overline{n} &= E_2(1 + \cos\theta_2), \\
l_3 \cdot n &= E_3(1 - \cos\theta_3), & l_3 \cdot \overline{n} &= E_3(1 + \cos\theta_3), \\
l_1 \cdot l_2 &= E_1 E_2 (1 - \cos\theta_1 \cos\theta_2 - \cos\phi_2 \sin\theta_1 \sin\theta_2), \\
l_1 \cdot l_3 &= E_1 E_2 (1 - \cos\theta_1 \cos\theta_3 - \cos\phi_3 \sin\theta_1 \sin\theta_3), \\
l_2 \cdot l_3 &= E_2 E_3 \,(1 - \cos\chi_3 \sin\phi_2 \sin\phi_3 \sin\theta_2 \sin\theta_3 \\
&\qquad - \cos\phi_2 \cos\phi_3 \sin\theta_2 \sin\theta_3 - \cos\theta_2 \cos\theta_3)\,, \\
&\ \ \vdots
\end{aligned} \tag{2.33}$$

Thus, the momenta are parametrized effectively as $r+2$ dimensional vectors for $r$ real emissions.

Since, in this scheme, the external momenta are integrated in $4 - 2\epsilon$ dimensions,

for the case $r \leq 4$, one can trivially integrate part of the hyper-surface using [41]

$$\int_{S^{d-1}} d\Omega = \frac{2\pi^{d/2}}{\Gamma(d/2)}. \tag{2.34}$$

In the N$^3$LO case, at most, one momentum has five non-trivial dimensions. We therefore employ the formula [41]

$$\begin{aligned}\int_{S^{-2\epsilon}} d\Omega = \frac{(4\pi)^{-\epsilon}\Gamma(1-\epsilon)}{\Gamma(1-2\epsilon)} \int_{-1}^{1} d(\cos\rho) \\ \left(\delta(1-\cos\rho) + \delta(1+\rho) - 2\epsilon \frac{4^{\epsilon}\Gamma(1-2\epsilon)}{\Gamma^2(1-\epsilon)} \left[(1-\cos^2\rho)^{-1-\epsilon}\right]_+\right),\end{aligned} \tag{2.35}$$

for one of the dimensions of the third momentum.

In the parametrization (2.33), the soft, $n$-collinear and $\overline{n}$-collinear (anti-collinear) divergences of $l_1$, for example, correspond to the limits $E_1 \to 0$, $\theta_1 \to 0$ and $\theta_1 \to \pi$, respectively. Clearly, the $l_i$, $l_j$-collinear divergences of the products $l_i \cdot l_j$ are not a simple endpoint singularities in this parametrization, even for the simplest $l_1 \cdot l_2$, which diverges only when $\phi_2 = 0$ and $\theta_1 = \theta_2$ simultaneously. Now, one can identify that this is a overlapping manifold singularity, *cf.* Eqs. (1.125) and (1.126). On top of this, one encounters the denominators of the type $(l_1 + l_2) \cdot \overline{n}$ and $2l_1 \cdot l_2 - n \cdot (l_1 + l_2)$. The former arises from the internal gluon propagator in the light-cone gauge with momentum $l_1 + l_2$ and the latter from the propagator denominator $(p - (l_1 + l_2))^2$, *cf.* Fig. 2.1. Naturally, there is some freedom in the choice of parametrization. For example, one can parametrize the momenta such that $l_1 \cdot l_2 = E_1 E_2 (1 - \cos\theta_{12})$ at the cost of $l_1 \cdot n$ and $l_1 \cdot \overline{n}$ becoming complicated.

As discussed earlier (*cf.* Sec. 2.1.2), one encounters the light-cone divergences in the present integration. For such case, one may choose to parametrize momenta with light-cone coordinates instead of (2.32), where the transverse components $l_{i\perp}$ are defined in the analogous way to the above case of Eq. (2.32), only that they are $d-2$ dimensional:

$$l_i = (\frac{l_{i-} + l_{i+}}{2}, 0, \cdots, l_{iT}\sin(\theta), l_{iT}\cos(\theta), \frac{l_{i-} - l_{i+}}{2}). \tag{2.36}$$

This parametrization is more intuitive recalling that the rapidity divergences correspond to the limits

$$l_{i-} \to 0 \qquad \text{while} \qquad l_{iT} \equiv |l_{i\perp}| \neq 0, \tag{2.37}$$

that is the limits where the rapidity $\ln\left(\frac{l_{i-}}{l_{iT}}\right) \to -\infty$.

With the help of selector functions, one can select a parametrization for each emission, which is optimal for a given subset of divergences. For instance, parametrization (2.32), or equivalently (2.33), is suitable when the unsuppressed divergences occur at $n$-collinear limits, while if we are to handle the $l_2$, $l_3$-collinear divergence, it is clearly not a good choice.

Once the momenta are suitably parametrized, it is convenient to put the expres-

sions in a unit hypercube parametrized in variables $x_i \in [0,1]$. In order to do that, for the angles and the energies, one can use replacements of the form

$$\cos(\theta_i) \to 1 - 2x_j \qquad \text{and} \qquad E_k \to \frac{x_l}{1-x_l}. \tag{2.38}$$

The light-cone variables can be also transformed in an analogous way:

$$l_{i-} \to x_j \qquad \text{and} \qquad l_{kT} \to \frac{x_l}{1-x_l}, \tag{2.39}$$

where the minus components are restricted by the delta function in Eq. (2.24) to be

$$\sum_i l_{i-} = (1-z), \tag{2.40}$$

after the rescalings (2.25). In the parametrization (2.33), one encounters also

$$l_1 \cdot l_2 = E_1 E_2 (1 \pm \cos\phi_2 \sin\theta_1 \sin\theta_2 - \cos\theta_1 \cos\theta_2). \tag{2.41}$$

For such a case, one can use the change of variables [41]

$$\cos(\phi_2) \to \frac{(1-2\zeta)(1-\cos(\theta_1)\cos(\theta_2)) \pm \sin(\theta_1)\sin(\theta_2)}{1-\cos(\theta_1)\cos(\theta_2) \pm (1-2\zeta)\sin(\theta_1)\sin(\theta_2)}, \tag{2.42}$$

which, together with (2.38), yields

$$l_1 \cdot l_2 \to \frac{2(x_1-x_2)^2}{x_2 + x_1(1-2x_2) + 2\sqrt{(1-x_1)x_1(1-x_2)x_2}(1-2\zeta)}, \tag{2.43}$$

where the third variable, $\zeta$, is no longer related to any divergence. With this parametrization, the triple collinear limit is clear at $x_1 = x_2$, and can be transformed to an endpoint singularity as demonstrated earlier in Sec. 1.4.

### 2.1.5 Selector functions

As we saw in Sec. 1.4, selector functions can be very useful in suppressing subsets of divergences while keeping the rest of active divergences. We shall employ the term *primary sector* for the sectors defined by the selector functions. For each primary sector, with its corresponding subset of divergences, we choose the optimal parametrization and apply sector decomposition procedure. In the example of Sec. 1.4, we used the selector functions $\{x_2, 1-x_2\}$ *cf.* Eq. (1.130). In this section, a general treatment of selector functions, which is required by the N$^3$LO calculation, is discussed.

Let $C_i$ be a set of *maximally divergent* limits with the corresponding selector function $S_i$:

$$S_i\Big|_{C_j} = \begin{cases} 1, & \text{if } i = j \\ 0, & \text{if } i \neq j \end{cases}. \tag{2.44}$$

A maximally divergent set is a full set of limits which can occur simultaneously. In two

dimensions, for example, one may have a set $\{x_1 \to 0, x_2 \to 0\}$, as one of such sets, but not $\{x_1 \to 0, x_2 \to 0, x_2 \to 1\}$, since the last two cannot happen simultaneously. In this example, $\{x_1 \to 0\}$ and $\{x_2 \to 0\}$ are not maximally divergent set since they are subsets of a larger sets (*i.e.* they are divergent but not maximal).

One should note that there are cases of limits which are not allowed to happen simultaneously by the matrix element. In other words, they correspond to unphysical points in the phase space. For example, the case where the minus components $l_{i-}$ of all real emissions vanishing is suppressed by the delta function $\delta(\sum l_{i-} - (1-z)p_-)$, *cf.* Eqs. (2.19) and (2.24). In other words, even though a set is a superset of some possible limits without double counting the variables, the limit may not be divergent (*i.e.* they are maximal but not divergent).

A complete set of selector functions must satisfy

$$\sum_i S_i = 1. \tag{2.45}$$

The functions which fulfil the above requirements, Eqs. (2.44) and (2.45), can thus be obtained by the following definition [41, 109]:

$$S_i = \frac{1}{d_i \left( \ldots + \frac{1}{d_{i-1}} + \frac{1}{d_i} + \frac{1}{d_{i+1}} + \ldots \right)}, \tag{2.46}$$

where

$$d_i\Big|_c \begin{cases} \neq 0, & \text{if } c \notin C_i \\ = 0, & \text{if } c \in C_i \end{cases}. \tag{2.47}$$

In the above, $d_i|_c$ means taking limit $c$ of $d_i$.

A simple way to construct $d_i$ would be to use the products

$$d_i = \prod_j v_j, \tag{2.48}$$

where $v_j$ are variables (or functions of variables) which vanish in the limit $c_j \in C_i$.

### 2.1.6 Selector functions with light-cone singularities

For the case without light-cone divergences, it suffices to use the relative angles and the energies of emitted particles such that [41, 45, 109]

$$v_j = \begin{cases} 1 - \cos\theta_{\alpha\beta} & \text{collinear} \\ 1 + \cos\theta_{\alpha\beta} & \text{anti-collinear} \\ E_\alpha & \text{soft} \end{cases}. \tag{2.49}$$

Therefore, a sector for soft and collinear limit of $l_1$, for example, would be

$$d_{l_1,\text{soft, coll.}} = E_1(1 - \cos(\theta_1)). \tag{2.50}$$

The presence of rapidity divergences complicates the treatment already at NNLO. In this section, we will propose selector functions which fully address requirements posed by the calculation of the N$^3$LO beam functions. The main idea is unchanged and Eqs. (2.46)-(2.48) are used to construct the selector functions. What is different from those in Refs. [41, 45] is the presence of transverse components.

In order to illustrate this point, let us consider the NNLO case with real emissions $l_1$, $l_2$. Let us first take the $\overline{n}$-collinear limit, where the relative angle of $\overline{n}$ and $l_1$ vanishes. In addition, one may take a limit where $l_1$ becomes soft. This is now a maximally divergent limit, as no other divergent limits are left. However, instead of the soft limit of $l_1$, one may also take the $n$-collinear limit of $l_2$, provided that $E_1$ is large enough so that $l_{1T} \neq 0$, *cf.* Eq. (2.37). These two limits can easily be separated by a choice of the transverse momenta, where in the former, $l_{2T} \neq 0$ and the latter $l_{1T} \neq 0$. This demonstrates that, in order to treat the light-cone divergences, it is necessary to incorporate the transverse components $l_{iT}$ in addition to the angle and energies.

In order to construct a full set of selector functions, one can start with determination of sets of vanishing variables, *cf.* Eq. (2.49), where these sets now contain information on the transverse components. Additionally, the possibility of limits $E_i^{-1} \to 0$ needs to be taken in account. For simplicity, the sets can be grouped by selections of transverse components, and within the group, we can safely make a set of selector functions with angles and energies. Therefore, for three-particle emissions, we have

$$\{S_i\} = [S_{T(1,2)}\{S_{(j;1,2)}\}, \quad S_{T(2,3)}\{S_{(j;2,3)}\}, \quad S_{T(1,3)}\{S_{(j;1,3)}\}], \tag{2.51}$$

where $\{S_i\}$ denotes a list of selector functions $[S_1,\ S_2, ...]$, which satisfy

$$\begin{gathered} \sum_i S_{(i;j,k)} = 1, \qquad\qquad \sum_{j<k} S_{T(j,k)} = 1, \\ \sum_i S_i = \sum_i \sum_{j\neq k} S_{T(j,k)} S_{(i;j,k)} = 1. \end{gathered} \tag{2.52}$$

For the triple-real-emission case, transverse selector functions are given by

$$S_T = \left[ \frac{l_{3T}}{l_{1T}+l_{2T}+l_{3T}}, \qquad \frac{l_{1T}}{l_{1T}+l_{2T}+l_{3T}}, \qquad \frac{l_{2T}}{l_{1T}+l_{2T}+l_{3T}} \right]. \tag{2.53}$$

In practice, different sectors in the transverse momenta are related to each other by permutations of the momenta, thus in the current case it suffices to generate $S_{T(1,2)}\{S_{(j;1,2)}\}$ in Eq. (2.51) and take permutations $S_{T(2,3)}\{S_{(j;2,3)}\}$ and $S_{T(1,3)}\{S_{(j;1,3)}\}$ to produce the full set.

In this method, one initially obtains 66 primary sectors for the N$^3$LO case. It turns out that it is more convenient to combine some sectors, if simple parametrization for the divergences are possible simultaneously. This results in 39 primary sectors. Tab. 2.1, shows the sets of vanishing variables for $S_{(j;1,2)}$, where $\hat{l}_i$ denotes a rescaled momentum $l_i/E_i$.

The angles (scalar products) and energies, or the corresponding light-cone variables, listed in the same block of Tab. 2.1 (*e.g.*, rows labelled dbl. $\overline{n}$-coll.) can be

| Name | Relative angles | | | | Energies | |
|---|---|---|---|---|---|---|
| tpl. coll. | $\hat{l}_1\cdot\hat{l}_2$ | $\hat{l}_1\cdot\hat{l}_3$ | $\hat{l}_2\cdot\hat{l}_3$ | | $E_1$ | $E_2$ |
| dbl. $n$-coll. | $\hat{l}_1\cdot\hat{l}_2$ | $\hat{l}_1\cdot n$ | $\hat{l}_2\cdot n$ | | $E_1$ | $E_2$ |
| dbl. $\overline{n}$-coll. | $\hat{l}_1\cdot\hat{l}_2$ | $\hat{l}_1\cdot\overline{n}$ | $\hat{l}_2\cdot\overline{n}$ | | $E_1$ | $E_2$ |
| | $\hat{l}_1\cdot\hat{l}_2$ | $\hat{l}_1\cdot\overline{n}$ | $\hat{l}_2\cdot\overline{n}$ | | $E_2^{-1}$ | $E_1$ |
| | $\hat{l}_1\cdot\hat{l}_2$ | $\hat{l}_1\cdot\overline{n}$ | $\hat{l}_2\cdot\overline{n}$ | | $E_1^{-1}$ | $E_2$ |
| | $\hat{l}_1\cdot\hat{l}_2$ | $\hat{l}_1\cdot\overline{n}$ | $\hat{l}_2\cdot\overline{n}$ | | $E_1^{-1}$ | $E_2^{-1}$ |
| coll. & $n$-coll. | | $\hat{l}_1\cdot\hat{l}_3$ | $\hat{l}_2\cdot n$ | | $E_1$ | $E_2$ |
| coll. & $\overline{n}$-coll. | | $\hat{l}_1\cdot\hat{l}_3$ | $\hat{l}_2\cdot\overline{n}$ | | $E_1$ | $E_2$ |
| | | $\hat{l}_1\cdot\hat{l}_3$ | $\hat{l}_2\cdot\overline{n}$ | | $E_2^{-1}$ | $E_1$ |
| coll. & $n$-coll. | | $\hat{l}_1\cdot n$ | $\hat{l}_2\cdot\hat{l}_3$ | | $E_1$ | $E_2$ |
| $n$-coll. & $\overline{n}$-coll. | | $\hat{l}_1\cdot n$ | $\hat{l}_2\cdot\overline{n}$ | | $E_1$ | $E_2$ |
| | | $\hat{l}_1\cdot n$ | $\hat{l}_2\cdot\overline{n}$ | | $E_2^{-1}$ | $E_1$ |
| coll. & $\overline{n}$-coll. | | $\hat{l}_1\cdot\overline{n}$ | $\hat{l}_2\cdot\hat{l}_3$ | | $E_1$ | $E_2$ |
| | | $\hat{l}_1\cdot\overline{n}$ | $\hat{l}_2\cdot\hat{l}_3$ | | $E_1^{-1}$ | $E_2$ |
| $n$-coll. & $\overline{n}$-coll. | | $\hat{l}_1\cdot\overline{n}$ | $\hat{l}_2\cdot n$ | | $E_1$ | $E_2$ |
| | | $\hat{l}_1\cdot\overline{n}$ | $\hat{l}_2\cdot n$ | | $E_1^{-1}$ | $E_2$ |
| dbl. $n$-coll. & $\overline{n}$-coll. | $\hat{l}_1\cdot\hat{l}_2$ | $\hat{l}_1\cdot n$ | $\hat{l}_2\cdot n$ | $\hat{l}_3\cdot\overline{n}$ | $E_3^{-1}$ | $E_1$ |
| $n$-coll. & dbl. $\overline{n}$-coll. | $\hat{l}_1\cdot\hat{l}_3$ | $\hat{l}_1\cdot\overline{n}$ | $\hat{l}_2\cdot n$ | $\hat{l}_3\cdot\overline{n}$ | $E_3^{-1}$ | $E_1$ |
| | $\hat{l}_1\cdot\hat{l}_3$ | $\hat{l}_1\cdot\overline{n}$ | $\hat{l}_2\cdot n$ | $\hat{l}_3\cdot\overline{n}$ | $E_1^{-1}$ | $E_3^{-1}$ |
| dbl. $n$-coll. & $\overline{n}$-coll. | $\hat{l}_1\cdot\hat{l}_2$ | $\hat{l}_1\cdot n$ | $\hat{l}_2\cdot n$ | $\hat{l}_3\cdot\overline{n}$ | $E_3^{-1}$ | $E_2$ |
| $n$-coll. & dbl. $\overline{n}$-coll. | $\hat{l}_1\cdot n$ | $\hat{l}_2\cdot\hat{l}_3$ | $\hat{l}_2\cdot\overline{n}$ | $\hat{l}_3\cdot\overline{n}$ | $E_3^{-1}$ | $E_2$ |
| | $\hat{l}_1\cdot n$ | $\hat{l}_2\cdot\hat{l}_3$ | $\hat{l}_2\cdot\overline{n}$ | $\hat{l}_3\cdot\overline{n}$ | $E_2^{-1}$ | $E_3^{-1}$ |

Table 2.1: Examples of sets (2.49) which can be used to construct selector functions $S_{(j;1,2)}$, (*i.e.*, for the sector $l_{3T}\neq 0$). $\hat{l}_i$ denotes rescaled vector $\hat{l}_i\equiv l_i/E_i$. The rows which are not separated by lines are combined into one sector by simply taking the sum of the corresponding selector functions. (tpl.= triple, dbl.= double)

simultaneously parametrized in simple forms described in Sec. 2.1.4.

The full expression of the N$^3$LO selector functions is too large to be presented here, but it is available at

`https://github.com/Tomoki-Goda/Supplementary-materials.git`,

Nevertheless in order to get some insight in the our selector functions, let us take the limit $E_3\to 0$, $\hat{l}_3\cdot n\to 0$, which recovers the NNLO selector functions, which are

compact enough to be presented:

$$S = \left[ \begin{array}{cccc} \dfrac{E_2^2\,\hat{l}_{2+}\,\hat{l}_{2-}}{D_1}\ \dfrac{\hat{l}_{1+}^2\,\hat{l}_{1-}\,\hat{l}_{2-}}{D_2}, & \dfrac{E_2^2\,\hat{l}_{2+}\,\hat{l}_{2-}}{D_1}\ \dfrac{\hat{l}_1\cdot\hat{l}_2\,\hat{l}_{1-}\,\hat{l}_{2-}}{D_2}, \\ \dfrac{E_2^2\,\hat{l}_{2+}\,\hat{l}_{2-}}{D_1}\ \dfrac{(1+E_1^2)\ \hat{l}_1\cdot\hat{l}_2\,\hat{l}_{1+}^2\,\hat{l}_{2-}}{D_2}, & \dfrac{E_2^2\,\hat{l}_{2+}\,\hat{l}_{2-}}{D_1}\ \dfrac{E_1E_2\,\hat{l}_1\cdot\hat{l}_2\,\hat{l}_{1-}}{D_2}, \\ \dfrac{E_1^2\,\hat{l}_{1+}\,\hat{l}_{1-}}{D_1}\ \dfrac{E_1E_2\,\hat{l}_1\cdot\hat{l}_2\,\hat{l}_{2-}}{D_3}, & \dfrac{E_1^2\,\hat{l}_{1+}\,\hat{l}_{1-}}{D_1}\ \dfrac{\hat{l}_{1-}\,\hat{l}_{2+}^2\,\hat{l}_{2-}}{D_3}, \\ \dfrac{E_1^2\,\hat{l}_{1+}\,\hat{l}_{1-}}{D_1}\ \dfrac{(1+E_2^2)\ \hat{l}_1\cdot\hat{l}_2\,\hat{l}_{1-}\,\hat{l}_{2+}^2}{D_3}, & \dfrac{E_1^2\,\hat{l}_{1+}\,\hat{l}_{1-}}{D_1}\ \dfrac{\hat{l}_1\cdot\hat{l}_2\,\hat{l}_{1-}\,\hat{l}_{2-}}{D_3} \end{array} \right] \tag{2.54}$$

where

$$\begin{aligned} D_1 &= \left(E_1^2\,\hat{l}_{1+}\,\hat{l}_{1-} + E_2^2\,\hat{l}_{2+}\,\hat{l}_{2-}\right), \\ D_2 &= \left(\hat{l}_{1+}^2\,\hat{l}_{1-}\,\hat{l}_{2-} + \hat{l}_1\cdot\hat{l}_2\,\left(\left(1+E_1^2\right)\,\hat{l}_{1+}^2\,\hat{l}_{2-} + \hat{l}_{1-}\,\left(E_1E_2 + \hat{l}_{2-}\right)\right)\right), \\ D_3 &= \left(\hat{l}_{1-}\,\hat{l}_{2+}^2\,\hat{l}_{2-} + \hat{l}_1\cdot\hat{l}_2\,\left(E_1E_2\,\hat{l}_{2-} + \hat{l}_{1-}\,\left(\left(1+E_2^2\right)\,\hat{l}_{2+}^2 + \hat{l}_{2-}\right)\right)\right). \end{aligned} \tag{2.55}$$

The first factor in each selector of Eq. (2.54) selects the transverse components, and the second factors select the angles and energies.

Further taking the $n$-collinear limit of $l_1$, we get

$$\frac{\hat{l}_{2-}}{\left(E_1E_2 + \hat{l}_{2-}\right)} \qquad \text{and} \qquad \frac{E_1E_2}{\left(E_1E_2 + \hat{l}_{2-}\right)} \tag{2.56}$$

which are the only non-vanishing selectors. The remaining valid limits are the soft limit of $l_1$, and the rapidity limit of $l_2$ ($E_2 \to \infty$, $\hat{l}_2 \to 0$). These limits leave, respectively, only the first and the second selector function in (2.56) finite, hence the selection is complete.

Instead, one can take another interesting limit where $\hat{l}_1\cdot\overline{n} \to 0$, while keeping $l_{T1} \sim 1$. In this case, the second (angles & energies) part of the selector functions (2.54) collapse to 0 or 1, leaving the transverse selector functions from each sector:

$$\frac{l_{T1}}{l_{T1}+l_{T2}} \qquad \text{and} \qquad \frac{l_{T2}}{l_{T1}+l_{T2}}. \tag{2.57}$$

In this case, when the energy of $l_1$ is sufficiently high, $l_2$ may contribute to $n$-collinear divergence.

## 2.2 Sector Decomposition

While different in complexity, the sector decomposition demonstrated earlier with a toy model, Eq. (1.124), remains valid. As we shall see in this section, at N$^3$LO, there are four variables (let them be called $x_1, x_2, x_3, x_4$), which produce poles at the same time in each sector, and the expression is regular in the remaining 5 variables, *cf.* Sec. 2.1.4.

In Fig. 2.1, lists of potentially divergent denominators and corresponding lines in Feynman diagrams were shown. In general, at N$^3$LO, we have the following denominators:

$$(l_1+l_2)^2, \qquad (l_2+l_3)^2, \qquad (l_1+l_3)^2, \tag{2.58}$$

$$(l_1+l_2+l_3)^2, \tag{2.59}$$

$$(p-l_1-l_2)^2, \qquad (p-l_2-l_3)^2, \qquad (p-l_1-l_3)^2, \tag{2.60}$$

$$(p-l_1-l_2-l_3)^2, \tag{2.61}$$

and

$$l_1\cdot\overline{n}, \qquad l_2\cdot\overline{n}, \qquad l_3\cdot\overline{n}, \tag{2.62}$$

$$(l_1+l_2)\cdot\overline{n}, \qquad (l_2+l_3)\cdot\overline{n}, \qquad (l_1+l_3)\cdot\overline{n}, \tag{2.63}$$

$$(l_1+l_2+l_3)\cdot\overline{n}, \tag{2.64}$$

from the gauge-dependent part of the gluon propagator. Because of the selector functions, we only need to consider a subset of them at a time.

Let us focus the case corresponding to the first row of Tab. 2.1, labelled “tpl. coll.". In this primary sector, the most obvious overlap singularity arises from the denominator (2.59). On top of that, propagators such as

$$(p-l_1-l_2)^2 = 2(l_1\cdot l_2-(l_1+l_2)\cdot p), \tag{2.65}$$

give rise to overlapping singularities, in the case of Eq. (2.65), an overlap of $E_1$ and $E_2$. As it was shown earlier, three relative angles can be parametrized such that, after the transformations (2.42) and (2.38), the scalar products behave as

$$\hat{l}_1\cdot\hat{l}_2\sim x_1, \qquad \hat{l}_2\cdot\hat{l}_3\sim x_2, \qquad \hat{l}_1\cdot\hat{l}_3\sim (x_1-x_2)^2, \tag{2.66}$$

and the energies behave as

$$E_1\sim x_3, \qquad E_2\sim x_4, \tag{2.67}$$

where $\hat{l}_i = l_i/E_i$.

The propagator denominators (2.59) and (2.65) can be written with some coefficients $A_i$, $B_i$ and $C_i$ in the form

$$(l_2\cdot l_3+l_1\cdot l_2+l_1\cdot l_3)^2 \sim ((x_1-x_2)^2x_4A_1+x_1x_3x_4B_1+x_2x_3C_1), \tag{2.68}$$

$$(l_1\cdot l_2-(l_1+l_2)\cdot p) \sim ((x_1-x_2)^2x_3x_4A_2+x_3B_2+x_4C_2), \tag{2.69}$$

which illustrates the complex structure of overlapping singularities.

The process of sector decomposition amounts to a recursive application of changes of variables as demonstrated in Sec. 1.4. In this primary sector (the fist of row of Tab. 2.1), for example, we obtain 13 secondary sectors.

A schematic view of sector decomposition for light-cone variables is shown in Fig. 2.6. While the decomposition in Fig. 2.6 is incomplete, it illustrates an im-

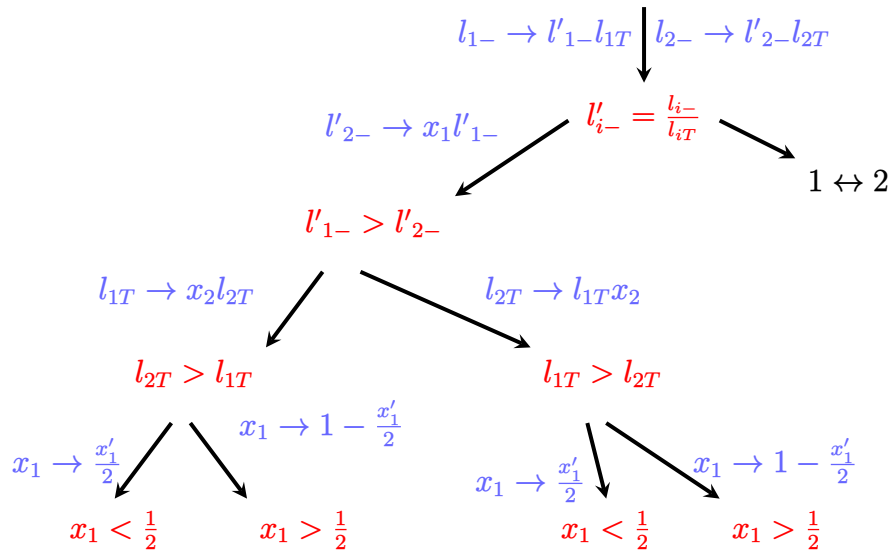


Figure 2.6: Schematic view of sector decomposition for minus components and transverse components. The variables $x_1$, $x_2$ and $x'_1$ are in the range $[0,1]$. As one can see, the condition at the nodes, effectively determine the order in which the limits are taken *cf.* Eq. (2.72).

portant aspect: that decomposition can be viewed as ordering of variables in size *cf.* Eq. (1.128). For example, by performing the decomposition

$$[l_{1T} \to x l_{2T}, \quad l_{2T} \to x l_{1T}]\,, \tag{2.70}$$

where $x \in [0,1]$, we are making sectors in which $l_{1T}$ and $l_{2T}$ are ordered differently:

$$[l_{1T} < l_{2T}, \quad l_{2T} < l_{1T}]\,. \tag{2.71}$$

As a result, after sector decomposition, taking the limits $x_i \to 0$ in different orders have to produce the same result. Naturally, divergences in the form of monomials satisfy such requirement. Conversely, there should be at least as many sectors as there are orders of limits one can take to get distinct divergences of the original expression. For example, *cf.* Sec. 1.4,

$$\frac{1}{x_1(x_1+x_2)} \sim \begin{cases} \frac{1}{x_1^2} & \text{for } x_2 \to 0,\ x_1 \to 0, \\ \frac{1}{x_1 x_2} & \text{for } x_1 \to 0,\ x_2 \to 0, \end{cases} \tag{2.72}$$

shows that we need two sectors, at least.

For the case of a combination of denominators (2.68) and (2.69), indeed, there are 13 different orders to take limits in which we get distinct divergences. Our decomposition satisfies this condition, which serves as a check of the method. After the full sector decomposition, the 39 primary sectors are further decomposed to 447 sectors in total. A Mathematica file in which the complete algorithm described above, valid at N$^3$LO is provided at
`https://github.com/Tomoki-Goda/Supplementary-materials.git`.

### 2.2.1 Laurent expansion and integration

Once the divergences are sorted out, as described in the previous section, they can be factored out as simple monomials. At N$^3$LO, we have

$$I = \int_0^1 \left[\prod_i dx_i\right] x_1^{-1+2\alpha} x_2^{-1-2\epsilon} x_3^{-1+\alpha-2\epsilon} x_4^{-1-2\alpha-3\epsilon} \mathcal{W}(x_1, x_2, \cdots; \epsilon, \alpha), \tag{2.73}$$

where the function $\mathcal{W}(x_1, x_2, \cdots; \epsilon, \alpha)$ is regular in each variable. We note that, in general, the powers of monomials in Eq. (2.73) is different for each sector. One can then proceed to apply the plus-prescription of Eq. (1.133). This, in practice, boils down to replacing the monomials by

$$x^{-1+a\epsilon+b\alpha} \to \frac{1}{a\epsilon+b\alpha}\delta(x) + \left[x^{-1+a\epsilon+b\alpha}\right]_+ . \tag{2.74}$$

Then, one gets

$$\begin{aligned}
I =& \frac{1}{2\alpha}\int_0^1 \left[\prod_{i\neq 1} dx_i\right] x_2^{-1-2\epsilon} x_3^{-1+\alpha-2\epsilon} x_4^{-1-2\alpha-3\epsilon} \mathcal{W}(0, x2, \cdots, x_i \cdots; \epsilon, \alpha) \\
&+ \int_0^1 \left[\prod_i dx_i\right] \left[x_1^{-1+2\alpha}\right]_+ x_2^{-1-2\epsilon} x_3^{-1+\alpha-2\epsilon} x_4^{-1-2\alpha-3\epsilon} \mathcal{W}(x_1, x_2, \cdots; \epsilon, \alpha) \\
=& \frac{1}{24\alpha\epsilon^3}\int_0^1 \left[\prod_{i\in\text{regular}} dx_i\right] \mathcal{W}^{(0,0)}(0, 0, \cdots, x_i \cdots) \\
&+ \frac{1}{144\epsilon^4}\int_0^1 \left[\prod_{i\in\text{regular}} dx_i\right] \mathcal{W}^{(0,0)}(0, 0, \cdots, x_i \cdots) + \cdots \\
&+ \int_0^1 \left[\prod_i dx_i\right] \left[x_1^{-1}\right]_+ \left[x_2^{-1}\right]_+ \left[x_3^{-1}\right]_+ \left[x_4^{-1}\right]_+ \mathcal{W}^{(0,0)}(x_1, x_2, \cdots) \\
&+ 2\alpha\int_0^1 \left[\prod_i dx_i\right] \left[\frac{\log(x_1)}{x_1}\right]_+ \left[x_2^{-1}\right]_+ \cdots \mathcal{W}^{(0,0)}(x_1, x_2, \cdots) + \cdots ,
\end{aligned} \tag{2.75}$$

where, in the second equality, expansions around $\alpha = 0$ and $\epsilon = 0$ are performed including the plus distributions, and $\mathcal{W}^{(i,j)}(\cdots)$ denote coefficients of Taylor expansion of $\mathcal{W}(\cdots; \epsilon, \alpha)$. We stress that the expansion in $\alpha$ has to be performed before that in $\epsilon$.

### 2.2.2 Numerical integration

The integrals in Eq. (2.75) can now, in principle, be evaluated numerically for a given value of $z$. In practice, the evaluations of $\lim_{x_i\to 0} \mathcal{W}^{(i_\epsilon, i_\alpha)}(\cdots, x_i, \cdots)$ are highly non-trivial and require proper treatments in order to avoid numerical instabilities. While they are by construction regular in those limits, in reality, the naive evaluation often yields 0/0, thus it is ill defined.

In order to circumvent this problem, we evaluate the limits in the following way.

At the level of the integrand, expressed in terms of scalar products, the size of the expression is moderate and can still be handled. The exact parametrizations of the scalar products, however, are not necessarily simple, particularly after the sector decomposition and the integration over a non-diverging variable with the delta function $\delta(\sum_i l_{i-} - (1-z))$. This prevents one to handle the expression explicitly in the variables $x_i$. One can instead hide the complexity within the scalar products, and apply sector decompositions to them. For the scalar products which are parametrized to vanish in the limits $x_i \to 0$, one can naturally have the corresponding variables factored out. Thus, the scalar products can be written in the form

$$v_i \cdot v_j = x_1^{p_1} x_2^{p_2} x_3^{p_3} x_4^{p_4} \; sp(v_i \cdot v_j) \qquad \text{where} \qquad sp(v_i \cdot v_j)\big|_{x_i=0} \neq 0. \tag{2.76}$$

While the genuine poles can be extracted in this manner, there remain some spurious poles which involve cancellations among the *sp* functions.

We observed that the majority of the spurious poles is related to combinations of momenta, $l_i - l_j$. For a triple-collinear limit, two variables describe angular configurations relative to $n$ and each other after the non-linear transformation of Eq. (2.42) is applied. Let them be $x_1$ and $x_2$ here. Then, the scalar products $l_i \cdot n$, $l_j \cdot n$ and $l_i \cdot l_j$, for example, scale respectively as $x_1$, $x_2$ and $|x_1 - x_2|$ in those variables. Consider $[x_1] - [x_2]$, where [ ] means that they are hidden inside scalar products. Sector decomposition transforms this expression, for example, as follows

$$[x_1] - [x_2] \qquad \to \qquad [x_1 x_2] - [x_2] \qquad \to \qquad [(1 - \frac{x_1}{2})x_2] - [x_2]. \tag{2.77}$$

When the scaling is extracted as in Eq. (2.76), it reveals only one of the overall scalings:

$$x_2 \left( [(1 - \frac{x_1}{2})] - [1] \right) = \frac{x_1 x_2}{2}. \tag{2.78}$$

This demonstrates, that , for example, in an expression $\frac{(l_1 - l_2)\cdot n}{l_1 \cdot l_2}$ a spurious pole may arise, which can only be removed when the hidden scalings, as in Eq. (2.78), are realized.

A Mathematica program was written to search and extract such hidden scalings, and with this, one could take the limits $x_i \to 0$ safely. Once the relevant limits of $\mathcal{W}^{(i,j)}$ are obtained, the integrations can be performed. For thiss purpose, we used PARNI [110] Monte-Carlo integration library.

## 2.3 Refactorization and renormalization

As a part of the renormalization procedure discussed in Sec. 1.1, one replaces a bare coupling with a running coupling, which, in $\overline{\text{MS}}$ scheme, are related by

$$a_s^b = \xi_\alpha(\mu^2) Z_\alpha(\mu^2) a_s(\mu^2), \tag{2.79}$$

where

$$a_s = \frac{\alpha_s}{4\pi} = \frac{g_s}{(4\pi)^2}, \tag{2.80}$$

and

$$\xi_\alpha(\mu^2) = \left(\frac{\mu^2}{4\pi e^{-\gamma_E}}\right)^\epsilon, \tag{2.81}$$

$$Z_\alpha(\mu^2) = 1 - a_s(\mu^2)\left(\frac{\beta_0}{\epsilon}\right) + a_s^2(\mu^2)\left(\frac{\beta_0^2}{\epsilon^2} - \frac{\beta_1}{2\epsilon}\right) + \mathcal{O}(a_s^3(\mu^2)). \tag{2.82}$$

This leads to the following expansion of the beam functions:

$$\begin{aligned}
&\mathcal{B}^{(0)_{\rm ren}} + a_s^b \mathcal{B}^{(1)_{\rm ren}} + a_s^{b^2} \mathcal{B}^{(2)_{\rm ren}} + a_s^{b^3} \mathcal{B}^{(3)_{\rm ren}} \\
&\qquad = \mathcal{B}^{(0)} + a_s \xi_\alpha \mathcal{B}^{(1)} + a_s^2 \left(\xi_\alpha^2 \mathcal{B}^{(2)} - \frac{\beta_0 \xi_\alpha}{\epsilon} \mathcal{B}^{(1)}\right) \\
&\qquad\quad + a_s^3 \left(\xi_\alpha^3 \mathcal{B}^{(3)} - \frac{2\beta_0 \xi_\alpha^2}{\epsilon} \mathcal{B}^{(2)} + \left(\frac{\beta_0^2 \xi_\alpha}{\epsilon^2} - \frac{\beta_1 \xi_\alpha}{2\epsilon}\right) \mathcal{B}^{(1)}\right),
\end{aligned} \tag{2.83}$$

where the factors $\xi_\alpha$ are often absorbed inside $\mathcal{B}$ [38], and we suppressed the arguments $(z, x_T^2)$ and the label $i/j$ of the beam functions in order to simplify the argument. The subscript "ren" is added to differentiate the coefficients of un-renormalized and renormalized couplings. Therefore, we see that the latter receive contributions from lower order results. Additionally, one needs to consider a product of beam functions in order to cancel the poles in $\alpha$, *cf.* Eq. (1.115). Thus, at $\mathcal{O}(\alpha_s^3(\mu))$, one has

$$\begin{aligned}
\left[\mathcal{B}\overline{\mathcal{B}}\right]^{(3)_{\rm ren}} &= \left\{\mathcal{B}^{(1)}\left[\overline{\mathcal{B}}^{(2)}_{RR} + \overline{\mathcal{B}}^{(2)}_{RV} - \frac{\beta_0}{\epsilon}\overline{\mathcal{B}}^{(1)}\right]\right. \\
&\left. + \mathcal{B}^{(0)}\left[\overline{\mathcal{B}}^{(3)}_{RRR} + \overline{\mathcal{B}}^{(3)}_{RRV} + \overline{\mathcal{B}}^{(3)}_{RVV} - \frac{2\beta_0}{\epsilon}\left(\overline{\mathcal{B}}^{(2)}_{RR} + \overline{\mathcal{B}}^{(2)}_{RV}\right) + \left(\frac{\beta_0^2}{\epsilon^2} - \frac{\beta_1}{2\epsilon}\right)\overline{\mathcal{B}}^{(1)}\right]\right\} \\
&+ \left\{\mathcal{B} \leftrightarrow \overline{\mathcal{B}},\right\},
\end{aligned} \tag{2.84}$$

which must be regular in $\alpha$. The subscripts $R$ and $V$ denote the real and virtual emissions, respectively.

For the NNLO case, one observes that the $\alpha$ poles cancel within each $\{\ldots\}$ of

$$\begin{aligned}
\left[\mathcal{B}\overline{\mathcal{B}}\right]^{(2)_{\rm ren}} &= \left\{\mathcal{B}^{(1)}\overline{\mathcal{B}}^{(1)} + \mathcal{B}^{(1)}\overline{\mathcal{B}}^{(1)} + \mathcal{B}^{(0)}\overline{\mathcal{B}}^{(2)}_{RR} + \overline{\mathcal{B}}^{(0)}\mathcal{B}^{(2)}_{RR}\right\} \\
&\quad + \left\{\mathcal{B}^{(0)}\overline{\mathcal{B}}^{(2)}_{RV} + \overline{\mathcal{B}}^{(0)}\mathcal{B}^{(2)}_{RV}\right\} - \left\{\frac{\beta_0}{\epsilon}\mathcal{B}^{(0)}\overline{\mathcal{B}}^{(1)} + \frac{\beta_0}{\epsilon}\overline{\mathcal{B}}^{(0)}\mathcal{B}^{(1)}\right\}.
\end{aligned} \tag{2.85}$$

This is simply because the cancellations must occur regardless of the values of $\mu$ and $\nu$, *cf.* Eqs. (2.79), (2.26) and (2.27). That is, the cancellation occurs within each coefficient of un-renormalized coupling, and also within the contributions with the same total number of real emissions[1].

[1] A product of beam functions scales as $\nu^r$ for $r$ total real emissions of the collinear and anti-collinear beam functions, see Eqs. (2.26) and (2.27).

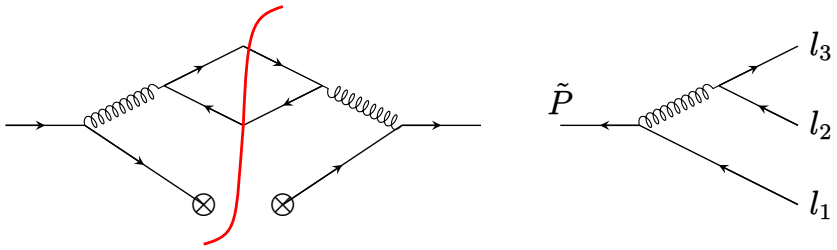


Figure 2.7: Left: $q \to qq'\bar{q}'g$ contribution at NNLO. Right: kinematics of time-like splitting.

At N$^3$LO, we have and analogous structure

$$\begin{aligned}
\left[\mathcal{B}\overline{\mathcal{B}}\right]^{(3)_{\rm ren}} = &\left\{\mathcal{B}^{(1)}\overline{\mathcal{B}}^{(2)}_{RR} + \overline{\mathcal{B}}^{(1)}\mathcal{B}^{(2)}_{RR} + \mathcal{B}^{(0)}\overline{\mathcal{B}}^{(3)}_{RRR} + \overline{\mathcal{B}}^{(0)}\mathcal{B}^{(3)}_{RRR}\right\} \\
&+ \left\{\mathcal{B}^{(1)}\overline{\mathcal{B}}^{(2)}_{RV} + \overline{\mathcal{B}}^{(1)}\mathcal{B}^{(2)}_{RV} + \mathcal{B}^{(0)}\overline{\mathcal{B}}^{(3)}_{RVV} + \overline{\mathcal{B}}^{(0)}\mathcal{B}^{(3)}_{RVV}\right\} \\
&+ \left\{\mathcal{B}^{(0)}\overline{\mathcal{B}}^{(3)}_{RRV} + \overline{\mathcal{B}}^{(0)}\mathcal{B}^{(3)}_{RRV}\right\} \\
&- \frac{\beta_0}{\epsilon}\left\{\mathcal{B}^{(1)}\overline{\mathcal{B}}^{(1)} + \overline{\mathcal{B}}^{(1)}\mathcal{B}^{(1)} + 2\mathcal{B}^{(0)}\overline{\mathcal{B}}^{(2)}_{RR} + 2\overline{\mathcal{B}}^{(0)}\mathcal{B}^{(2)}_{RR}\right\} \\
&- \frac{2\beta_0}{\epsilon}\left\{\mathcal{B}^{(0)}\overline{\mathcal{B}}^{(2)}_{RV} + \overline{\mathcal{B}}^{(0)}\mathcal{B}^{(2)}_{RV}\right\} \\
&+ \left(\frac{\beta_0^2}{\epsilon^2} - \frac{\beta_1}{2\epsilon}\right)\left\{\overline{\mathcal{B}}^{(1)}\mathcal{B}^{(0)} + \mathcal{B}^{(1)}\overline{\mathcal{B}}^{(0)}\right\},
\end{aligned} \tag{2.86}$$

where the cancellation of $\alpha$ poles in the last three lines is guaranteed from the NNLO calculation. For the problem at hand, the cancellation of $\alpha$ poles within the first line can serve as a test of $\mathcal{B}^{(3)}_{RRR}$. We note that in general, as one goes higher in the expansion in $\alpha_s$, higher orders in $\alpha$ and $\epsilon$ are required, which can be explained as follows: consider $\mathcal{B}^{(i)}$, which has at most $1/\epsilon^j$ pole, then, in order to obtain $\epsilon^0$ term of $\mathcal{B}^{(i)}\overline{\mathcal{B}}^{(k)}$, one needs up to $\epsilon^j$ term of $\overline{\mathcal{B}}^{(k)}$.

## 2.4 NNLO example

As a first test of the method, we show explicitly the steps of calculations at NNLO, which can be compared to the literature. At this level, our method is not strictly necessary, however, it is still useful for outlining some technical details.

Let us consider the contribution depicted on the left-hand side of Fig. 2.7, where a real $q\bar{q}$ pair is emitted. We first compute the time-like splitting depicted on the right-hand side of Fig. 2.7. As discussed in Sec. 2.1.2, the splitting amplitude is given by

$$M_{q\to qq'\bar{q}'g} = ig_s^2 t^a_{ij} t^b_{kl}\bar{v}(\tilde{P})\gamma^\mu v(l_1)\frac{\delta_{ab}d^{\mu\nu}}{(l_2+l_3)^2}\bar{u}(l_3)\gamma^\mu v(l_2), \tag{2.87}$$

where

$$\tilde{P} = -\sum_i l_i + \frac{s_{123}}{2\bar{n}\cdot\tilde{P}}\bar{n}, \tag{2.88}$$

| no. | transverse sizes | relative angles | energies |
|---|---|---|---|
| 1 | $l_{1T}$ | $\hat{l}_1 \cdot \hat{l}_2$ | $E_1$ |
| 2 | $l_{1T}$ | $\hat{l}_1 \cdot n$ | $E_1$ |
| 3 | $l_{1T}$ | $\hat{l}_1 \cdot \overline{n}$ | $E_1$ |
| | $l_{1T}$ | $\hat{l}_1 \cdot \overline{n}$ | $E_1^{-1}$ |
| 4 | $l_{1T}$ | $\hat{l}_1 \cdot n \quad \hat{l}_2 \cdot \overline{n}$ | $E_2^{-1}$ |
| 5 | $l_{2T}$ | $\hat{l}_1 \cdot \overline{n} \quad \hat{l}_2 \cdot n$ | $E_1^{-1}$ |
| 6 | $l_{2T}$ | $\hat{l}_2 \cdot \overline{n}$ | $E_2$ |
| 7 | $l_{2T}$ | $\hat{l}_1 \cdot \hat{l}_2$ | $E_2$ |
| 8 | $l_{2T}$ | $\hat{l}_2 \cdot n$ | $E_2$ |
| | $l_{2T}$ | $\hat{l}_2 \cdot \overline{n}$ | $E_2^{-1}$ |

Table 2.2: Vanishing variables of 8 primary sectors for two real emissions, where $\hat{l}_i = l_i/E_i$. *cf.* Tab. (2.1) and Eq. (2.49).

and

$$d^{\mu\nu} = \left[ g^{\mu\nu} - \frac{(l_1+l_2)^\mu \overline{n}^\nu + (l_1+l_2)^\nu \overline{n}^\mu}{\overline{n}\cdot(l_1+l_2)} \right]. \tag{2.89}$$

The colour matrices in Eq. (2.87) can be evaluated to be

$$t^a_{ij} t^b_{kl} \delta^{ab} = T_F \left( \delta_{il}\delta_{jk} - \frac{1}{N_c}\delta_{ij}\delta_{kl} \right), \tag{2.90}$$

thus, when squared, we get a factor of $T_F^2(N_c^2-1)$, which becomes $T_F C_F$, when averaged over colour. In fact, this is the only contribution to $\mathcal{B}^{(2)}_{q/q}$ which is proportional to $C_F T_T n_f$, and thus the validity of our calculation can be verified by comparing with the result of Ref. [38].

With the standard Dirac-Clifford algebra, implemented in FeynCalc/FenArts [104–108], we reproduces the result of Ref. [102]:

$$\begin{aligned} \left| M_{q\to qq'\overline{q}'g} \right|^2 =& 4g_s^2 C_F T_F \frac{s_{123}}{2s_{23}} \\ & \times \left( (1-2\epsilon)\left( (z_2+z_3) - \frac{s_{23}}{s_{123}} \right) - \frac{t_{231}^2}{s_{123}s_{23}} + \frac{4z_1 + (z_2-z_3)^2}{z_2+z_3} \right), \end{aligned} \tag{2.91}$$

where

$$t_{231} = \frac{2(s_{13}z_2 - s_{12}z_3)}{z_2+z_3} + \frac{s_{23}(z_2-z_3)}{z_2+z_3}, \tag{2.92}$$

and

$$s_{ij} = (l_i + l_j)^2, \qquad z_i = \frac{l_i \cdot n}{p\cdot\overline{n}}. \tag{2.93}$$

Crossing to the space-like splitting can be achieve by the following momentum replacements for the legs of the emitted particles: $l_2, l_3 \to -l_1, -l_2$, ( see Fig.2.5) and the renaming $l_1 \to p$ and $p \to p - l_1 - l_2$.

After the crossing and rescaling, one find a term in the matrix element, which we

shall denote by $A$

$$A = \frac{2(l_{1-}+l_{2-}-1)(l_{1+}l_{2-}-l_{1-}l_{2+})^2}{(l_1\cdot l_2)^2(l_{1-}+l_{2-})^2(l_{1+}+l_{2+}-2l_1\cdot l_2)^2}. \tag{2.94}$$

Now let us consider an integral

$$I = \int_0^\infty \frac{d^dl_1}{(2\pi)^{d-1}}\frac{d^dl_2}{(2\pi)^{d-1}}\left(\frac{\nu}{l_{1+}}\right)^\alpha\left(\frac{\nu}{l_{2+}}\right)^\alpha \delta^+(l_1^2)\delta^+(l_2^2) \times \delta\left(l_{1-}+l_{2-}-(1-z)\right)|l_{1\perp}+l_{2\perp}|^2\, e^{-|l_{1\perp}+l_{2\perp}|^2} A. \tag{2.95}$$

Let us first analyse the term (2.94). It has three types of denominators:

$$l_1\cdot l_2, \qquad 2l_1\cdot l_2 - l_{1+} - l_{2+}, \qquad l_{1-}+l_{2-}. \tag{2.96}$$

These three denominators have their origin in the internal propagators depicted in Fig. 2.8. For the gluon propagator, we have an additional denominator $\overline{n}\cdot(l_1+l_2)$ from the axial gauge gluon propagator, *cf.* Eq. (1.9).

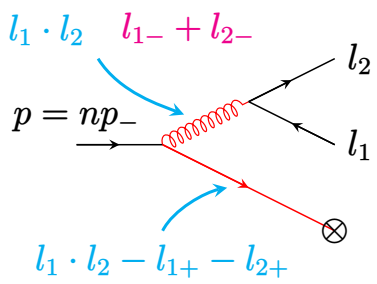


Figure 2.8

The first denominator is associated with the collinear divergence of two momenta, while the other two are related to the double $n$-collinear and double $\overline{n}$-collinear divergences, respectively. One important point to note is that, due to the delta function

$$\delta(l_{1-}+l_{2-}-(1-z)), \tag{2.97}$$

the double $\overline{n}$-collinear divergence is suppressed. Likewise, the exponent $e^{-(l_{1\perp}+l_{2\perp})^2}$ suppresses the double $n$-collinear divergence. Therefore, what remains is the $l_1, l_2$-collinear divergence. At first sight, it appears to be more divergent than $1/x$, however, the numerator also vanishes in the same $l_1, l_2$-collinear limit. In order to see how this scales, we parametrise the momenta as

$$\begin{aligned} l_1 &= E_1(1,\ 0,\ \sin\theta_1,\ \cos\theta_1),\\ l_2 &= E_2(1,\ \sin\chi_1\sin\chi_2,\ \cos\chi_2\cos\theta_1\sin\chi_1+\cos\chi_1\sin\theta_1,\\ &\qquad\qquad \cos\chi_1\cos\theta_1-\cos\chi_2\sin\chi_1\sin\theta_1), \end{aligned} \tag{2.98}$$

such that $l_1\cdot l_2 = E_1E_2(1+\cos\chi_1)$. There are 8 primary sectors at NNLO, as we summarize in Tab. 2.2.

Let us take an example of primary sectors in which $\chi_1$ and $E_1$ potentially leads to divergence (row 1 in Tab. 2.2), and further parametrize in the unit hyper cube of $x_i$ variables,

$$\cos\chi_1 = -1+2x_2, \qquad E_1 = \frac{x_1}{1-x_1}. \tag{2.99}$$

The rest of the variables are guaranteed to be trivial thanks to the selector function,

*i.e.* the first element in (2.54). That is to say, any limit other than $x_1, x_2 \to 0$ is regular by construction. Therefore, the knowledge of variables other than $x_1$ and $x_2$ is redundant and can be hidden. Scalings of the scalar products can be extracted as

$$l_1 \cdot l_2 = x_1 x_2 sp(l_1 \cdot l_2), \qquad l_{1\perp} \cdot l_{2\perp} = x_1 sp(l_{1\perp} \cdot l_{2\perp}), \tag{2.100}$$
$$l_1 \cdot n = x_1 sp(l_1 \cdot n), \qquad l_1 \cdot \overline{n} = x_1 sp(l_1 \cdot \overline{n}), \tag{2.101}$$
$$l_2 \cdot n = sp(l_2 \cdot n), \qquad l_2 \cdot \overline{n} = sp(l_2 \cdot \overline{n}), \tag{2.102}$$
$$l_{1\perp} \cdot l_{1\perp} = x_1^2 sp(l_{1\perp} \cdot l_{1\perp}), \qquad l_{2\perp} \cdot l_{2\perp} = sp(l_{2\perp} \cdot l_{2\perp}), \tag{2.103}$$

where $sp(l_i \cdot l_j)$ are the non-scaling parts of $l_i \cdot l_j$ (*i.e.* $\lim_{x_1,x_2\to 0} sp(l_i \cdot l_j) \neq 0$).

Ignoring trivial Jacobian and the selector function and letting $\epsilon$, $\alpha \to 0$, the integrand of Eq. (2.95) reads

$$\propto \frac{x_1 z (sp(l_{1+})sp(l_{2-}) - sp(l_{1-})sp(l_{2+}))^2}{x_2^2 (sp(l_1 \cdot l_2))^2 (x_1 sp(l_{1-}) + sp(l_{2-})^2 (x_1 x_2 sp(l_1 \cdot l_2) - x_1 sp(l_{1+}) - sp(l_{2+}))^2}. \tag{2.104}$$

While it is not divergent in the limit $x_1 \to 0$, divergence in $x_2$ appears to be too strong. Similarly to the discussion in Sec 2.2.2, $sp(l_{1+})sp(l_{2-}) - sp(l_{1-})sp(l_{2+})$ indeed scales as $\sim \sqrt{x_2}$ and reads

$$\sqrt{x_2} \frac{((1-z)y_1 - 2x_1 y_3)\left(2(x_4 - y_4)\sqrt{y_2 x_3 y_3} + \sqrt{x_2}(x_3 - y_3)\right)}{y_1^2\left(2(x_4 - y_4)\sqrt{x_2 x_3 y_2 y_3} + x_2(x_3 - y_4) + y_3\right)}, \tag{2.105}$$

where

$$y_i \equiv 1 - x_i, \tag{2.106}$$

which reduces the power of the divergence in (2.104) to $x_2^{-1}$. Once such scaling combinations are found, it suffices to replace one of the $sp$ functions, for example

$$sp(l_{2+}) \to \frac{sp(l_{1+})sp(l_{2-}) - \sqrt{x_2} sp'(l_{2+})}{sp(l_{1-})}, \tag{2.107}$$

such that the spurious poles are cancelled without increasing complexity of the expression. The new function $sp'(l_{2+})$ behaves much like the other $sp$ functions, while it is no longer related to $l_{2+}$. Applying this technique recursively, one eventually arrives at integrands whose singularities take forms of simple monomials.

As we saw earlier, some expressions do vanish in the limit $x_i \to 0$. In fact, Eq. (2.91) vanishes in the soft limits (*i.e.* single soft limit of $g \to q\overline{q}$ is not divergent. *cf.* AP kernel $P_{qg}$, Eq. (1.44)). Consequently, the first pole is $\epsilon^{-1}$. At this order in $\epsilon$, there are two sectors which contribute, and they are both $l_1, l_2$-collinear sectors, with different momenta allowed to be soft (*i.e.* row 1 and 7 in Tab. 2.2). The scaling of

the integrand is $x_1^{-1-\alpha-2\epsilon}x_2^{-1-\epsilon}$. Therefore, it can be expanded as

$$\begin{aligned}
&I^{(2,2),1}_{\mathcal{B}_{q/q,\,n_f C_F T_F}}(z)\\
=&(2\pi)^{-2(d-1)}\int dx_3 dx_4\left[\alpha\left(-\frac{\mathcal{W}(0,0)}{4\epsilon^3}+\frac{\int dx_2\left(\frac{1}{x_2}\right)_+\mathcal{W}(0,x_2)}{4\epsilon^2}\right)+\frac{\mathcal{W}(0,0)}{2\epsilon^2}\right.\\
&\left.-\frac{\int dx_1\left(\frac{1}{x_1}\right)_+\mathcal{W}(x_1,0)}{\epsilon}-\frac{\int dx_2\left(\frac{1}{x_2}\right)_+\mathcal{W}(0,x_2)}{2\epsilon}+\mathcal{O}\left(\left(\frac{\alpha}{\epsilon}\right)^2,\epsilon^0\right)\right] \qquad (2.108)\\
=&-(2\pi)^{-2(d-1)}\int dx_1 x_3 dx_4\frac{\left(\frac{1}{x_1}\right)_+\mathcal{W}^{(0,0)}(x_1,0)}{\epsilon}+\mathcal{O}\left(\left(\frac{\alpha}{\epsilon}\right)^2,\epsilon^0\right)\\
=&-\frac{(2\pi)^{-2(d-1)}}{\epsilon}\int dx_1 x_3 dx_4\frac{\mathcal{W}^{(0,0)}(x_1,0)}{x_1}+\mathcal{O}\left(\left(\frac{\alpha}{\epsilon}\right)^2,\epsilon^0\right),
\end{aligned}$$

where dependencies on other variables and parameters are implicit We have used above, the fact that, in the soft limit

$$\lim_{x_1\to 0}\mathcal{W}(x_1,x_2)=0. \qquad (2.109)$$

The additional super script "1" in Eq. (2.108) denotes that it is the contribution from the primary sector 1 ( see Tab. 2.2), and the subscript $n_f C_F T_F$ denotes that it is the coefficient of this colour factor. The integration of the last line of Eq. (2.108) is three dimensional and can be performed analytically with Mathematica. Since the full integrand is too large to be presented here, we show only the $x_1$-integrated result:

$$\int dx_1\frac{\mathcal{W}^{(0,0)}(x_1,0)}{x_1}=\frac{-\pi(1-z)\left(\left(-8x_4^2+8x_4-1\right)z+z^2+1\right)}{3(1-x_3)^2\sqrt{(1-x_4)x_4}}e^{-\frac{x_3}{1-x_3}(1-z)^2}. \qquad (2.110)$$

This has an integrable singularity at $x_4=0,\,1$, which can potentially spoil numerical accuracy. Such singularities can be removed by a change of variables

$$x_i\to(1-x_i^2)^2, \qquad (2.111)$$

whose Jacobian is $4x_i(1-x_i^2)$, hence

$$\begin{aligned}
&\int dx_1\frac{\mathcal{W}^{(0,0)}(x_1,0)}{x_1}\\
=&\frac{-2\pi(1-z)\left(\left(-8x_4^8+32x_4^6-40x_4^4+16x_4^2-1\right)z+z^2+1\right)}{3(1-x_3)^2\sqrt{2-x_4^2}}e^{-\frac{x_3}{1-x_3}(1-z)^2}.
\end{aligned} \qquad (2.112)$$

Further integrations over $x_3$ and $x_4$ yield

$$I^{(2,2)}_{\mathcal{B}_{q/q,\,n_f C_F T_F}}(z)=(2\pi)^{-2(d-1)}\frac{-2\pi^2(1+z^2)}{3\epsilon(1-z)}+\mathcal{O}\left(\epsilon^0,\frac{\alpha}{\epsilon}\right), \qquad (2.113)$$

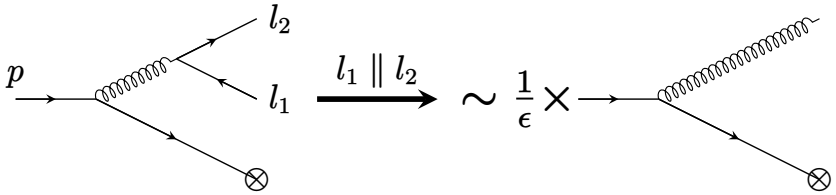


Figure 2.9: By taking the $l_1, l_2$-collinear limit of $q \to qq'\overline{q}'$, one gets a configuration of $q \to qg$ at the leading order in the Laurent expansion.

where the factor of 2 was inserted to account for the two contributing sectors, thus we drop the super script. We notice that this result (2.113) has the same dependence on $z$ as $P_{qq}$, Eq. (1.43). Moreover, Eq. (2.113) is in deed proportional to the NLO beam function in $q \to gq$ channel [38]. This is because we are taking the collinear limit of a $q\bar{q}$ pair which originates from a gluon, as it is shown schematically in Fig. 2.9.

Note that we have a divergence at $z = 1$ in Eq. (2.113), which would have been, in fact, regularized by $\alpha$, had we kept $\alpha$ finite in the calculation. This can be seen by considering an integral with a test function $f(l_{1-}, l_{2-})$:

$$I = \int dl_{1-} dl_{2-} \left(\frac{\nu}{l_{1-}}\right)^{\alpha} \left(\frac{\nu}{l_{2-}}\right)^{\alpha} \delta(p_- - (1-z)(l_{1-} + l_{2-})) f(l_{1-}, l_{2-}). \tag{2.114}$$

Using the delta function,

$$\begin{aligned} I &= \int dl_{1-} \frac{1}{1-z} \left(\frac{\nu}{l_{1-}}\right)^{\alpha} \left(\frac{\nu}{p_-/(1-z) - l_{1-}}\right)^{\alpha} f\left(l_{1-}, \frac{p_-}{(1-z)} - l_{1-}\right) \\ &= \int dl_{1-} \left(\frac{\nu}{l_{1-}}\right)^{\alpha} \left(\frac{\nu}{p_- - (1-z) l_{1-}}\right)^{\alpha} (1-z)^{-1+\alpha} f\left(l_{1-}, \frac{p_-}{(1-z)} - l_{1-}\right), \end{aligned} \tag{2.115}$$

hence, $z = 1$ is regularized by $\alpha$.

Taking this into consideration, the correct result is recovered:

$$\frac{-2\pi^2(1+z^2)}{3\epsilon(1-z)} \to -\frac{2\pi^2}{3\epsilon} \left(\frac{2}{\alpha}\delta(1-z) + \frac{(1+z^2)}{(1-z)_+} + \mathcal{O}(\alpha)\right). \tag{2.116}$$

This, in fact, makes our calculation of leading $\epsilon$ insufficient at $z = 1$. While $\alpha$ poles cancel at the end, we have terms proportional to $\frac{\alpha}{\epsilon}$ in higher order of expansion

$$x_i^{-1+a\epsilon+b\alpha} \to \frac{1}{b\epsilon} + \frac{a\alpha}{b^2\epsilon^2} + \mathcal{O}\left(\epsilon^0, \frac{\alpha}{\epsilon}\right), \tag{2.117}$$

which, when combined, makes additional contribution to the leading $\epsilon$ pole. Nonetheless, we will for the moment consider the case $z \neq 1$.

In order to compare the result (2.113) with the literature, we need to multiply it by the factor from Eqs. (2.31) and (2.81). This factor gives additional power of $\epsilon$, thus the leading order is $\mathcal{O}(\epsilon^{-2})$.

To the first three leading orders in $\epsilon$ at $z = 1/3$, our numerical results (test) show

perfect agreement with Ref. [38] (ref) the numerical errors:

$$\mathcal{B}^{\text{test}}_{C_F T_F n_f}(1/3, x_T^2) = \frac{2.22}{\epsilon^2} + \frac{4.44 L_\perp + 1.27}{\epsilon} + 4.44 L_\perp^2 + 2.55 L_\perp + 6.85, \tag{2.118}$$

$$\mathcal{B}^{\text{ref}}_{C_F T_F n_f}(1/3, x_T^2) = \frac{2.22}{\epsilon^2} + \frac{4.44 L_\perp + 1.26}{\epsilon} + 4.44 L_\perp^2 + 2.53 L_\perp + 6.95, \tag{2.119}$$

$$\overline{\mathcal{B}}^{\text{test}}_{C_F T_F n_f}(1/3, x_T^2) = \frac{2.22}{\epsilon^2} + \frac{4.44 L_\perp + 1.26}{\epsilon} + 4.44 L_\perp^2 + 2.51 L_\perp + 6.92, \tag{2.120}$$

$$\overline{\mathcal{B}}^{\text{ref}}_{C_F T_F n_f}(1/3, x_T^2) = \frac{2.22}{\epsilon^2} + \frac{4.44 L_\perp + 1.26}{\epsilon} + 4.44 L_\perp^2 + 2.53 L_\perp + 6.95. \tag{2.121}$$

where we estimate the error to be $\lesssim 5\%$.

### 2.4.1 Numerical results at N$^3$LO

Before discussing our numerical result at N$^3$LO, we would like to point out that, in fact, we obtained an important result in the previous example of the NNLO calculation, which is necessary for the calculation of the N$^3$LO beam function, namely a new term in the NNLO beam function

$$\frac{4(1+z^2)\alpha}{3\epsilon^3 (1-z)_+}, \tag{2.122}$$

which originates from Eq. (2.113).

This is absent in the result of Ref. [38], since it goes beyond $\alpha^0$ order. However, in our formulation, the term (2.122) appears at leading-order in $\epsilon$ and next-to-leading order in $\alpha/\epsilon$ due to the expansion of the prefactor, Eq. (2.31):

$$C(x_T, 2, 2, \alpha, \epsilon) = -\frac{1}{2\epsilon} + \frac{\alpha}{2\epsilon^2} + \mathcal{O}\left(\epsilon^0, \left(\frac{\alpha}{\epsilon}\right)^2\right). \tag{2.123}$$

We now turn to the calculation of the quark-to-quark beam function at N$^3$LO focusing on the $n_f C_F^2 T_F$ colour factor. The building blocks presented so far in this chapter was implemented entirely in Mathematica [111], except for the numerical integration. Starting from the matrix elements, we apply the algorithm presented above, which leads to the expression (2.75). Each plus-prescribed integral can be evaluated numerically for a given value of $z$, which we did with PARNI Monte-Carlo integration library [110].

As discussed earlier, products of beam functions expanded in $\alpha_s$, as in Eq. (2.86) form groups, within which $\alpha$ poles cancel. For the case at hand, cancellation of $\alpha$ poles involves only the first group of terms in Eq. (2.86). Let us call the sum of these terms $R$:

$$\begin{aligned} R(z_1, z_2) =& \mathcal{B}^{(1)}(z_1)\overline{\mathcal{B}}^{(2)}_{RR}(z_2) + \overline{\mathcal{B}}^{(1)}(z_2)\mathcal{B}^{(2)}_{RR}(z_1) \\ &+ \mathcal{B}^{(0)}(z_1)\overline{\mathcal{B}}^{(3)}_{RRR}(z_2) + \overline{\mathcal{B}}^{(0)}(z_2)\mathcal{B}^{(3)}_{RRR}(z_1) \\ =& \mathcal{B}^{(1)}(z_2)\overline{\mathcal{B}}^{(2)}_{RR}(z_1) + \overline{\mathcal{B}}^{(1)}(z_1)\mathcal{B}^{(2)}_{RR}(z_2) \\ &+ \delta(1-z_2)\overline{\mathcal{B}}^{(3)}_{RRR}(z_1) + \delta(1-z_1)\mathcal{B}^{(3)}_{RRR}(z_2), \end{aligned} \tag{2.124}$$

where, in the second equality, we used Eq. (2.1), and for the moment we will suppress the argument $x_T$ for simplicity. By considering the case where $z_2 \neq 1$, the delta functions multiplying $\overline{\mathcal{B}}^{(3)}_{RRR}(z_1)$ vanish and one is left with

$$R(z_1, z_2 \neq 1) = \mathcal{B}^{(1)}(z_2)\overline{\mathcal{B}}^{(2)}_{RR}(z_1) + \overline{\mathcal{B}}^{(1)}(z_1)\mathcal{B}^{(2)}_{RR}(z_2) + \delta(1-z_1)\mathcal{B}^{(3)}_{RRR}(z_2). \tag{2.125}$$

Therefore, $\alpha$-pole cancellation can be checked by taking the limit $\alpha \to 0$ of

$$R(1, z_2 \neq 1) = \underbrace{\mathcal{B}^{(1)}(z_2)\overline{\mathcal{B}}^{(2)}_{RR}(1) + \overline{\mathcal{B}}^{(1)}(1)\mathcal{B}^{(2)}_{RR}(z_2)}_{\text{known}} + \mathcal{B}^{(3)}_{RRR}(z_2), \tag{2.126}$$

which must be regular in this limit. The first two terms in Eq. (2.126) are available in Ref. [38], and considering the case $z_2 = 1/2$, we get

$$\begin{aligned} &\mathcal{B}^{(1)}\left(\frac{1}{2}\right)\overline{\mathcal{B}}^{(2)}_{RR}(1) + \overline{\mathcal{B}}^{(1)}(1)\mathcal{B}^{(2)}_{RR}\left(\frac{1}{2}\right) \\ &\qquad = -\mathcal{B}^{(1)}(1)\overline{\mathcal{B}}^{(2)}_{RR}\left(\frac{1}{2}\right) - \overline{\mathcal{B}}^{(1)}\left(\frac{1}{2}\right)\mathcal{B}^{(2)}_{RR}(1) \\ &\approx \frac{C_F^2 T_F n f}{\alpha}\left(-\frac{20.}{\epsilon^3} - \frac{23.}{\epsilon^2} - \frac{95.}{\epsilon} + \mathcal{O}\left(\epsilon^0\right)\right) \\ &\qquad + \mathcal{O}(\alpha^0) + \text{other colour factors.} \end{aligned} \tag{2.127}$$

From our direct calculation, we obtain [99]

$$\mathcal{B}^{(3)}_{q/q,\, n_f C_F^2 T_F}\left(\frac{1}{2}, x_T^2\right) = \frac{1}{\alpha}\left(-\frac{20.}{\epsilon^3} - \frac{23.}{\epsilon^2} - \frac{97.}{\epsilon} + \mathcal{O}\left(\epsilon^0\right)\right) + \mathcal{O}(\alpha^0)\,, \tag{2.128}$$

$$\overline{\mathcal{B}}^{(3)}_{q/q,\, n_f C_F^2 T_F}\left(\frac{1}{2}, x_T^2\right) = \frac{1}{\alpha}\left(\frac{20.}{\epsilon^3} + \frac{23.}{\epsilon^2} + \frac{97.}{\epsilon} + \mathcal{O}\left(\epsilon^0\right)\right) + \mathcal{O}(\alpha^0), \tag{2.129}$$

where we estimate the numerical accuracy to be $\sim 2-3\%$. We see the cancellation (2.126) of the *ap* poles between Eq. (2.127) and our results (2.128) and (2.129), which is a strong validation of our approach.

The next check to the result is the renormalization group equations [34,42]. However, this requires the knowledge of the virtual contributions, *cf.* (2.86).

## 2.5 Summary of the chapter

In this chapter, we have discussed construction of a scheme needed for calculation of the N$^3$LO beam functions. This required, in particular, extraction of all singularities generated by the final-state emissions. According to the KLN theorem, IR divergences of loops and real emissions cancel when the observable under consideration is sufficiently inclusive.

In order to accomplish the extraction, two main concepts had to be introduced: *selector functions* [45–47] and *sector decomposition* [43, 44]. The former selectively suppress subsets of divergences, thus allowing, otherwise unfeasible, optimal parametrization of momenta for the Laurent expansions of divergences. The latter

disentangles, and further simplifies the divergences, which have, in general, complex structures.

The calculation was carried out in the light-cone gauge, which is characterised by the gauge-dependent part of the gluon propagator (1.9). As discussed in Sec. 2.1.3, in addition to the soft and collinear divergences, beam functions exhibit the so-called *rapidity divergence*. These divergences are not regularized by the standard dimensional regularization, and require an additional regulator. We employed the so-called *analytic regulator* [33, 39], $\alpha$, whose poles cancel when a product of the collinear and anti-collinear beam functions are considered. After the cancellation, hard-scale dependence remains, but it can be further factorized and exponentiated. Physical divergences which appear in the renormalized beam functions can be either removed by multiplicative $Z$ factor, which is related to the IR divergences in QCD, or absorbed in side collinear PDFs.

At the end of this chapter we used the complete algorithm to compute the $\alpha$-pole part of the beam function and anti-beam function at N$^3$LO, and found that the two contributions cancel in the product as required.

# Chapter 3

# TMDs at small $x$ and saturation

## 3.1 Theoretical framework

### 3.1.1 Models of dipole cross section

The dipole cross section, which we saw in Eq. (1.163), is an integral over the impact parameter $b$ of the dipole amplitude $\mathcal{N}$, which appeared in Eq. (1.147):

$$\sigma_{\text{dipole}}(x,r) = 2\int d^2\mathbf{b}\,\mathcal{N}(x,r,\mathbf{b})\,. \tag{3.1}$$

In order to stay consistent with the Froissart bound (1.144), $\mathcal{N}$ has to satisfy the so called *black disk limit* [48], which restricts $\mathcal{N} < 1$. The factor 2 in Eq. (3.1) is related to the optical theorem [48]. For a constant, $\theta$-like, proton profile, the integration over the impact parameter yields $\frac{\sigma_0}{2} = \pi R^2$, where $R$ is an effective size of the proton. One may also consider more realistic $b$-profiles [112]. One of possible consequences of the $b$-dependence is that the $\sigma_{\text{dipole}}(x,r)$ may rise logarithmically in the saturated region, see Ref. [112]. This is still in agreement with the Froissart bound, which limits the growth not to be steeper than $\sim \ln^2(s)$. The interpretation is that the cross section is limited by the growth of the effective size of the target (black disk), which grows logarithmically [71].

As discussed in Sec. 1.7, the dipole amplitude can be obtained by solving, for example, the non-linear evolution equations like BK (1.147) [54,55] or more general JIMWLK (1.175) [113–118]. Nevertheless, it is often useful to have a simple model, which may also be used as an initial condition for the evolution. The Golec-Biernat–Wüsthoff (GBW) saturation model [73, 75] is one of such examples and it is also popular as an initial condition parametrization [57, 119–121].

In the GBW saturation model, the dipole cross section is parametrized as

$$\sigma_{\text{GBW}}(x,r) = \sigma_0\left(1 - e^{-r^2\frac{Q_s^2(x)}{4}}\right), \qquad \text{where} \qquad Q_s^2(x) = Q_0^2\left(\frac{x_0}{x}\right)^{\lambda}. \tag{3.2}$$

The parameters $\{\sigma_0, x_0, \lambda\}$ were fitted to DIS data for $F_2$ [122–125]. It was also

proposed to replace [73]

$$x \to x\left(1 + \frac{4m_f^2}{Q^2}\right), \tag{3.3}$$

such that, for $m_f \neq 0$, the small-$Q^2$ limit remains finite. We discussed in Sec. 1.6 that this replacement has its origin in the gluon kinematics, *cf.* Eq. (1.163).

What is important in Eq. (3.2) is that, when the dipole size $r$ is small, the dipole cross section scales as

$$\sigma_{\mathrm{GBW}}|_{r \ll Q_s} \approx \sigma_0 \frac{r^2 Q_s^2(x)}{4}, \tag{3.4}$$

whereas, as $r$ grows, the cross section saturates at $\sigma_0$. The transition to the region where the saturation behaviour is dominant is governed by the $x$-dependent saturation scale $Q_s(x)$.

Another feature of the GBW model is that the dipole cross section depends only on $rQ_s(x)$ rather than two variables $r$ and $x$ separately. This behaviour is called the *geometric scaling* [59]. We have previously discussed this phenomenon in the context of the BK equation, *cf.* Eq. (1.147). Both the solutions of the BK equation and experimental data support the existence of such behaviour [50, 59, 126].

While the GBW model showed remarkable success in description of experimental data with its simple form, its validity was restricted to the region of relatively small $Q$. In order to describe the data at higher photon virtualites, Bartels, Golec-Biernat and Kowalski (BGK) proposed an improved model [70]. In order to account for the small-$r$ limit, Eq. (1.166), the dipole cross section was modified as follows:

$$\sigma_{\mathrm{BGK}} = \sigma_0 \left(1 - \exp\left[-r^2 \frac{\pi^2 \alpha_s(\mu) x g(x,\mu)}{N_c \sigma_0}\right]\right), \tag{3.5}$$

where

$$\mu = \frac{C}{r^2} + \mu_0^2 \qquad \text{and} \qquad x g(x, Q_0^2) = A_g x^{-\lambda_g} (1-x)^{5.6}. \tag{3.6}$$

Thus, the fit parameters of the BGK model are: $\{\sigma_0,\, A_g,\, \lambda_g,\, C,\, \mu_0\}$. This can be thought of as an eikonalized extrapolation of the small-$r$ limit described in Ref. [72]. This form renders the dipole cross section in the correct small-$r$ limit, Eq. (1.166), while in the large-$r$ limit, where $\mu \approx \mu_0 \gtrsim Q_0$, recovers the behaviour of the GBW model.

The models presented above assume $\theta$-like profile of the proton, thus a proton is effectively treated as a fixed-size, uniform disk. Plots of the dipole cross sections and the dipole gluon densities of the GBW and BGK models are presented in Fig. 3.1. At the bottom of each subplot, coloured contour is shown. In the top row, the dipole cross sections of the two models are shown. Overall, they are similar in shape, and the areas in pink correspond to the saturated region (plateau), while the areas in blue correspond to the colour-transparency region ($\sim r^2$). The figures visualize concepts of the colour-transparency region and the saturated regions, and that the latter expands to lower-$r$ regions as $x$ decreases. The BGK model shows stronger decrease in moderate- to large-$x$ region as $x$ grows. This is largely due to the factor $(1-x)^{5.6}$ in the gluon

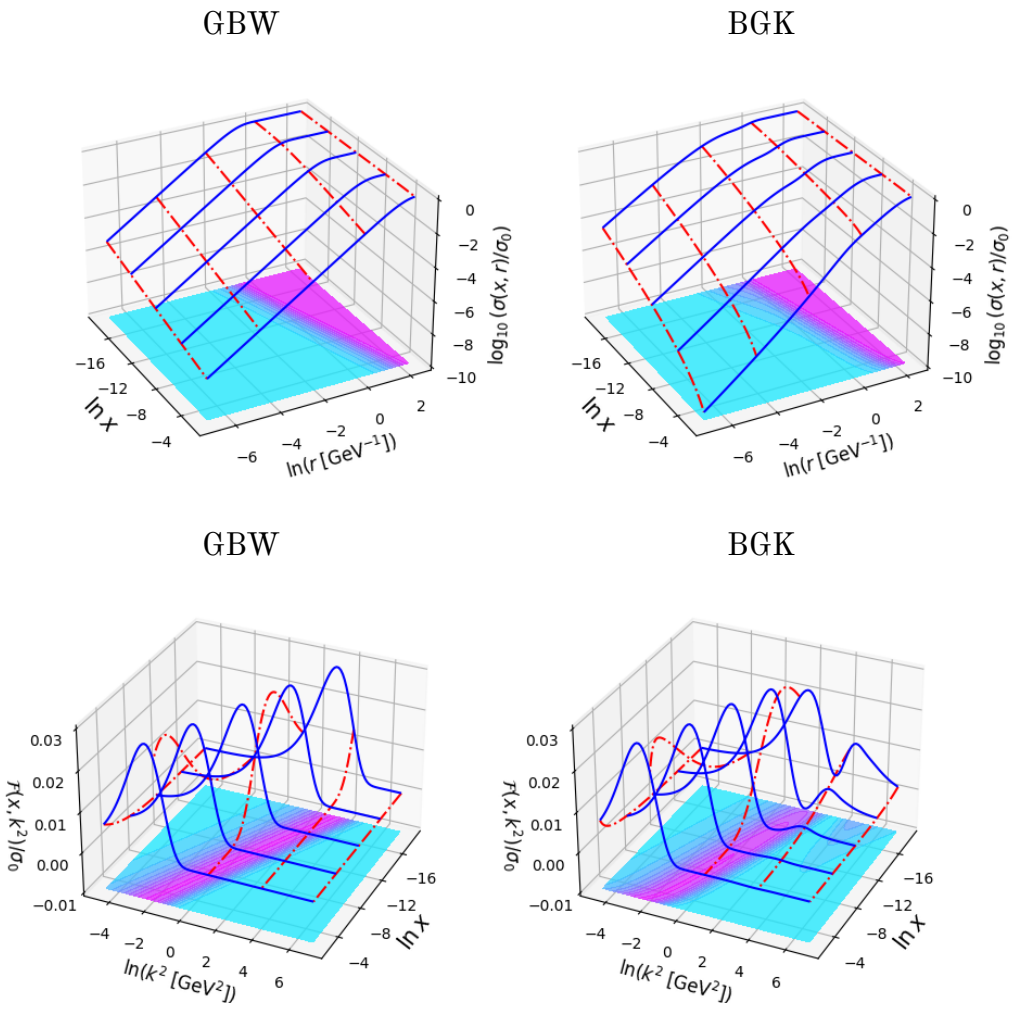


Figure 3.1: Top: An example of dipole cross sections, $\sigma_{\text{dipole}}(x,r)/\sigma_0$. Bottom: An example of dipole gluon densities, $\mathcal{F}^{\text{dipole}}(x,k^2)/\sigma_0$.

density. The bottom row shows the dipole gluon densities computed from the models as Eq. (1.165). The differences between those of the GBW and BGK models are clearly visible. The BGK gluon gets a second bump in the small-$x$ region due to DGLAP evolution [70]. It is also worth pointing out that the shapes of the lines in blue for the GBW model are the same over $x$ (*i.e.* the blue lines are identical up to a shift), while that of the BGK model no longer shows such a feature. This is a consequence of the loss of geometric scaling.

One may in principle incorporate a little more realistic proton profile, which was achieved by Kowalsky and Teaney (KT) [112], as yet another extension to the GBW and BGK models, in which the exponent was multiplied by a Gaussian profile function. In a simpler version, Ref. [85], one may consider a factorized impact parameter profile

$$\mathcal{N}(x,b,r) = N(x,r)T(b). \tag{3.7}$$

In the case of the KT model, the resulting dipole cross section after integration over the impact parameter rises logarithmically at large $r$. In fact, a form in which the

dipole cross section rises logarithmically was considered already in the first paper of Golec-Biernat and Wüsthoff [73] (see also Ref. [72] for the methods of unitarization).

### 3.1.2 Saturation scale

As already discussed, the saturation scale is an intrinsic scale in the saturation phenomenon, and it is a key element in the models. The pioneering work of Gribov Levin and Ryskin (GLR) [52] has incorporated recombination of gluons at the level of collinear gluon density in the proton. Let us consider an unintegrated gluon density defined by (*cf.* Eq. (1.157)) [69, 71]

$$\frac{\partial xg(x,k_T^2)}{\partial k_T^2} \simeq \mathcal{F}(x,k_T). \tag{3.8}$$

By re-expressing the Gribov–Levin–Ryskin–Muller–Qiu (GLR–MQ) equation (1.145) as [48, 52, 53]

$$\frac{\partial^2 xg(x,Q^2)}{\partial \ln(1/x)\partial \ln(Q^2)} = \frac{\alpha_s N_c}{\pi} xg(x,Q^2) - \frac{\alpha_s^2 N_c \pi}{2C_F S_\perp Q^2}[xg(x,Q^2)]^2, \tag{3.9}$$

the saturation scale can be defined as a scale at which the linear term and the non-linear term of the above are of the same order, *i.e.*

$$\frac{\partial^2 xg(x,Q^2)}{\partial x \partial Q^2} \approx 0. \tag{3.10}$$

By combining this with Eq. (3.8), one obtains the condition

$$\frac{\partial \mathcal{F}(x,k^2)}{\partial x} \approx 0. \tag{3.11}$$

This condition is met at the ridge (peak) of the unintegrated gluon density in the $(x,k_T^2)$ space. The pink bands in the contour plots of the bottom row of Fig. 3.1, which shows $\alpha_s \mathcal{F}(x,k_T^2)$ obtained from the GBW and BGK models, can be thought of as the saturation scale. The figures show clearly the ridge around $k_T \sim 1\text{GeV}$. This line of $Q_s^2(x)$ in the $(x,k_T^2)$ space is called the *saturation line* (and historically also called the *critical line*). In the GBW model, where

$$\alpha_s \mathcal{F}_{\text{GBW}}^{\text{dipole}} = \sigma_0 \frac{N_c}{(2\pi)^2} \frac{k_T^2}{Q_S^2} e^{-\frac{k_T^2}{Q_S^2}}, \tag{3.12}$$

the ridge corresponds to

$$\frac{\partial \alpha_s \mathcal{F}_{\text{GBW}}^{\text{dipole}}}{\partial x} = \sigma_0 \frac{\partial Q_s^2}{\partial x} \frac{N_c}{(2\pi)^2} \frac{k_T^2}{Q_s^6} \left(k_T^2 - Q_s^2\right) e^{-\frac{k_T^2}{Q_S^2}} = 0. \tag{3.13}$$

Therefore, one sees that the condition is met at $k_T^2 = Q_s^2$. We note Eq. (3.8) is true only in DLLA, while Eq. 3.9 describes effects beyond DLLA. Therefore, the above

argument should not be regarded as rigorous. Nevertheless, it is useful as it illustrates important feature of the model. In the original GBW model, the saturation scale was defined as a scale where

$$\sigma_{\text{dipole}} = \sigma_0 \left(1 - e^{-1}\right) \approx 0.63\sigma_0. \tag{3.14}$$

The condition (3.14) can be used as a definition of the saturation scale also for the BGK model [127].

However in general, the dipole cross section can rise logarithmically [73,86,112], thus the definition Eq. (3.14) may become unsuitable and it is more advantageous to consider the transverse momentum at which the unintegrated gluon peaks as the saturation scale. In other words, it can be interpreted as a typical $k_T$ scale of gluons at a given $x$.

### 3.1.3 Sudakov form factor

As already discussed, in cases where the transverse momentum is not comparable with the hard scale of a process in consideration, one encounters the Sudakov type large logarithms $\ln(Q^2/k_t^2)$, which should, in principle, be resummed [40]. The Sudakov form factor is related to soft emissions which give small transverse momentum to the parton entering the hard collision. In the language of parton branching, it is also referred to as a survival factor [22, 128], due to the interpretation of the Sudakov form factor as a probability of parton evolving without emitting any particle between two scales.

The hard scale dependence in the leading-$\log(1/x)$ approximation is a subleading effect. Thus, one may expect that introduction of a hard scale into the dipole cross section enhances the moderate-$x$ region. As shown in Refs. [129,130], simultaneous resummation of $\ln(1/x)$ and $\ln(Q^2/k_T^2)$ can be achieved consistently, owing to separation of contributing regions in the phase space. In particular, in Ref. [88], the Sudakov logarithms were resummed for the dipole gluon density.

At leading order, the perturbative Sudakov factor reads [88]

$$S^{(1)}_{\text{pert}}(r, Q^2) = \frac{C_A}{2\pi} \int_{\mu_b^2}^{Q^2} \alpha(\mu^2) \frac{d\mu^2}{\mu^2} \ln\left(\frac{Q^2}{\mu^2}\right). \tag{3.15}$$

For the case of the running coupling $\alpha_s(\mu^2) = 1/(b_0 \ln \frac{\mu^2}{\Lambda^2_{\text{QCD}}})$ at LO, one gets

$$S^{(1)}_{\text{pert}}(r, Q^2) = \frac{C_A}{2\pi b_0} \Bigg[ - \ln\left(\frac{Q^2}{\mu_b^2}\right) + \left(\frac{1 + \alpha(\mu_b^2) b_0 \ln\left(\frac{Q^2}{\mu_b^2}\right)}{\alpha(\mu_b^2) b_0}\right) \ln\left(1 + \alpha(\mu_b^2) b_0 \ln\left(\frac{Q^2}{\mu_b^2}\right)\right) \Bigg], \tag{3.16}$$

where $b_0 = \frac{11C_A - 2n_f}{12}$. The lower limit of the integral is set to be

$$\mu_b = C_S/r, \tag{3.17}$$

where $C_S = 2e^{-\gamma_{\rm E}}$, and $\gamma_{\rm E} \approx 0.577$ is the Euler-Mascheroni constant.

In principle, one can include also the non-perturbative Sudakov factor [40, 131, 132]:

$$S(r, Q^2) = S_{\rm pert}(r, Q^2) + S_{\rm np}(r, Q^2), \tag{3.18}$$

where [131]

$$S_{\rm np}(r, Q^2) = g_1 r^2 + g_2 \ln\left(\frac{r}{r_*}\right) \ln\left(\frac{Q}{Q_0}\right). \tag{3.19}$$

Introduction of $r_*$ is paired with the modification of Eq. (3.17)

$$\mu_b^2 = C_S^2/r_*^2 \equiv C_S^2/r^2 + C_S^2/r_{\rm max}^2, \tag{3.20}$$

for some cut-off $r_{\rm max}$. The effect is such that stared variable $r_* < r_{\rm max}$ remains in the perturbative domain, and freezes the perturbative Sudakov factor when $r \gtrsim r_{\rm max}$, and in such region the non-perturbative Sudakov factor plays its role.

In our Sudakov-improved model of Ref. [133], the non-perturbative Sudakov factor was omitted since the effect was negligible. The details of its effects in the GBW model will be discussed later in Sec. 3.2.

The Sudakov form factor, $S(r, Q^2)$, can be included as follows. Firstly, by combining Eqs. (1.164) and (1.165) one can write

$$\sigma_{\rm dipole}(x, r) = \int \frac{d^2\mathbf{k}_t}{(2\pi)^2 k_T^2} \left(1 - e^{i\mathbf{k}_t \cdot \mathbf{r}}\right) \int d^2\mathbf{r}' e^{i\mathbf{k}_t \cdot \mathbf{r}'} \nabla_{\mathbf{r}'}^2 \sigma_{\rm dipole}(x, r'), \tag{3.21}$$

and following Ref. [88], the Sudakov factor can be inserted in the above to yield

$$\Sigma_{\rm dipole}(x, r, Q^2) = \int \frac{d^2\mathbf{k}_t}{(2\pi)^2 k_T^2} \left(1 - e^{i\mathbf{k}_t \cdot \mathbf{r}}\right) \int d^2\mathbf{r}' e^{i\mathbf{k}_t \cdot \mathbf{r}'} e^{-S(r', Q^2)} \nabla_{\mathbf{r}'}^2 \sigma_{\rm dipole}(x, r'). \tag{3.22}$$

A new object $\Sigma_{\rm dipole}$ on the left-hand side depends on the hard scale, $Q^2$. The integral can be partially performed analytically and one obtains [133]

$$\Sigma_{\rm dipole}(x, r, Q^2) = \int_0^r dr' r' \ln\left(\frac{r}{r'}\right) e^{-S(r', Q^2)} \nabla_{r'}^2 \sigma_{\rm dipole}(x, r'). \tag{3.23}$$

$\Sigma_{\rm dipole}(x, r, Q^2)$ is identical to $\sigma_{\rm dipole}(x, r, Q^2)$ if the Sudakov effects are ignored. This new function should be thought of as an object which appears in the dipole factorization, where it is defined by Eq. (1.160) rather than the dipole cross section defined with the CGC operators, Eq. (1.173).

| $\mu_{0S}^2$[GeV$^2$] | GBW + Sud$_{\text{pert}}$ | GBW + Sud$_{\text{pert+np}}$ |
|---|---|---|
| 1 | 2.71 | 2.72 |
| 2 | 2.66 | 2.67 |
| 3 | 2.64 | 2.65 |
| 4 | 2.64 | 2.64 |
| 5 | 2.64 | 2.65 |

| $\mu_{0S}^2$[GeV$^2$] | BGK + Sud$_{\text{pert}}$ | BGK + Sud$_{\text{pert+np}}$ |
|---|---|---|
| 1 | 1.18 | 1.17 |
| 2 | 1.21 | 1.17 |
| 3 | 1.25 | 1.21 |
| 4 | 1.29 | 1.21 |
| 5 | 1.32 | 1.22 |

Table 3.1: $\chi^2$/dof of fits with and without the non-perturbative Sudakov factor, with 5 values of $\mu_{0S}^2$ for the Sudakov factor. It is clear that when $\mu_{0S}^2$ is set small, the effect of non-perturbative Sudakov factor is negligible. It is interesting to see that, for the BGK model, inclusion of the non-perturbative factor indeed weakens the dependence on the choice of $\mu_{0S}$.

| type | light quark mass [GeV] | $\sigma_0$ [mb] | $x_0(10^{-4})$ | $\lambda$ | $\chi^2$/dof |
|---|---|---|---|---|---|
| GBW | $m_l = 0.14$ | 23.8 | 1.12 | 0.308 | 5.27 |
| GBW + Sud | $m_l = 0.14$ | 23.0 | 1.32 | 0.287 | 3.37 |
| GBW | $m_l = 0.0$ | 19.1 | 2.58 | 0.322 | 4.44 |
| GBW + Sud | $m_l = 0.0$ | 18.6 | 3.11 | 0.299 | 2.66 |

| type | light quark mass [GeV] | $\sigma_0$ [mb] | $A_g$ | $\lambda_g$ | $C$ | $\mu_0^2$ [GeV$^2$] | $\chi^2$/dof |
|---|---|---|---|---|---|---|---|
| BGK | $m_l = 0.14$ | 33.1 | 1.33 | 0.0553 | 0.420 | 1.76 | 1.62 |
| BGK + Sud | $m_l = 0.14$ | 30.7 | 6.28 | -0.380 | 0.677 | 3.09 | 1.27 |
| BGK | $m_l = 0.0$ | 23.3 | 1.18 | 0.0832 | 0.329 | 1.87 | 1.56 |
| BGK + Sud | $m_l = 0.0$ | 22.2 | 8.67 | -0.500 | 0.670 | 3.83 | 1.21 |

Table 3.2: The parameters and $\chi^2$ per degrees of freedom of the GBW and BGK models for the fit with the HERA data ($Q^2 < 650$ GeV$^2$). Two cases with massive light quarks and massless light quarks are presented.

## 3.2 Sudakov-improved GBW and BGK models

In this section the results of the fits of saturation models to HERA data are discussed. We have fitted the GBW and BGK models to the $F_2$ data from HERA [134], using Eq. (1.163), where the data were selected with the conditions

$$0.045 \leq Q^2 \leq 650 \text{ GeV}^2, \qquad x \leq 0.01, \tag{3.24}$$

for which there are 378 available data points.

Since we were not primarily concerned about the low-$Q^2$ limit, the replacement of Eq. (3.3) was not strictly necessary, hence two classes of fits were studied, where, in one case the light quark mass was set to zero, and in the other case it was set to 0.14 GeV. The charm and bottom quarks were taken into account with the masses 1.3 and 4.6 GeV respectively. Additionally, the forms of $\mu$ in Eq. (3.6) and $\mu_b$ in Eq. (3.20) were modified as proposed in Ref. [76]:

$$\mu_i^2 = \frac{\mu_{0i}^2}{1 - \exp\left[-r^2 \frac{\mu_{0i}^2}{C_i}\right]}, \tag{3.25}$$

where $\mu_{0i} = \mu_0$ and $C_i = C$, for the gluon in the BGK (3.6), and $\mu_{0i} = \mu_{0S}$ and $C_i = C_S = 2e^{-\gamma_E}$, for the parameters of the Sudakov factor (3.20).

Tab. 3.1 shows preliminary fit results with and without the non-perturbative Sudakov factor with several values of $\mu_{0S}$. For both cases, the effects are negligible for small values of $\mu_{0S}$. Therefore, a value $\mu_{0S}^2 = 2$ GeV$^2$, which produces reasonable result, was used. While the non-perturbative Sudakov factor is ignored, it is nonetheless interesting to see that for the BGK model, the non-pertirbative Sudakov factor reduces the effect of what value of $\mu_{0S}$ being used.

In Tab. 3.2, the results of the fit are summarized. In the top subtable, the parameters of the GBW model, with and without the Sudakov factor, for the cases of massive and massless cases are presented. Differences in $\sigma_0$ and $x_0$ are clear between the massive and massless light quarks cases. These differences are a natural consequence of the factor $(1+4m_f^2/Q^2)$ multiplying $x$, see Eq. (3.3), and Eq. (1.163). The effects of the Sudakov factor show similar trend for both the massive and massless light quarks cases. Even though changes in the parameters are moderate, the fit quality improves substantially. As it was the case in Refs. [76, 127] for inclusive DIS, the massless light quarks version appears to be preferred. In the bottom subtable of Tab. 3.2, the results of the BGK model for the same setups are summarized. Again, the effects of the light-quark mass and the Sudakov factor seem uncorrelated, and the Sudakov factor gives qualitatively similar effects in the massive and massless cases. The observation that the Sudakov form factor affects similarly to both massive and massless cases is related to the fact that the Sudakov factor acts at high-$Q$ region whereas the effects of mass is primarily prominent in the low-$Q$ region. The improvement in the BGK model is less significant compared to the GBW model, yet it is of the order of 20%. In comparison to the GBW model, the difference in fit quality between the massless and massive light quarks cases is small. One may also notice that $\lambda_g$ became negative in the new fit. This means that the initial condition on the collinear gluon no longer rises with $1/x$, and thus, the rise has to originate from the DGLAP evolution [70], which we have discussed in Sec. 1.5, *cf.* Eq. (1.140). For the rest of this section, only the massless light quarks case will be considered following Refs. [76, 127].

In the top row of Fig. 3.2, the resulting dipole cross sections are shown. The plots are normalized by $\sigma_0$ in order to make the differences of the other parameters more clearly visible. The left-hand side plot of the GBW model shows some effects in the scaling region. The effect is uniform over all range of $r \lesssim 1/Q_s$, and appears to make the $x$ dependence milder. On the right-hand side of Fig. 3.2, the BGK model is shown. In the transition region, near $1/Q_s$, the effect is uniform over both $r$ and $x$, increasing the cross section. In the small-$r$ region, the differences are bigger for larger $x$ and smaller $r$. This means that the region corresponding to large $Q$ and moderate $x$ is the most strongly affected. In the second row of Fig. 3.2, the dipole gluon density is plotted. Both the GBW and BGK models show similar patterns. The difference pointed out above can be also seen in the bottom row of Fig. 3.2, showing the saturation scale. On the left-hand side, one can see a milder dependence on $x$ for the case of the Sudakov-improved GBW model, while on the right-hand side, the saturation scale is almost uniformly lifted up.

Figs. 3.8 and 3.9 show how the models describe the data. At the bottom of each figure, the histogram gives the $\chi^2$-value at each value of $Q^2$. Clearly, for the GBW model there is a significant improvement at large $Q^2$, while for the BGK model, the

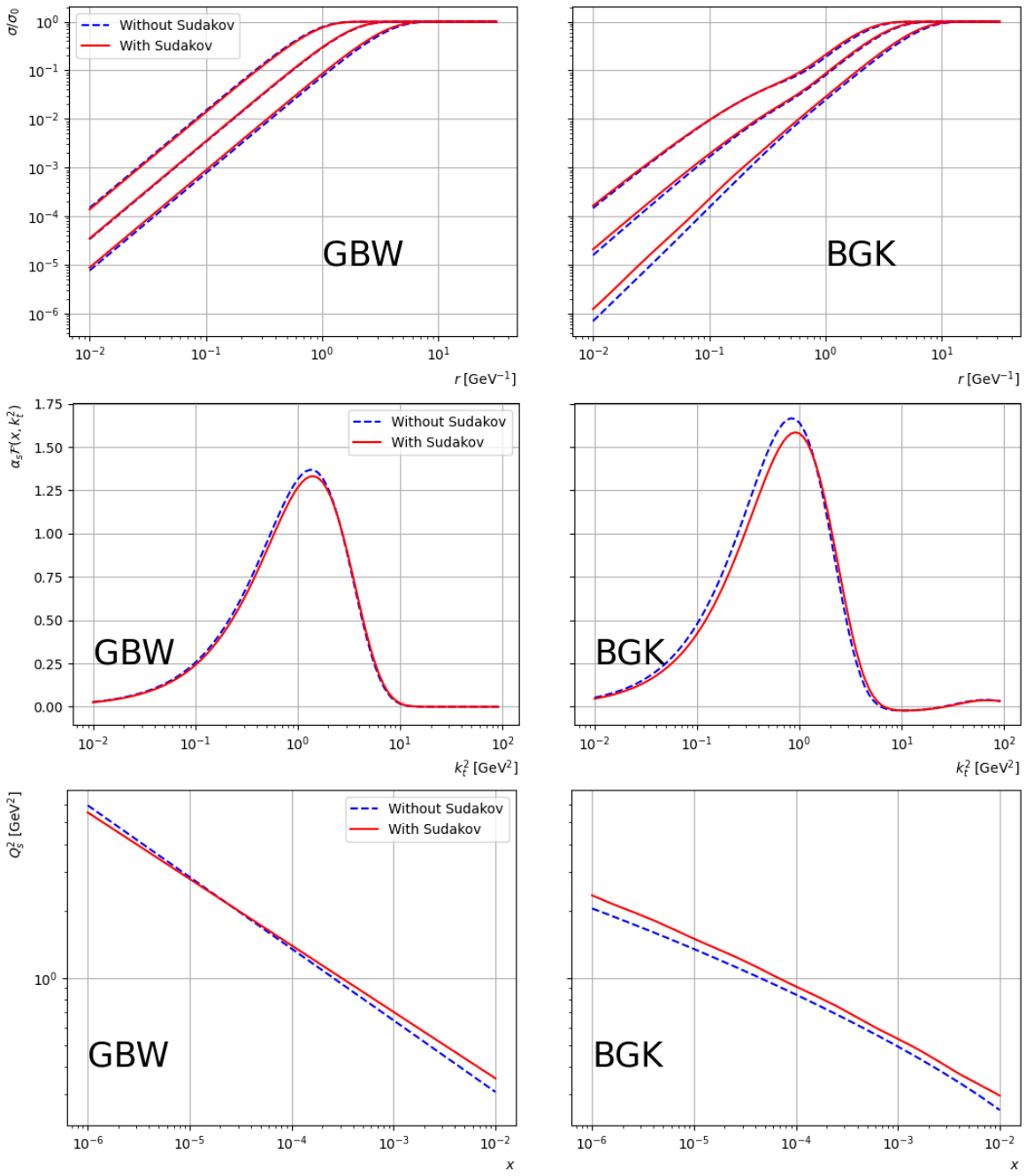


Figure 3.2: The dipole cross section, the dipole gluon density and the saturation scale of the GBW an BGK models. The dipole cross section is plotted for $x = 10^{-2}, 10^{-4}, 10^{-6}$.

improvement is even over the whole range of $Q^2$. However, when one looks at Fig. 3.9 closer, particularly around $Q^2 \sim 15$ GeV$^2$, one notices that the change is more prominent in the moderate-$x$ region. In fact, if one plots the $x$-slope of $F_2$, it becomes clearly visible (see Fig. 3.5), that indeed, the moderate-$x$ region receives the largest modification, while the GBW model shows uniform decrease in the $x$-slope. This effect is expected, as the hard scale dependence is a subleading effect in the leading $\log(1/x)$ approximation. Incorporation of such dependence delays the breakdown of the leading $\log(1/x)$ approximation. That is to say that it is expected that the Sudakov factor extends applicability of the model further to the moderate-$x$ region.

Fig. 3.6 shows the contour plots of gluon densities. As a reference, also the hard scale-dependent/independent non-linear Kutak–Sapeta (KS) gluon densities [135–137] are plotted. While they differ quantitatively, the qualitative effect of the inclusion of the Sudakov factor is similar. For both cases, the Sudakov factor suppresses the moderate-$x$ region. This is in agreement with a common treatment of the gluon density in the large-$x$ region, namely the multiplication by a factor $(1-x)^{2n_{\text{spectator}}-1}$ for $n_{\text{spectator}}$ spectator quarks [12, 138, 139]. In the plot of the BGK gluon, it is also visible that the Sudakov factor smears out the distribution wider. The plot also shows that the Sudakov factor has little effect on the saturation scale, while the profile of the gluon density changes substantially.

## 3.3 Effects of exact gluon kinematics in the GBW and BGK models

### 3.3.1 Dipole factorization revisited

As discussed in Sec. 3.1.1, the original GBW and BGK models were fitted using the dipole factorization formula (1.163), which is defined in position space. In this section, we shall discuss fits carried out in the framework of $k_T$-factorization [133] defined in momentum space, which we discussed in Sec. 1.6. With a change of a variable

$$\boldsymbol{\kappa}'_t \equiv \boldsymbol{\kappa}_t - (1-\beta)\mathbf{k}_t \,, \tag{3.26}$$

Eqs. (1.153) and (1.154) can be integrated analytically over the angle $\phi$ to yield [62, 74]

$$F_2(x,Q^2) = \sum_f e_f^2 \frac{Q^2}{2\pi} \int \frac{dk_t^2}{k_t^2} \int_0^1 d\beta \int d\kappa'_t \alpha_s(\mu^2) \mathcal{F}^{\text{dipole}}(x/z, k_t^2)\Theta(1-x/z) \\ \left[ \left(\beta^2 + (1-\beta)^2\right) \left(\frac{I_1}{2\pi} - \frac{I_2}{2\pi}\right) + \left(m_f^2 + 4Q^2\beta^2(1-\beta)^2\right) \left(\frac{I_3}{2\pi} - \frac{I_4}{2\pi}\right) \right], \tag{3.27}$$

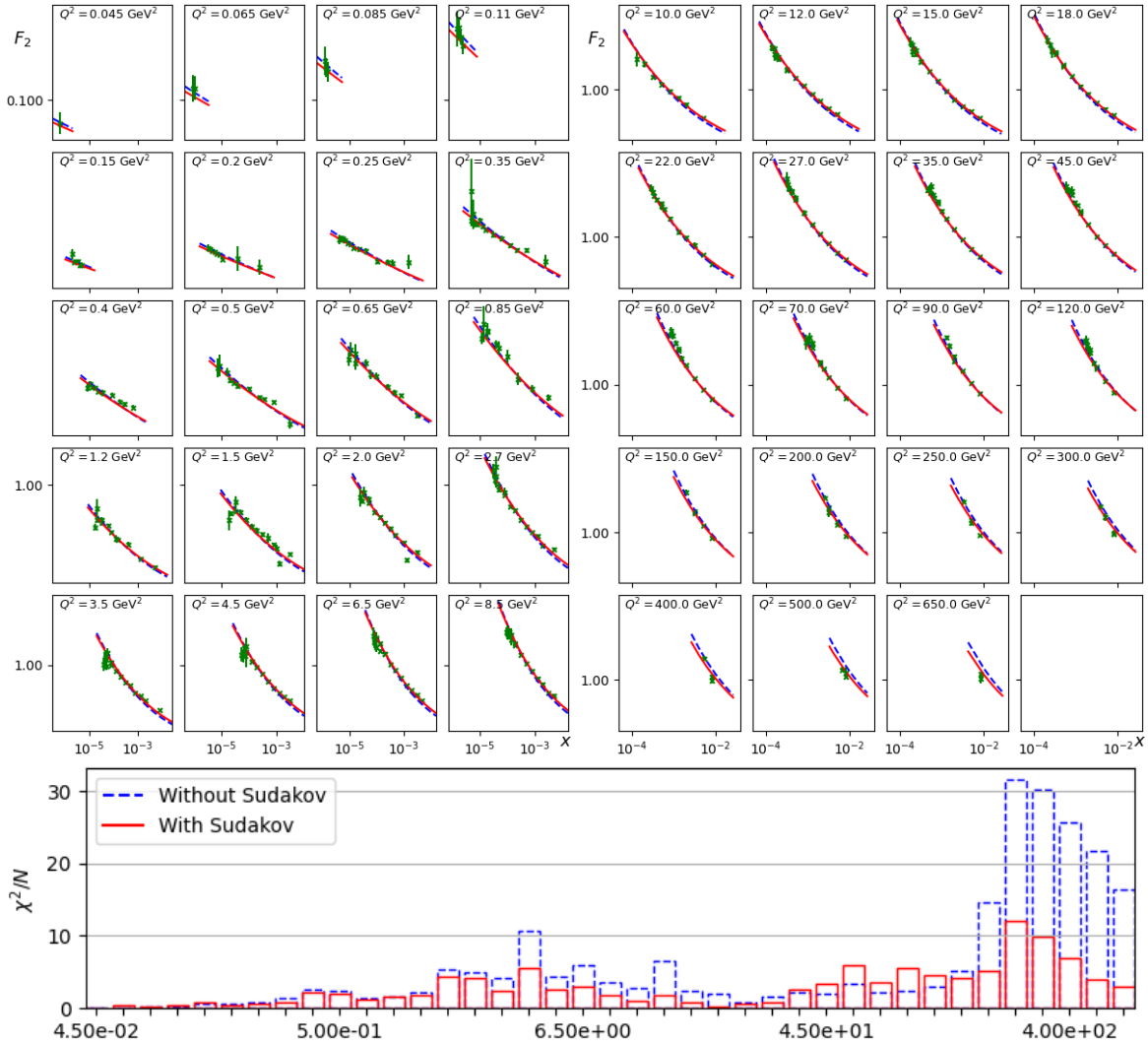


Figure 3.3: Comparison with $F_2$ data and the fit quality ($\chi^2$ per number of data points.)

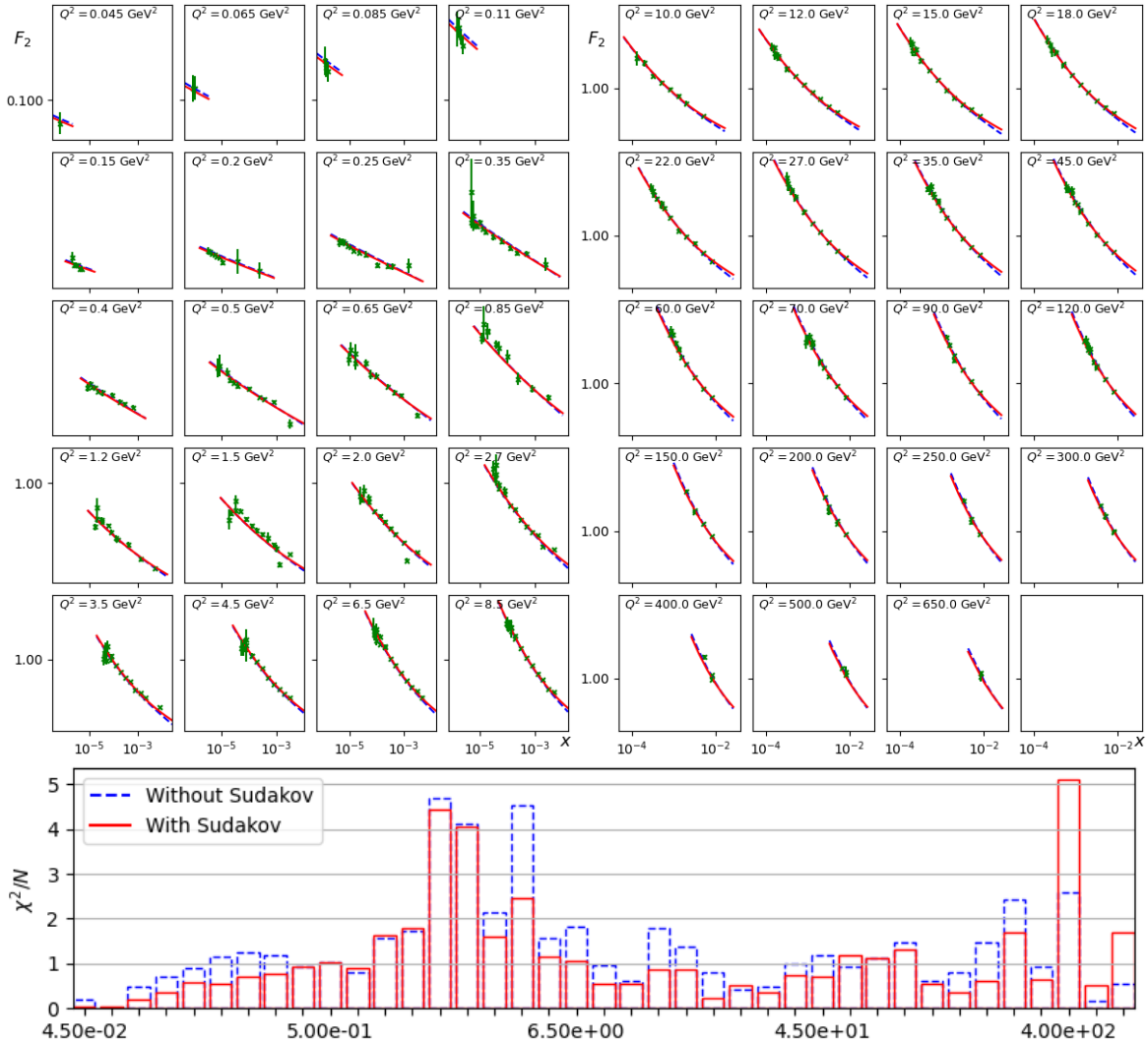


Figure 3.4: Comparison with $F_2$ data and the fit quality ($\chi^2$ per number of data points.)

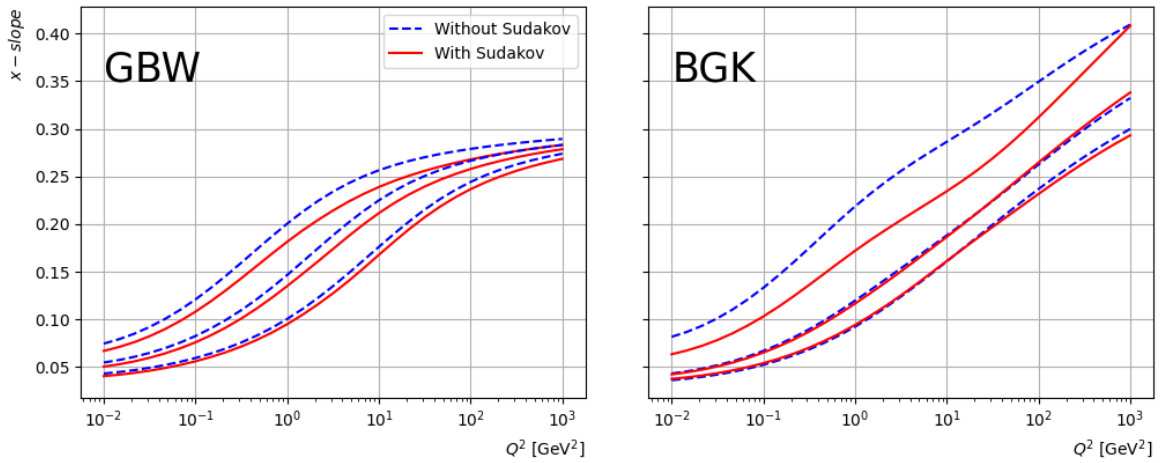


Figure 3.5: $x$-slope of $F_2$.

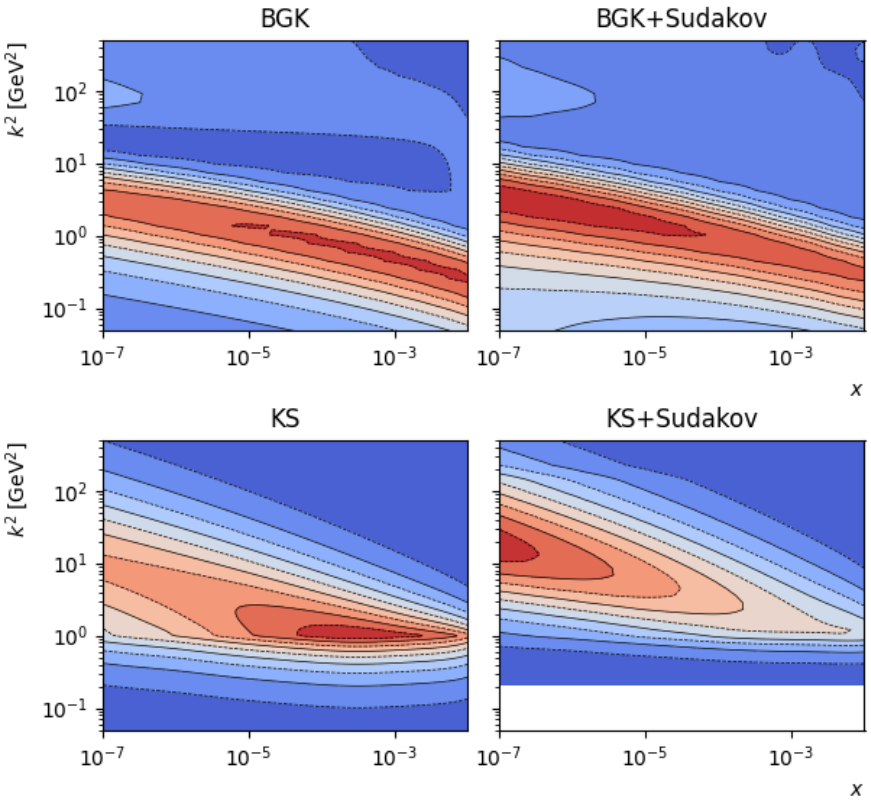


Figure 3.6: Comparison of KS and BGK gluon densities. $Q^2 = 175,\ 180\,\mathrm{GeV}^2$

where

$$\frac{I_1}{2\pi} = \frac{N_1 N_2 + N_3^2}{(N_1^2 + 2N_1 N_2 + N_3^2)^{3/2}}, \qquad \frac{I_2}{2\pi} = \frac{N_3 - (1-2\beta)N_1}{(N_1+N_4)\sqrt{N_1^2 + 2N_1 N_2 + N_3^2}},$$
$$\frac{I_3}{2\pi} = \frac{N_1 + N_2}{(N_1^2 + 2N_1 N_2 + N_3^2)^{3/2}}, \qquad \frac{I_4}{2\pi} = \frac{2(1-\beta)}{(N_1+N_4)\sqrt{N_1^2 + 2N_1 N_2 + N_3^2}}, \tag{3.28}$$

for

$$\begin{aligned} N_1 &\equiv \beta(1-\beta)Q^2 + m_f^2, & N_2 &\equiv \kappa_t'^2 + (1-\beta)^2 k_t^2, \\ N_3 &\equiv \kappa_t'^2 - (1-\beta)^2 k_t^2, & N_4 &\equiv \kappa_t'^2 + \beta(1-\beta)k_t^2. \end{aligned} \tag{3.29}$$

For the fitting, the form (3.27) of $k_T$-factorization was used. The gluon density is obtained by evaluating Eq. (1.165). In Sec. 1.6, it was discussed that the $k_T$-factorization enables one to fit the dipole cross section with exact gluon kinematics. In order to proceed, let us mention a few points concerning the gluon densities of the GBW and BGK models. For the GBW model, the gluon density, Eq. (1.165), can be obtained analytically:

$$\mathcal{F}^{\text{dipole}}_{\text{GBW}}(x, k_T^2) = \sigma_0 \frac{C_A}{4\pi^2} \frac{k_T^2}{Q_s^2} e^{-\frac{k_T^2}{Q_s^2}}. \tag{3.30}$$

For the BGK model, it has to be computed numerically. The direct numerical integration tends to be unstable due to high oscillation of the Bessel function, and thus the use of the method of Lyness [140], which we shall discuss in Sec. 3.3.2, is advantageous. Alternatively, in Ref. [141], the gluon density was matched to $\frac{\partial x g(x,\mu^2)}{\partial \mu^2}$ at high $k_T$, *cf.* Eqs. (3.8) and (1.157). Together with their treatment of the running coupling, the gluon density of Ref. [141] is positive definite, while for our case the gluon density can be negative. This, as discussed in Refs. [141, 142] originates from the behaviour of the dipole cross section near $r \sim 0$, which decreases faster than $r^2$.

The key question here is how to treat the coupling in Eq. (1.164). While the approach of Ref. [141] has its benefits, if one follows the derivation of the dipole factorization in Sec. 1.6, it is still natural to have a coupling constant encoded in the dipole cross section. Considering the small-$r$ limit of the GBW model

$$\sigma_{\text{GBW}}(x, r)\big|_{r \ll Q_s} \approx r^2 Q_s^2 / 4, \tag{3.31}$$

in comparison to *cf.* Eq. (1.166)

$$\sigma_{\text{dipole}}(x, r)\big|_{r \ll Q_s} \approx \frac{r^2 \pi^2 \alpha_s(\mu^2) x g(x, \mu^2)}{3}, \tag{3.32}$$

suggests that the GBW model is an approximation in which $\alpha_s(\mu^2)$ and $xg(x, \mu^2)$ are independent of $r$ [70]. For this reason, in order to account for the running coupling in Eq. (3.27), we assume that $\alpha_s$ in Eq. (1.165) is constant for the GBW model, and thus explicitly multiply by the running coupling

$$\alpha_s(\mu^2) \mathcal{F}^{\text{dipole}}_{\text{BGW}}(x, k_T^2) \to \alpha_s(\mu) \frac{\alpha_s \mathcal{F}^{\text{dipole}}_{\text{BGW}}(x, k_T^2)}{0.2}, \tag{3.33}$$

where

$$\alpha_s(\mu^2) = \frac{1}{\frac{11C_A - 2n_f}{12\pi} \log\left(\frac{\mu^2}{\Lambda^2_{\text{QCD}}}\right)}, \tag{3.34}$$

and $\Lambda^2_{\text{QCD}} = 0.09\ \text{GeV}^2$. The factor 0.2 is an arbitrary normalization and, since its

| $n$ | Levin | Sum |
|---|---|---|
| 9 | $-5.751 \times 10^{-9}$ | $-4.998 \times 10^{-4}$ |
| 12 | $-1.5891 \times 10^{-9}$ | $2.5567 \times 10^{-4}$ |
| 15 | $-3.803 \times 10^{-11}$ | $-1.5069 \times 10^{-4}$ |
| 18 | $6.639 \times 10^{-13}$ | $9.743 \times 10^{-5}$ |
| 21 | $2.6728 \times 10^{-13}$ | $-6.722 \times 10^{-5}$ |
| 24 | $2.6744 \times 10^{-13}$ | $4.866 \times 10^{-5}$ |
| 27 | $2.6744 \times 10^{-13}$ | $-3.655 \times 10^{-5}$ |

Table 3.3: Computing $\int \frac{dr}{r} J_0(rk)(1-e^{-r^2})$ with $k = 10$ adding up to $n$ th term. Levin-accelerated case reaches the true value of $\sim 2.674 \times 10^{-13}$ far more quickly, and shows superior stability.

effect is absorbed by $\sigma_0$, it bears no importance. (For a more detailed analysis of the dipole gluon density from the BGK model see Ref. [141]) While there is some ambiguity on what the argument of $\alpha_s(\mu^2)$ should be, we follow Ref. [74] and use

$$\mu^2 = k_T^2 + \kappa_t'^2 + m_f^2 + \mu_0^2, \tag{3.35}$$

where $\mu_0^2 = 4\ \mathrm{GeV}^2$ is added in order to freeze the coupling at low scales. This value is chosen from the results of preliminary runs, which turned out to work well. Fitting of this parameter is not desirable due to strong correlations with the other parameters, particularly with $\sigma_0$.

Unlike in the dipole-factorization formula, Eq. (1.163), the argument of $\mathcal{F}^{\mathrm{dipole}}$ in Eqs. (1.153) and (1.154) is $x/z$, not $x$, therefore, the gluon density enters the region of large-$x$, where the model is not expected to be valid. Particularly, the assumption that the parton density is dominated by gluons is no longer true. While one may multiply the gluon density by a factor $(1-x/z)^\alpha$ in order to suppress the threshold region [139], from a preliminary fit, it was observed that the effect is rather limited and for the case of the BGK model, the fit quality was deteriorated.

### 3.3.2 Computation of gluon densities

In the evaluation Eq. (1.167), convergence of the integral may be slow due to high oscillation for large $k$. For such integration, one can employ a method summarized in Ref. [140]. Essentially, the integration is carried out between, anti-nodes of $J_0(rk)$. Then, the total integral is written in the form of infinite sum

$$I = \sum_{i=1}^{\infty} \int_{a_i}^{a_{i+1}} \frac{dr}{r} J_0(rk)\sigma_{\mathrm{dipole}}(x,r), \tag{3.36}$$

where we use $a_i = \frac{\pi}{k}(i+1/4)$. This sum can be accelerated with series transformation described in Ref. [143–145]. Remarkable power of Levin's transformation is shown in Tab. 3.3. This trick is also useful in the computation of dipole gluon density. While there are several methods for numerical integration, we chose to implement the method of Clenshaw and Curtis (CC) [146], which is tightly related to

the Chebyshev approximation. The idea essentially is to expand the expression in the basis of Chebyshev polynomials, thus reducing the integral to the integration of Chebyshev polynomials. In general, quadrature formulae are written in the form

$$\int_b^a dx f(x) = \sum_{i=0}^{n} c_i f(x_i) + E, \tag{3.37}$$

where the coefficients $c_i$ are specific to the quadrature formula and $E$ is the remainder. Unlike the Gauss quadrature formula, in this method of CC, a set of points $x_i$ used for the $n$-point quadrature can be reused for the $2n$-point quadrature. An estimate of an error, $E$, can be obtained by comparing the $n$-point and $2n$-point results, for which $n$-ponit result can be trivially obtained in the CC formula, while the Gauss formula requires additional evaluation of $f(x)$ at $n$ points. Using Eq. (3.36) with the CC quadrature, one can numerically compute gluon densities efficiently.

### 3.3.3 Fits with exact kinematics

We have fitted the GBW and BGK models to the $F_2$ data from HERA [134] with the same setup as in the previous fit see Sec.3.2:

$$\begin{aligned} &0.045 \leq Q^2 \leq 650 \text{ GeV}^2, \qquad x \leq 0.01 \\ &\text{number of data points} = 378, \\ &m_u, m_d, m_s = m_l = 0 \text{ GeV}, \quad m_c = 1.3 \text{ GeV}, \quad m_b = 4.6 \text{ GeV}, \end{aligned} \tag{3.38}$$

and the modified star-prescription (3.25) is used for the BGK model (3.6).

A new numerical program was written with help of CERNLIB (DPSIPG) [147], GSL [148], CUBA [149] and ROOT [150] libraries to evaluate $F_2$. As discussed earlier in Sec. 3.2, the $c$ and $b$ flavours were taken into account with the mass 1.3 and 4.6 GeV, respectively, and the light quarks were set to be massless. The fitting was performed using MnMigrad and MnSimplex of ROOT::Minuit2 [151, 152]. The following cases were studied:

- GBW model with the fixed coupling in $k_T$-factorization ($k_T$-GBW),
- GBW model with the running coupling in $k_T$-factorization (rc-$k_T$-GBW),
- BGK model in $k_T$-factorization ($k_T$-BGK),

and, the following results from Ref. [133] were used as a reference:

- GBW model with massless light quarks in the dipole-factorization ($r$-GBW),
- GBW model with massive light quarks in the dipole-factorizations ($r$-GBW-massive),
- BGK model in the dipole-factorization ($r$-BGK).

| - | $\sigma_0$ [mb] | $x_0\,(10^{-4})$ | $\lambda$ | $\chi^2$/dof |
|---|---|---|---|---|
| $r$-GBW | 1.907e+01 | 2.582e+00 | 3.219e-01 | 4.438e+00 |
| $r$-GBW-massive | 2.384e+01 | 1.117e+00 | 3.082e-01 | 5.274e+00 |
| $k_T$-GBW | 3.344e+01 | 1.333e+00 | 3.258e-01 | 4.396e+00 |
| rc-$k_T$-GBW | 1.520e+01 | 2.648e+00 | 3.211e-01 | 2.447e+00 |

| - | $\sigma_0$ [mb] | $A_g$ | $\lambda_g$ | $C$ | $\mu_0^2$ [GeV$^2$] | $\chi^2$/dof |
|---|---|---|---|---|---|---|
| $r$-BGK | 2.326e+01 | 1.181e+00 | 8.317e-02 | 3.294e-01 | 1.873e+00 | 1.556e+00 |
| $k_T$-BGK | 3.470e+01 | 1.048e+00 | 2.205e-01 | 2.391e-01 | 9.954e-01 | 1.527e+00 |

Table 3.4: Fit parameters of respective models. The parameters of the dipole-factorization cases are taken from Ref. [133].

The results of the fits are summarized in Tab. 3.4. The fit quality of $k_T$-GBW is almost unchanged from $r$-GBW, while rc-$k_T$-GBW shows remarkable improvement, almost halving the $\chi^2$ value. It was pointed out in Ref. [57, 119, 120] that in the BK evolution, the running coupling corrections have considerable effects. Another notable point is that, except for the normalization $\sigma_0$, the parameters are very similar, particularly those of rc-$k_T$-GBW are almost identical to those of $r$-GBW. This can be seen also in Fig. 3.7.

Let us analyse also the difference in $\sigma_0$. Recalling that the difference between the $k_T$-factorization formula and the dipole-factorization formula is in $x/z$, where this enters the GBW formalism via (3.3), it is easy to see that, as $x$ grows, the dipole cross section gets suppressed (Keeping in mind the suppression by the photon wave function in the large-$r$ region.). Such effect was discussed previously in Ref. [121] in the context of the BK equation. In fact, this suppression is the motivation given in Ref. [73] for such modification of $x$, so that in the small-$Q^2$ limit, the total cross section remains finite. Since

$$\left(1+\frac{4m_f^2}{Q^2}\right) \leq \left(1+\frac{k_T^2}{Q^2}+\frac{\kappa_t'^2+m_f^2}{\beta(1-\beta)Q^2}\right), \tag{3.39}$$

the $k_T$-factorization case receives more suppression. Consequently, the normalization factor $\sigma_0$ rises to compensate for it. Thus, one would expect that the massive light quarks partially simulate the effect of $x/z$. It is therefore interesting to see that the parameters of $k_T$-GBW are closer to those of $r$-GBW-massive than to the parameters of $r$-GBW. However, it seems that there is a compensating factor in rc-$k_T$-GBW.

While the GBW model remains almost unaffected, the BGK model shows slightly bigger change. The difference is more prominent in the small-$x$ region (Fig. 3.7), particularly noticeable in the second peak of the gluon density. The change is clearly visible in the saturation scale of Fig. 3.7. The resulting $F_2$ of respective models is plotted in Figs. 3.8 and 3.9. While the $r$-GBW and $k_T$-GBW show little difference, rc-$k_T$-GBW exhibi better fit quality in the high-$Q^2$ region. This is clearly visible in the histogram at the bottom. As for the BGK model, the difference is too small to be seen in the top plots. However, the bottom histogram reveals some differences. While the small-$Q^2$ region is somewhat improved, as a whole, the changes cancel out.

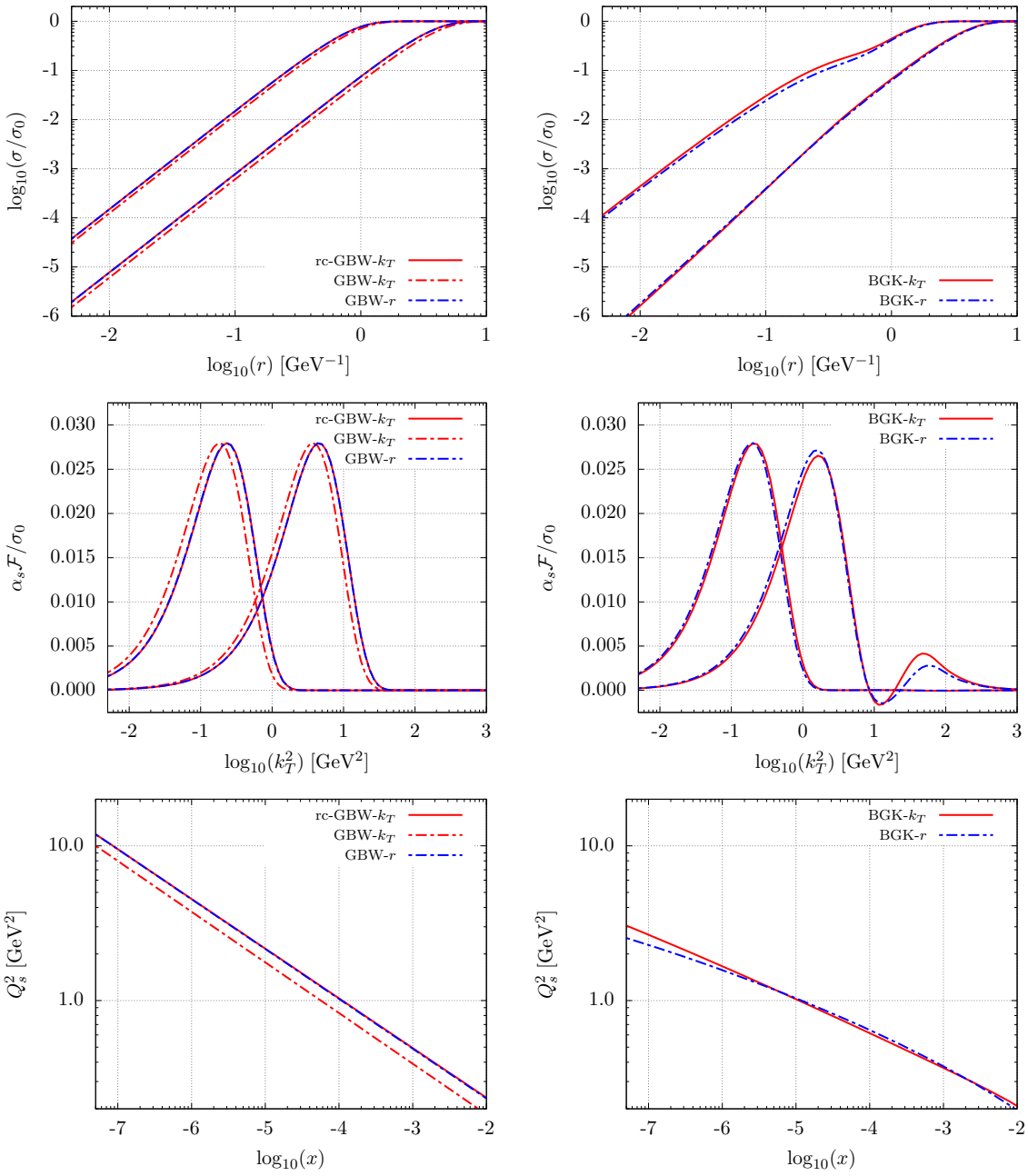


Figure 3.7: The dipole cross section, the dipole gluon density at $x = 10^{-2},\ 10^{-6}$, and the saturation scale for the GBW (left) and the BGK (right) models. Note that the dipole cross section and the gluon density are normalized by $\sigma_0^{-1}$.

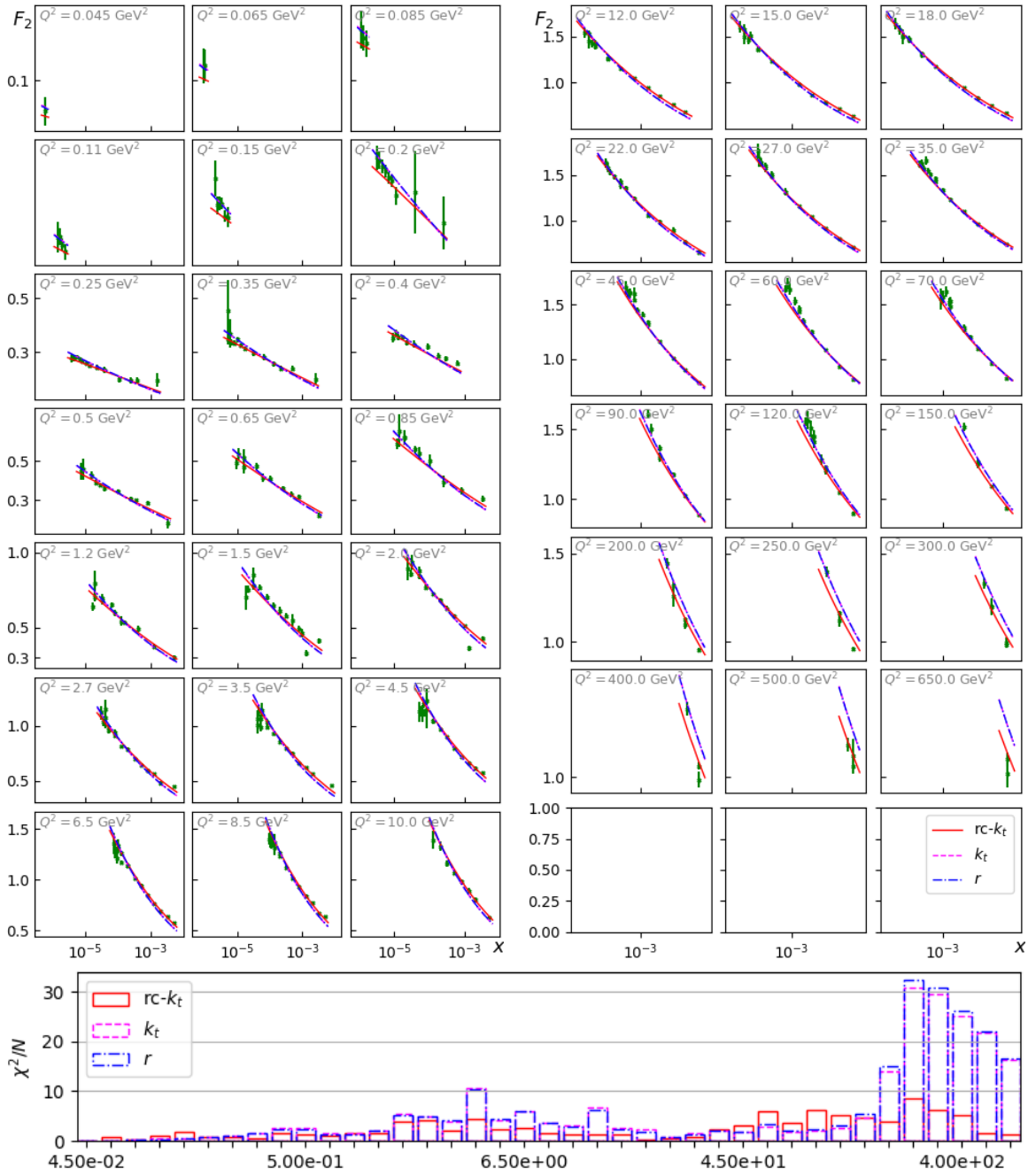


Figure 3.8: Comparison of GBW $F_2$ with HERA data. The histogram shows the $\chi^2$ value per data point in each frame. Improvement by the running coupling ($k_T$ run) is clearly visible in the high-$Q^2$region, while the new fit ($k_T$) gives only marginal improvement .

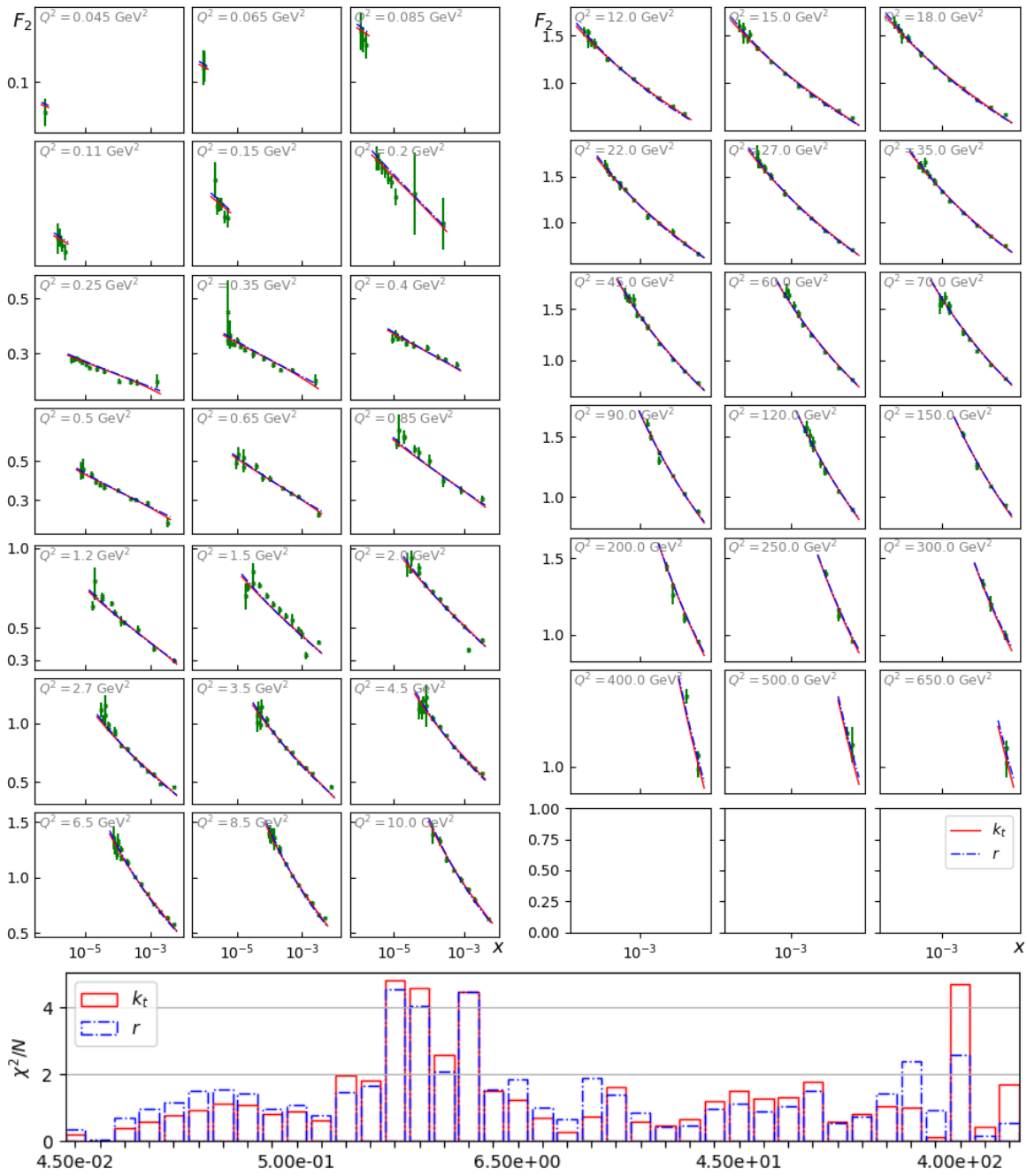


Figure 3.9: Comparison of BGK $F_2$ with HERA data. The histogram shows the $\chi^2$ value per data point in each frame. While the overall fit quality remain similar, the fit quality in each frame change noticeably. Particularly, the $k_T$-formula case ($k_T$) gives a better fit in the small-$Q^2$ region.

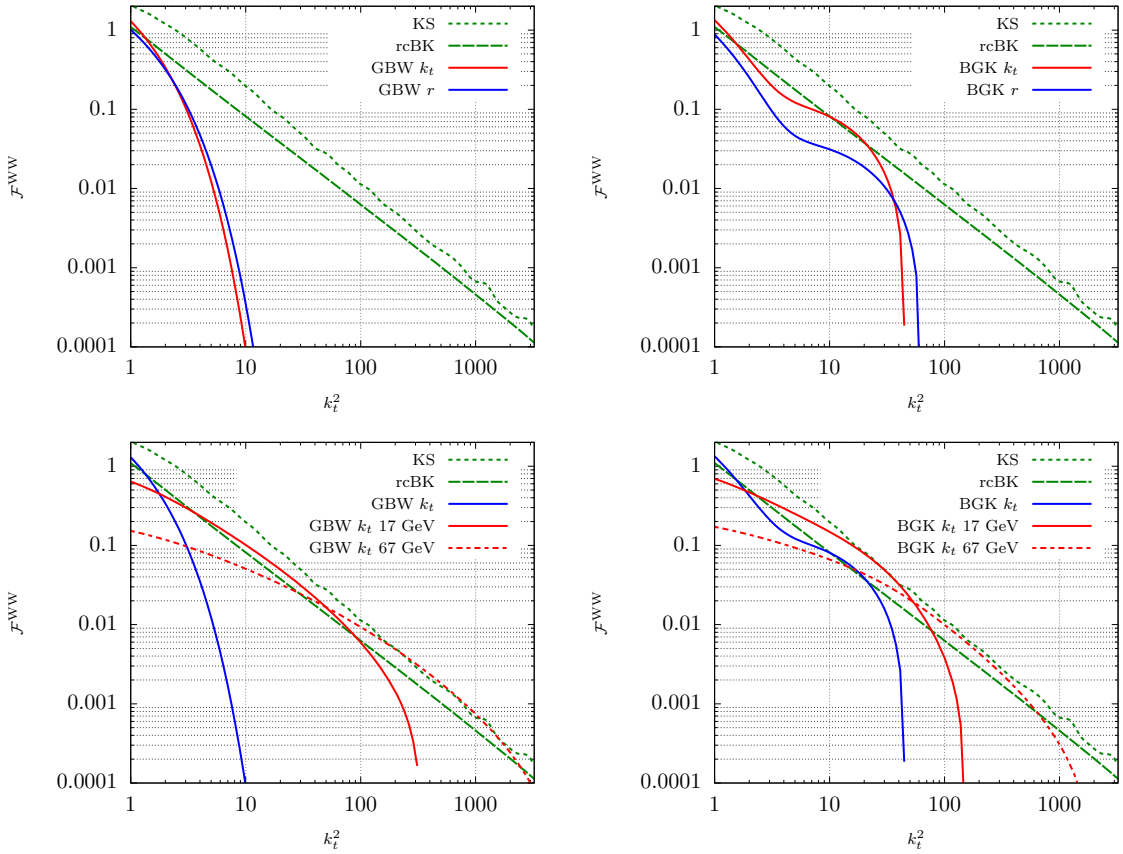


Figure 3.10: Weizsäcker-Williams gluon density at $x = 10^{-3}$. Top row: comparison of the dipole-factorization fit and $k_T$-factorization fit results. Bottom row: comparison of the respective models with and without the Sudakov factor at $\mu = 17,\ 67$ GeV.The green dotted line is the KS gluon [153], and the green dashed line is the rcBK gluon [154].

## 3.4 Dijet production at EIC

The $F_2$ structure function is an inclusive object and it is only moderately sensitive to the shape of the gluon density. To probe $k_T$-dependence of the gluon better, we shall now apply the dipole cross section obtained above to the electron-dijet correlation at the Electron-Ion Collider (EIC), following closely the method of Ref. [153].

We consider dijet production in DIS

$$e + p \to e + J_1 + J_2 + X\,. \tag{3.40}$$

At leading order, in the small-$x$ limit, this process is dominated by the $q\bar{q}$ jets [80]. It is therefore closely related to the dipole picture we discussed earlier, see Fig. 1.8. In the Breit frame, where the photon momentum is given by $q = (0, 0, 0, Q)$, at leading order, the jet momentum imbalance $p_T \equiv |p_{1T} + p_{2T}|$, where $p_{1T}$ and $p_{2T}$ are transverse momenta of the jets, equals the gluon transverse momentum $k_T$. This makes dijets an interesting process. For the region where $p_T \ll P_T \sim p_{1T}, p_{2T}$, one may use power counting to take leading order in $p_T/P_T$, which leads to the transverse-momentum-dependent (TMD) factorization, *cf.* Sec.1.8.

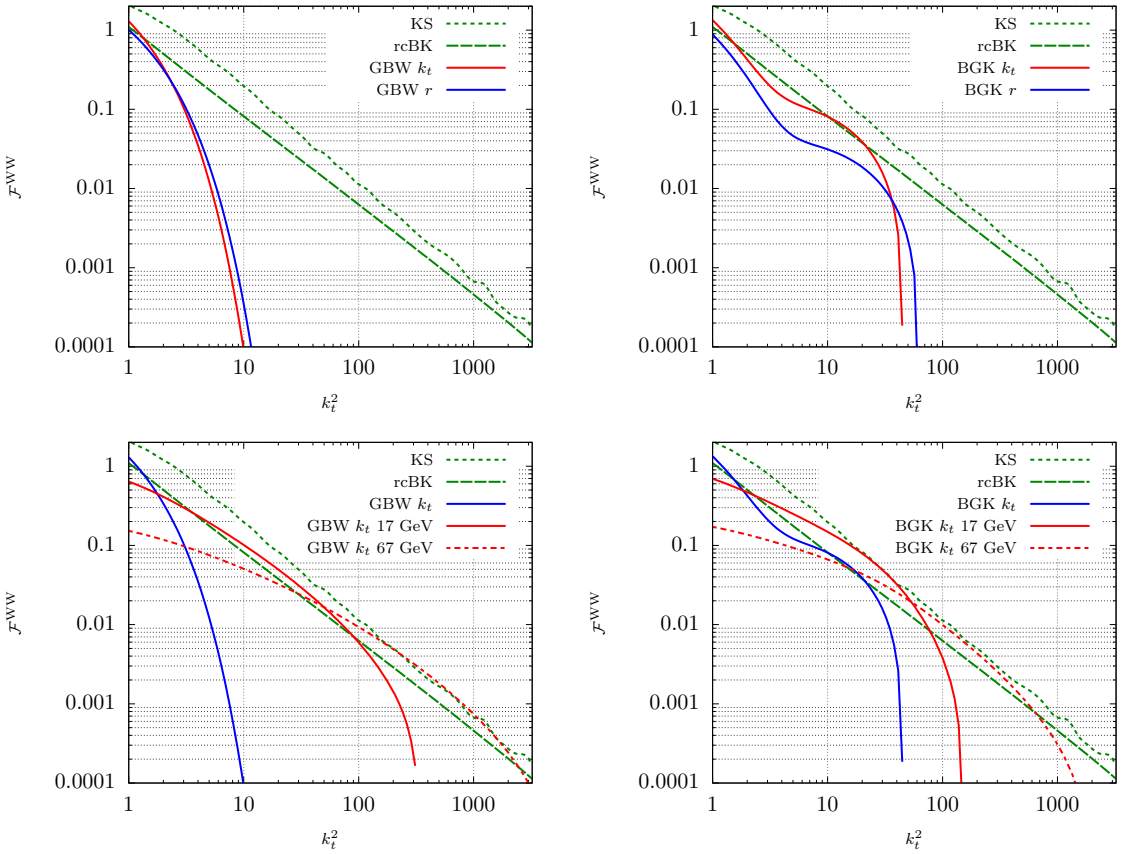


Figure 3.11: Weizsäcker-Williams gluon density at $x = 10^{-3}$. Top row: comparison of the dipole factorization fit and $k_T$-factorization fit results. Bottom row: comparison of the respective models with and without the Sudakov factor, at $\mu = 17,\ 67\mathrm{GeV}$.The green dotted line is the KS gluon [153], and the green dashed line is the rcBK gluon [154].

In the large-$N_c$ limit of the TMD factorization, there are two types of gluon densities, namely the dipole gluon density and the Weizsäcker-Williams (WW) gluon density [79, 80, 83, 84]. It was shown in Ref. [80] that the dijet process in DIS can directly probe the WW gluon, $\mathcal{F}^{\mathrm{WW}}(x, k^2)$, where the differential cross section factorizes as

$$\frac{d\sigma^{\gamma^* p \to q\bar{q}X}}{d\mathrm{P.S.}} = \mathcal{F}^{\mathrm{WW}}(x, k_T^2) H_{\gamma^* g^* \to q\bar{q}}, \tag{3.41}$$

with the hard function $H_{\gamma^* g^* \to q\bar{q}}$ describing interactions of an off-shell photon with an off-shell gluon producing a $q\bar{q}$ pair. $\mathcal{F}^{\mathrm{WW}}(x, k^2)$ has an interpretation of a number density of gluons inside a proton, while $\mathcal{F}^{\mathrm{dipole}}(x, k_T^2)$ does not have such an interpretation [79, 80, 84].

We carried out our study in the framework of the *Improved Transverse-Momentum-Dependent* (ITMD) factorization [81, 83, 90] introduced in Sec. 1.8. This framework is implemented in the program KaTie [155], which is used to compute the cross sections. The ITMD factorization is a generalization of the TMD factorization where the momentum imbalance in the latter is restricted to be small [81, 83]. That is to say, ITMD resums $(Q_s/k_T)^n$ and $(k_T/P_T)^n$ [81, 83], thus extends the region of applicability up to $k_T \sim P_T$. The difference of Eq. (3.41) from the regular TMD is that the

hard function has an off-shell gluon $g^*$, thus rendering the $k_T$ dependence in the hard function as well [81].

For the region where the TMD factorization is applicable, $Q_s \sim k_T \ll P_T \sim Q$, one needs to resum the large Sudakov logarithms $\log(k_T/Q)$, as well as $\log(1/x)$ [80]. As with the previous case of the dipole gluon density, it was shown in Refs. [88,129,156] that consistent resummation of such logarithms is possible owing to the separation of the corresponding regions. Resummation of the Sudakov logarithms is achieved by the formula

$$\mathcal{F}^{\mathrm{WW}}(x,k^2,\mu^2) = \frac{C_F}{2\pi^3\alpha_s}\int_0^\infty \frac{dr}{r} J_0(rk) e^{-S(r,\mu^2)} \sigma_{\text{dipole Adj.}}(x,r), \tag{3.42}$$

where we use the Sudakov form factor [88, 156]

$$S(r,\mu^2) = \frac{\alpha_s N_c}{4\pi}\ln^2\left(\frac{\mu^2 r^2}{4e^{-2\gamma_E}}\right), \tag{3.43}$$

in which the coupling constant was set to $\alpha_s = 0.2$.

Following Ref. [153], we study the azimuthal correlations of jets and the final state electron in DIS, as this observable is sensitive to soft emissions and saturation effects. Here, only the proton case is considered, because we focus on the Sudakov effects and the exact gluon kinematics. We use kinematical cuts suggested in Ref. [153]

$$\begin{aligned} E_e = 15\mathrm{GeV}, \qquad & E_p = 135\mathrm{GeV}, \qquad & Q^2 > 1\mathrm{GeV}^2, \\ 0.1 < \nu < 0.85, \qquad & \Delta R_{\mathrm{Breit}} < 1, \qquad & p_{1,2\,T}^{\mathrm{Breit}} > 3\mathrm{GeV}, \\ & -4 < y_{1,2\,\mathrm{lab}} < -1. \end{aligned}$$

Grids of the Weizsäcker-Williams gluon density were produced by evaluating Eqs. (1.167) and (3.42). The gluon density at $x = 10^{-3}$ is plotted in Fig. 3.11 with the hard-scale-independent Kutak-Sapeta (KS) gluon [135, 153, 157] and the running-coupling BK (rcBK) gluon density [120, 154, 158]. Clearly, the GBW and BGK models falls much more quickly than the KS and rcBK gluon densities. In general, expected behaviour in the large-$k_T$ region is $\sim k_T^{-2}$ [79, 80], while $\sigma_{\mathrm{GBW}}$ behaves like $\sim e^{-k_T^2}$. As in Ref. [153], the Sudakov factor enhances the small-$k_T$ region and suppresses the large-$k_T$ region. In other words, it broadens the gluon distribution. In comparison to the result of Ref. [153], the effect of broadening by the Sudakov factor is significantly more pronounced in the case of the GBW and BGK models. The hard-scale-dependent GBW and BGK models, as a consequence, become closer to the KS and rcBK gluons, *cf.* Fig. 2 of Ref. [153].

Figs. 3.12 and 3.13 show electron-jets azimuthal correlation in the Breit and in the Lab frame respectively. In the top row of Fig. 3.12, we see better agreements of out results with the KS and rcBK for the new $k_T$-factorization fits for both the GBW and BGK models. However, the overall normalization of the gluon density depends on the coupling $\alpha_s$, which we assumed to be 0.2. Nevertheless, Fig. 3.12 shows clearly the effect of the parameter $\sigma_0$. In the middle and the bottom row, we demonstrate the effects of the Sudakov form factor, which qualitatively agrees with that of Ref. [153]

by lowering the cross section.

Fig. 3.13 shows the electron-jets correlation in the Lab frame. Here, the difference between KS and GBW and BGK is more prominent, while rcBK shows similar pattern to the GBW and BGK models. The effects of the Sudakov factor are similar to those in Ref. [153] at relatively high $\Delta\phi$, while at smaller $\Delta\phi$ region, the effects are reversed (*i.e.* the cross sections were slightly lowered in Ref. [153], while here, they are significantly increased).

Finally, Fig. 3.14 shows the jet-jet correlations in the Breit frame. Again, the GBW and BGK models exhibit considerable deviation from the KS gluon. The difference from the previous plot is the disagreement of the GBW/BGK models and the rcBK in the small-$\Delta\phi$ region. Similarly to the previous plots, the Sudakov factor affects the models somewhat differently from the KS gluon in Ref. [153]. The effect enhances the cross section considerably in the small-$\Delta\phi$ region, making it closer to the KS gluon result.

The results shown in Figs. 3.13 and 3.14 are natural, as back-to-back configuration in the respective observable corresponds to the small-$k_T$ region of gluon densities, and, as it can be seen clearly in Fig. 3.11, the GBW and BGK gluons do not fare well in the large-$k_T$ region. That is to say that the enhancement in the small-$\Delta\phi$ region is a direct consequence of the broadening by the Sudakov factor.

A part of success of the GBW model is attributed to the description of diffractive DIS [75, 127]. However it was pointed out [85] that their formula

$$\sigma_{\text{Adj.}} = \frac{C_A}{C_F}\sigma_{\text{dipole}}, \tag{3.44}$$

saturates to a higher value $\frac{9}{4}\sigma_0$ than Eq. (1.168), thus it is expected to overshoot the data. Therefore, while Refs. [75, 127] described the data well, if one takes the correct formulation (1.168) into account, the result should decrease. The present fit has demonstrated that the normalization $\sigma_0$ increases if the exact kinematics is considered, thus our result is encouraging in this respect.

## 3.5 Summary of the chapter

In the first part of this chapter, we have discussed specifications of the models of dipole cross section. In particular, the detailed overview of the Golec-Biernat–Wüsthoff (GBW) model and its DGLAP improved version, the Bartels–Golec-Biernat–Kowalski (BGK) model was given.

In the second part of the chapter, we have investigated the effects of the Sudakov form factor, which resums two disparate scales, which in our case were $1/r \sim k_T$ and $Q$. In Ref. [88], consistent resummation of two large logarithms $\ln(rQ)$ and $\ln(x)$ was achieved for the dipole cross section. Using their results, we extended the dipole factorization formula by incorporating the Sudakov form factor (3.16). The resulting quality of fits to the HERA data improves, particularly in the region of higher $Q^2$ and more moderate $x$.

In the third part of the chapter, we have investigated effects of exact gluon kinemat-

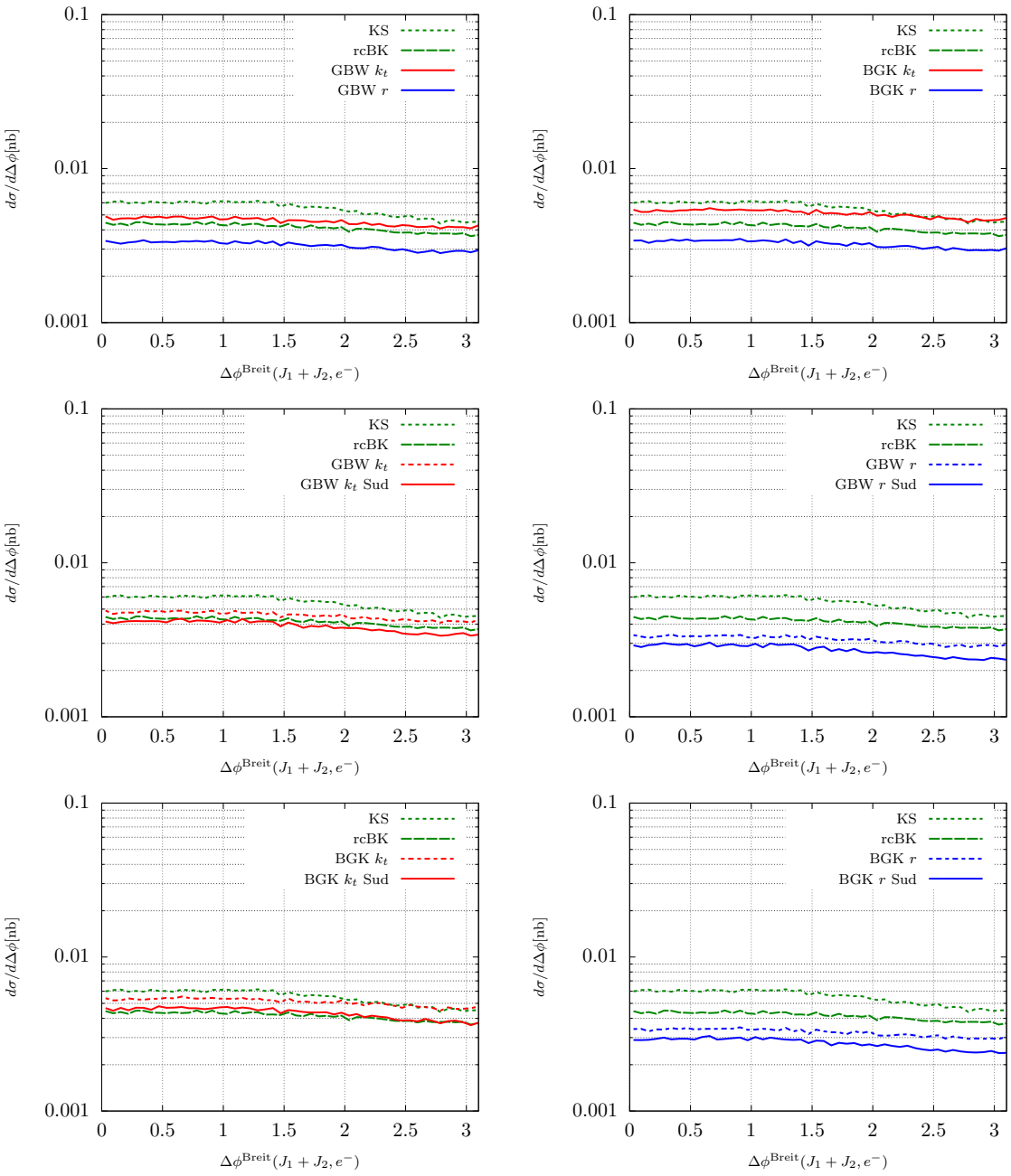


Figure 3.12: Azimuthal correlation of the jets and the scattered electron in the Breit frame. Top: Comparison of dipole factorization fit and $k_T$-factorization fit. Middle & Bottom: Effect of the Sudakov form factor. The green dotted line is the KS gluon [153] and the green dashed line is the rcBK gluon [154].

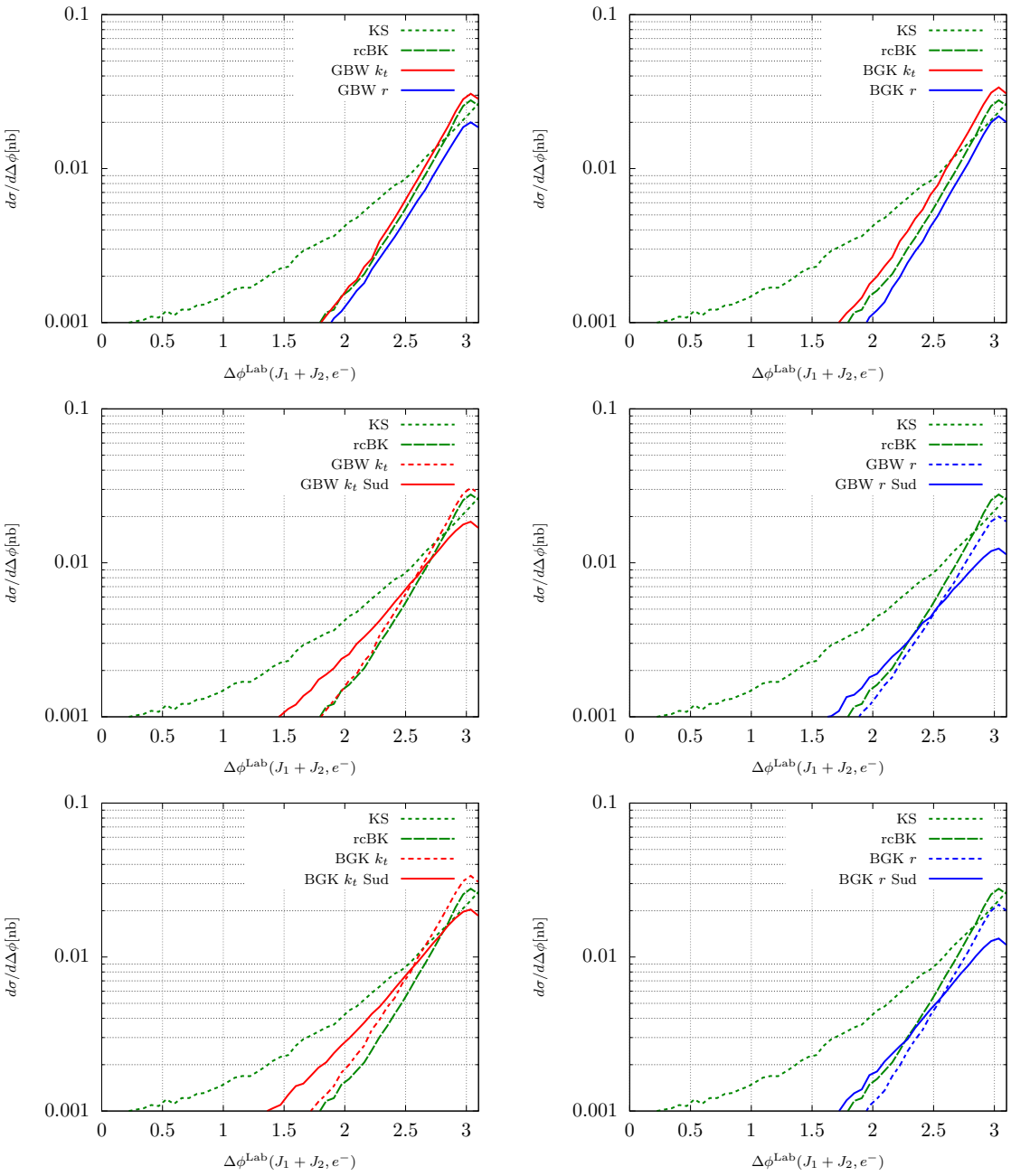


Figure 3.13: Azimuthal correlation of the jets and the scattered electron in the Lab frame. Top: Comparison of dipole factorization fit and $k_T$-factorization fit. Middle & Bottom: Effect of the Sudakov form factor. The green dotted line is the KS gluon [153] and the green dashed line is the rcBK gluon [154].

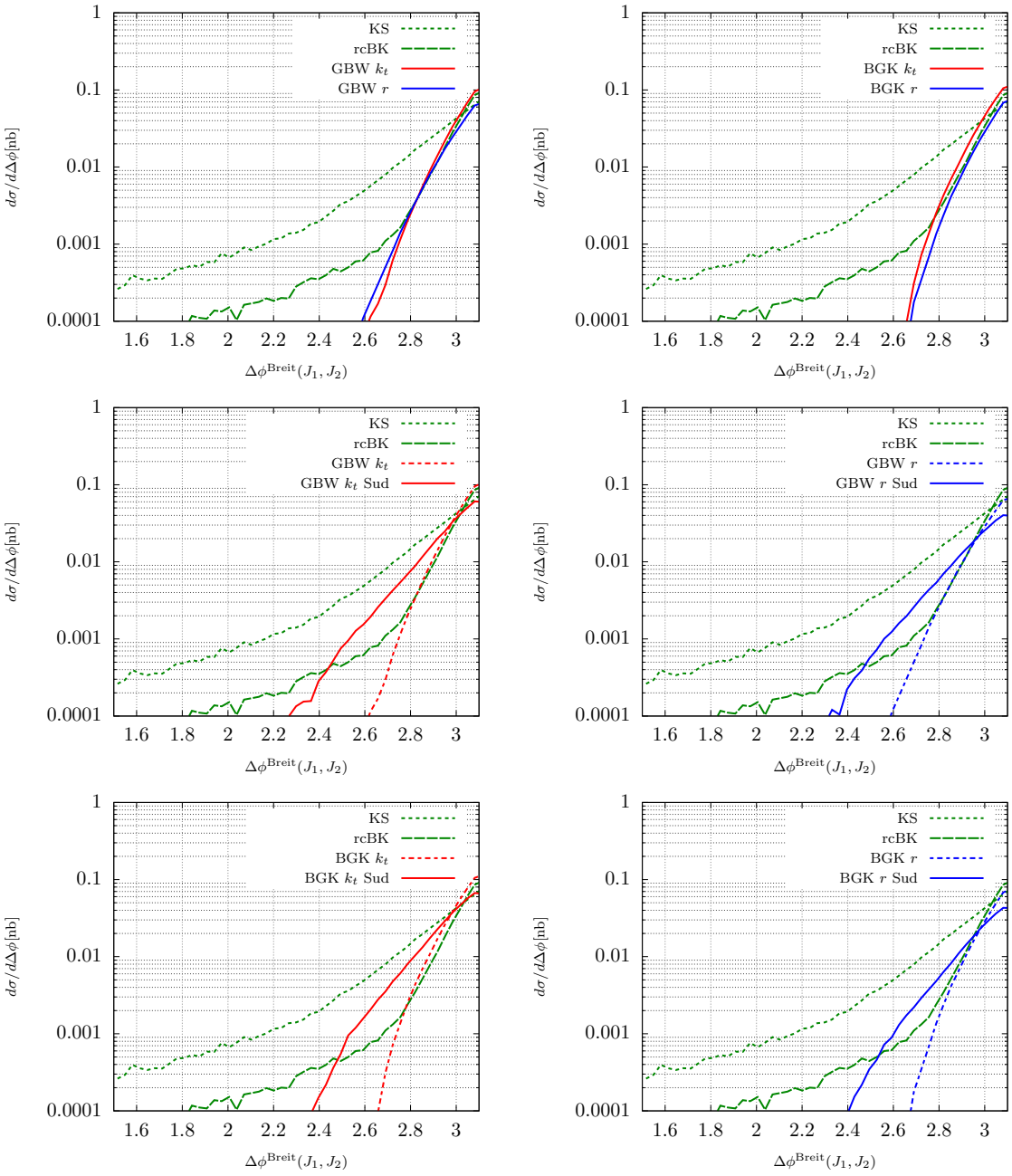


Figure 3.14: Azimuthal correlation of the jets in the Breit frame. Top: Comparison of dipole factorization fit and $k_T$-factorization fit. Middle & Bottom: Effect of the Sudakov form factor. The green dotted line is the KS gluon [153] and the green dashed line is the rcBK gluon [154].

ics in the $k_T$-factorization formula (3.27), which is partially lost in its position-space counterpart: the dipole factorization formula (1.163). The explicit re-derivation of the dipole factorization formula spelled out the differences between the two formalisms and also clarified the origin of the light-quark mass present in the original models (3.3). The GBW and BGK models were fitted with exact gluon kinematics to the same HERA data as in Sec. 3.2 but, this time, in the $k_T$-factorization formula (3.27). Remarkably, the fit qualities were little affected, yet the fit showed a large increase in the parameter controlling overall normalization, $\sigma_0$. The fit for the GBW model also showed a considerable improvement when the running coupling was implicitly used in the formula. At the end of the chapter, we have investigated implications of the newly fitted models, with Sudakov form factor, on the prediction of dijet production at EIC. The results were compared with Ref. [153] and have shown qualitative agreements.

# Summary

We have discussed theoretical and phenomenological aspects of the proton structure in two distinct regimes. In the first one, where the Bjorken scaling variable, $x$, is moderate but the hard-scale $Q$ is large, one resums the large logarithms, $\ln(Q^2)$. In addition, when the transverse momentum, $q_T$, of the system, such as that of the vector boson in the DY process, is small, cross sections are obtained by the convolution of the beam functions and appropriate partonic cross sections, in which also the logarithms of the type $\ln(q_T/Q)$ have to be resummed. In the second regime, where $x$ is small, while $Q$ is moderate, the resummation of $\ln(x)$ becomes important. In this region, gluons dominate as the constituents of the proton. As one goes further in the low-$x$ region, the gluon density is expected to be saturated. The description of the DIS processes in the small-$x$ region is commonly performed in the dipole formalism, in which the dipole cross section describes the scattering of quark–anti-quark pair on the gluon-rich proton.

In Ch. 2, we have presented a new scheme for the calculation of the beam functions. The main objective of the scheme is to obtain beam functions as Laurent expansions around the poles of regulators, $\epsilon$ and $\alpha$. To this end, one needs all singularities of the integrands to be factorized as monomials. At N$^3$LO, due to the increased number of real radiations, complexity of the divergences increases considerably. The complex structures can be treated with the use of a technique, called sector decomposition, which dissects the phase-space and deforms each sector such that the divergences can be factorized as monomials. However, it is impractical, if not impossible, to achieve optimal parametrization of momenta for the sector decomposition due to large number of divergent limits. In order to improve the situation, we have introduced another technique, involving selector functions. The selector functions effectively decompose the phase-space without deforming it. In each sector, the corresponding selector function allows only subsets of the divergences to be active and this helps to achieve optimal parametrization of the momenta. We have successfully demonstrated the effectiveness of our approach at N$^3$LO by explicitly computing the pole part of the beam function.

In Ch. 3, we have investigated the effects of the Sudakov form factor and exact gluon kinematics on the GBW and BGK models of the dipole cross section. In the former case, we have shown that inclusion of the Sudakov form factor improves description of the HERA data, expanding the region of applicability for a wider range of $Q^2$ and $x$. In the latter part of the chapter, we have investigated the effects of exact gluon kinematics by fitting the above two models directly in momentum space using the $k_T$-factorization formula of the $F_2$ structure function. It was demonstrated that in the derivation of the dipole factorization formula from the $k_T$-factorization formula,

the exact form of gluon kinematics is partially lost. Additionally, the effects of the running coupling become unclear in the dipole formalism. The derivation also clarified the origin of the use of massive light quarks in the original model. While the differences in fit quality were moderate, we have clearly demonstrated the effects on the overall normalization of the models, and its connection to the use of the massive light quarks. At the end of the chapter, we have investigated implication of the newly obtained fits to the predictions of dijets processes in DIS at EIC. We have also shown the effects of the Sudakov form factor on the prediction, which agreed with the result of Ref. [153].

# Appendix A

# Introduction

## A.1 The bubble diagram

In the calculation of loop diagrams one typically encounters an integral of a form

$$I_{\text{bubble}} = \int_0^\infty d^{4-2\epsilon}k \frac{1}{k^2(l-k)^2}. \tag{A.1}$$

This is a scalar integral of self energy diagram with loop momentum $k$ (Fig. A.1). One of the most basic techniques to be used is the Feyman parametrization:

$$\frac{1}{D_1^{i_1} D_2^{i_2} \cdots D_N^{i_N}} = \frac{\Gamma\left(\sum_j^N i_j\right)}{\prod_j^N \Gamma(i_j)} \int_0^\infty \prod_j^N dz_j z_j^{i_j - 1} \frac{\delta\left(1 - \sum_k^N z_k\right)}{[z_1 D_1 + z_2 D_2 + \cdots + z_N D_N]^{\sum_k^N i_k}}, \tag{A.2}$$

where $D$ are the propagator denominators $(p^2 - m^2 + i\delta)$.

Thus in the current example, the integral is transformed as

$$\begin{aligned} I_{\text{bubble}} &= \int_{-\infty}^\infty d^{4-2\epsilon}k \frac{\Gamma(2)}{\Gamma^2(1)} \int dz_1 dz_2 \frac{\delta(1 - z_1 - z_2)}{\left[z_1 k^2 + z_2 (k-l)^2\right]^2} \\ &= \int_{-\infty}^\infty d^{4-2\epsilon}k \int_0^1 dz_1 \frac{1}{\left[z_1 k^2 + (1-z_1)(k-l)^2\right]^2} \\ &= \int_{-\infty}^\infty d^{4-2\epsilon}k \int_0^1 dz_1 \frac{1}{\left[k^2 + (1-z_1)(-2k \cdot l + l^2)\right]^2}, \end{aligned} \tag{A.3}$$

where the integration over the Feynman parameters are reduced to between 0 and 1 due to the delta function. In more general form, the integral can be written as

$$\begin{aligned} I = \Gamma(N) \int_0^\infty \prod_j^N dz_j \delta\left(1 - \sum_i^N z_i\right) \\ \times \int_{-\infty}^\infty d^d k \left(k^2 + 2(\sum_i^N z_i l_i) \cdot k + \sum_i^N z_i (l_i^2 - m_i^2) + i\delta\right)^{-N}. \end{aligned} \tag{A.4}$$

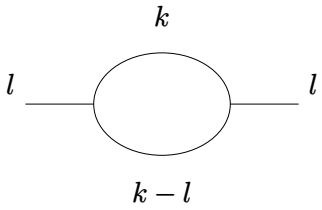


Figure A.1: Kinematic variables of self-energy loop diagrams.

By shifting $k$ by $-(\sum_i^N z_i l_i)$, one removes linear term in $k$, thus

$$I = \Gamma(N) \int_0^\infty \prod_j^N dz_j \delta\left(1 - \sum_i^N z_i\right) \times \int_{-\infty}^\infty d^d k' \left(k'^2 - (\sum_i^N z_i l_i)^2 + \sum_i^N z_i (l_i^2 - m_i^2) + i\delta\right)^{-N}. \quad \text{(A.5)}$$

With the relation $\sum_i^N z_i = 1$, one can rewrite the $k'$ integral as

$$\begin{aligned} &\int_{-\infty}^\infty d^d k' \left(k'^2 - (\sum_i^N z_i l_i)^2 + \sum_i^N z_i (l_i^2 - m_i^2) + i\delta\right)^{-N} \\ &= \int_{-\infty}^\infty d^d k' \left(k'^2 - (\sum_i^N z_i l_i)^2 + \sum_i^N \sum_j^N z_i (l_i^2 - m_i^2) z_j + i\delta\right)^{-N} \\ &= \int_{-\infty}^\infty d^d k' \left(k'^2 + \sum_i^N \sum_j^N z_i z_j ((l_i - l_j)^2 - m_i^2 - m_j^2) + i\delta\right)^{-N}. \end{aligned} \quad \text{(A.6)}$$

With $\mathcal{S}_{ij} \equiv ((l_i - l_j)^2 - m_i^2 - m_j^2)$, which is called Cayley matrix,

$$I = \Gamma(N) \int_0^\infty \prod_j^N dz_j \delta\left(1 - \sum_i^N z_i\right) \int_{-\infty}^\infty d^d k \left(k^2 + \sum_{ij} z_i z_j \mathcal{S}_{ij} + i\delta\right)^{-N}. \quad \text{(A.7)}$$

Divergences are located where

$$k_0^2 - \mathbf{k}^2 + z_i z_j \mathcal{S}_{ij} + i\delta = 0, \quad \text{(A.8)}$$

that is,

$$\begin{aligned} k_0 &= \pm\sqrt{\mathbf{k}^2 - z_i z_j \mathcal{S}_{ij} - i\delta} \\ &\simeq \pm \left[\sqrt{\mathbf{k}^2 - z_i z_j \mathcal{S}_{ij}} - \frac{1}{\sqrt{\mathbf{k}^2 - z_i z_j \mathcal{S}_{ij}}} i\delta\right]. \end{aligned} \quad \text{(A.9)}$$

Thus the poles are located at the $(+,-)$ and $(-,+)$ part of the complex plane (Fig. A.2). As it is shown schematically in Fig. A.2, one can Wick rotate without crossing over

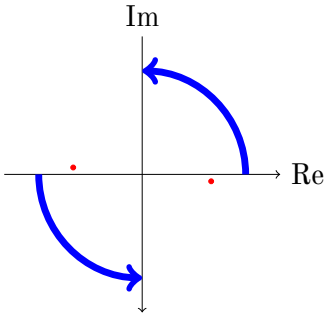


Figure A.2: Wick rotation. divergences are shown in red.

singular points such that $l_0 \to il'_0$, which effectively rotate from the Minkowski space-time to four dimensional Euclidean space, *i.e.*, $l^2 = -l'^2_0 - l_1^2 - l_2^2 - l_3^2$.

Then, the integral is transformed to

$$\begin{aligned} I = i\Gamma(N) \int_0^\infty \prod_j^N dz_j \delta\left(1 - \sum_i^N z_i\right) \\ \int_{-\infty}^\infty d^d k \left(-k^2 + \sum_{ij} z_i z_j \mathcal{S}_{ij} + i\delta\right)^{-N} \\ = \frac{i}{2}\Gamma(N) \int_0^\infty \prod_j^N dz_j \delta\left(1 - \sum_i^N z_i\right) \\ (-1)^{\frac{d-2}{2}} \int_0^\infty d|k|^2 \int d\Omega_{d-1} (|k|^2)^{\frac{d-2}{2}} \left(|k|^2 + \sum_{ij} z_i z_j \mathcal{S}_{ij} + i\delta\right)^{-N}. \end{aligned} \tag{A.10}$$

Using

$$\int d\Omega_{D-1} = \frac{2\pi^{D/2}}{\Gamma(D/2)}, \tag{A.11}$$

$$B(a,b) = \int_0^\infty \frac{z^{a-1}}{(1+z)^{a+b}} = \frac{\Gamma(a)\Gamma(b)}{\Gamma(a+b)}, \tag{A.12}$$

The $k$ integral can be performed to yield

$$\begin{aligned} I = \frac{i}{2} \frac{2\pi^{d/2}}{\Gamma(d/2)} \Gamma(N) \int_0^\infty \prod_j^N dz_j \delta\left(1 - \sum_i^N z_i\right) \\ \left(\sum_{ij} z_i z_j \mathcal{S}_{ij} + i\delta\right)^{d/2-N} (-1)^{\frac{d-2}{2}} \int_0^\infty d|k|^2 (k^2)^{\frac{d-2}{2}} \left(|k|^2 + 1\right)^{-N} \end{aligned} \tag{A.13}$$

$$= i\pi^{d/2} (-1)^{\frac{d-2}{2}} \Gamma(N - d/2) \int_0^\infty \prod_j^N dz_j \delta\left(1 - \sum_i^N z_i\right) \left(\sum_{ij} z_i z_j \mathcal{S}_{ij} + i\delta\right)^{d/2-N}. \tag{A.14}$$

Finally, using the relation

$$\int \frac{d^D k}{i\pi^{D/2}} \frac{(k^2)^A}{[k^2 - R^2]^N} = (-1)^{N+A} \frac{\Gamma(A + D/2)\Gamma\left(N - A - D/2\right)}{\Gamma(D/2)\Gamma(N)} \left(R^2\right)^{A-N+D/2}, \tag{A.15}$$

the example of the bubble diagram is evaluated to be [7]

$$\begin{aligned} I_{bubble} &= i(-1)^{\frac{d-2}{2}} \pi^{d/2} \Gamma(N - d/2) \int_0^1 dz \left(z(1-z)l^2\right)^{d/2-2} \\ &= i(-1)^{\frac{d-2}{2}} \pi^{\frac{d}{2}} \Gamma\left(2 - \frac{d}{2}\right) \left(l^2\right)^{\frac{d}{2}-2} B\left(\frac{d}{2} - 1, \frac{d}{2} - 1\right). \end{aligned} \tag{A.16}$$

Here one can now clearly see that integral vanishes when $l^2 \to 0$ and divergent for $d = 4$.

# Appendix B

# Beam function

## B.1 Re-factorization

In order to recover independence from $\alpha$ and $\nu$ one needs to consider a products of $\mathcal{B}$ and $\overline{\mathcal{B}}$. As we are interested in the perturbative expansion of the function, the explicit form can be given as

$$\begin{aligned}\mathcal{B}\overline{\mathcal{B}} = \alpha_s^0 &\left[\mathcal{B}^{(0)}(z_1)\overline{\mathcal{B}}^{(0)}(z_2)\right] \\ &+ \alpha_s^1 \left[\mathcal{B}^{(0)}(z_1)\overline{\mathcal{B}}^{(1)}(z_2) + \mathcal{B}^{(1)}(z_1)\overline{\mathcal{B}}^{(0)}(z_2)\right] \\ &+ \alpha_s^2 \left[\mathcal{B}^{(0)}(z_1)\overline{\mathcal{B}}^{(2)}(z_2) + \mathcal{B}^{(2)}(z_1)\overline{\mathcal{B}}^{(0)}(z_2) + \mathcal{B}^{(1)}(z_1)\overline{\mathcal{B}}^{(1)}(z_2)\right] \\ &+ \alpha_s^3 \Big[\mathcal{B}^{(0)}(z_1)\overline{\mathcal{B}}^{(3)}(z_2) + \mathcal{B}^{(3)}(z_1)\overline{\mathcal{B}}^{(0)}(z_2) \\ &\qquad + \mathcal{B}^{(2)}(z_1)\overline{\mathcal{B}}^{(1)}(z_2) + \mathcal{B}^{(1)}(z_1)\overline{\mathcal{B}}^{(2)}(z_2)\Big] + \mathcal{O}(\alpha_s^4),\end{aligned} \tag{B.1}$$

where

$$\mathcal{B}^{(0)}(z_1) = \delta\left(1 - z_1\right). \tag{B.2}$$

Let us introduce

$$C^{(i)} = \sum_j B^{b(j)}(z_1) B^{b(i-j)}(z_2), \tag{B.3}$$

$$\mathcal{C}^{(i)} = \lim_{\alpha\to 0} \sum_j \mathcal{B}^{(j)}(z_1)\overline{\mathcal{B}}^{(i-j)}(z_2), \tag{B.4}$$

where $B^{b(i)}(z)$ are bare, refactorized beam functions defined in Eq. (1.115). Then,

Eq. (1.115) can be written in the form,

$$\begin{aligned}\lim_{\alpha\to 0}\mathcal{B}\overline{\mathcal{B}} &= L^{\alpha_s F^{(1)}+\alpha_s^2 F^{(2)}+\alpha_s^3 F^{(3)}} \times \left[C^{(0)}+C^{(1)}\alpha_s+C^{(2)}\alpha_s^2+C^{(3)}\alpha^3\right]+\mathcal{O}(\alpha_s^4)\\ &= C^{(0)}+\alpha_s\left[C^{(1)}+C^{(0)}F^{(1)}\log(L)\right]\\ &\quad+\alpha_s^2\left[C^{(2)}+C^{(1)}F^{(1)}\log(L)+C^{(0)}F^{(2)}\log(L)+\frac{1}{2}C^{(0)}F^{(1)2}\log^2(L)\right]\\ &\quad+\alpha_s^3\left[C^{(3)}+C^{(2)}F^{(1)}\log(L)+C^{(1)}\left(F^{(2)}\log(L)+\frac{1}{2}F^{(1)2}\log^2(L)\right)\right.\\ &\quad\left.+C^{(0)}\left(F^{(3)}\log(L)+F^{(2)2}\log^2(L)+\frac{1}{6}F^{(1)3}\log^3(L)\right)\right]+\mathcal{O}(\alpha_s^4),\end{aligned} \tag{B.5}$$

where $L=\frac{x_T^2Q^2}{4e^{-2\gamma_E}}$. Since we know $C^{(0)},C^{(1)},C^{(2)},F^{(1)}$ and $F^{(2)}$, the N$^3$LO term enables one to determine $F^{(3)}$ as a coefficient of $C^{(0)}\log(L)$, and $C^{(3)}$ as a coefficient of 1 (or $L\to 1$) respectively.
Since $B^{b(0)}(z)=\delta(1-z)$, one can recursively obtain higher order functions using the relation

$$\begin{aligned}B^{b(i)}(z) &= \frac{B^{b(i)}(z)B^{b(0)}(z)+B^{b(0)}(z)B^{b(i)}(z)}{2\delta(1-z)}\\ &= \frac{1}{2\delta(1-z)}\left(C^{(i)}(z,z)-\sum_{j=1}^{i-1}B^{b(j)}(z)B^{b(i-j)}(z)\right)\\ &= \frac{1}{2\delta(1-z)}\left(\mathcal{C}^{(i)}(z,z)\big|_{L\to 1}-\sum_{j=1}^{i-1}B^{b(j)}(z)B^{b(i-j)}(z)\right).\end{aligned} \tag{B.6}$$

# Appendix C

# Dipole cross section

## C.1 Intermediate steps in the derivation of dipole factorization

Considering the terms

$$\left(\frac{1}{D_1}-\frac{1}{D_2}\right)^2 \qquad \text{and} \qquad \left(\frac{\boldsymbol{\kappa}_t}{D_1}-\frac{\boldsymbol{\kappa}_t-\mathbf{k}_t}{D_2}\right)^2 \tag{C.1}$$

of Eqs. (1.153) and (1.154). Using identities

$$iN_1\int\frac{d^2\mathbf{r}}{2\pi}\left(\frac{\mathbf{r}}{r}\right)e^{irk\cos\theta}K_1(N_1r)=-\mathbf{k}\frac{1}{k^2+N_1^2}, \tag{C.2}$$

$$i\int\frac{d^2\mathbf{r}}{2\pi}e^{irk\cos\theta}K_1(N_1r)=-\frac{1}{k^2+N_1^2}, \tag{C.3}$$

one has

$$\begin{aligned}&\left(\frac{1}{\kappa_t^2+N_1^2}-\frac{1}{(\boldsymbol{\kappa}_t-\mathbf{k}_t)^2+N_1^2}\right)\\&\qquad=-i\left(\int\frac{d^2\mathbf{r}}{2\pi}\;e^{i\boldsymbol{\kappa}_t\cdot\mathbf{r}}K_0(N_1r)-\int\frac{d^2\mathbf{r}}{2\pi}e^{i(\boldsymbol{\kappa}_t-\mathbf{k}_t)\cdot\mathbf{r}}K_0(N_1r)\right),\end{aligned} \tag{C.4}$$

$$\begin{aligned}&\left(\frac{\boldsymbol{\kappa}_t}{\kappa_t^2+N_1^2}-\frac{\boldsymbol{\kappa}_t-\mathbf{k}_t}{(\boldsymbol{\kappa}_t-\mathbf{k}_t)^2+N_1^2}\right)\\&\qquad=-iN_1\left(\int\frac{d^2\mathbf{r}}{2\pi}\left(\frac{\mathbf{r}}{r}\right)e^{i\boldsymbol{\kappa}_t\cdot\mathbf{r}}\;K_1(N_1r)-\int\frac{d^2\mathbf{r}}{2\pi}\left(\frac{\mathbf{r}}{r}\right)e^{i(\boldsymbol{\kappa}_t-\mathbf{k}_t)\cdot\mathbf{r}}K_1(N_1r)\right),\end{aligned} \tag{C.5}$$

where $N_1^2=\beta(1-\beta)Q^2+m_f^2$.

By multiplying by complex conjugate, one obtains

$$\left(\frac{1}{D_1}-\frac{1}{D_2}\right)^2=\int\frac{d^2\mathbf{r}}{2\pi}\int\frac{d^2\mathbf{r}'}{2\pi}e^{i\boldsymbol{\kappa}_t\cdot(\mathbf{r}-\mathbf{r}')}\left(1-e^{-i\mathbf{k}\cdot\mathbf{r}}\right)\left(1-e^{i\mathbf{k}\cdot\mathbf{r}'}\right)K_0(N_1r)K_0(N_1r'), \tag{C.6}$$

$$\left(\frac{\boldsymbol{\kappa}_t}{D_1}-\frac{\boldsymbol{\kappa}_t-\mathbf{k}_t}{D_2}\right)^2=N_1^2\int\frac{d^2\mathbf{r}}{2\pi}\int\frac{d^2\mathbf{r}'}{2\pi}\left(\frac{\mathbf{r}\cdot\mathbf{r}'}{rr'}\right)e^{i\boldsymbol{\kappa}_t\cdot(\mathbf{r}-\mathbf{r}')} \times\left(1-e^{-i\mathbf{k}\cdot\mathbf{r}}\right)\left(1-e^{i\mathbf{k}\cdot\mathbf{r}'}\right)K_1(N_1r)K_1(N_1r'). \tag{C.7}$$

The above can be integrated over $\boldsymbol{\kappa}_t$, which simply yields a delta function

$$\int d^2\boldsymbol{\kappa}_t e^{i\boldsymbol{\kappa}_t\cdot(\mathbf{r}-\mathbf{r}')}=(2\pi)^2\delta^2(\mathbf{r}-\mathbf{r}'). \tag{C.8}$$

Thus one obtains,

$$\int\frac{d^2\boldsymbol{\kappa}_t}{2\pi}\left(\frac{1}{D_1}-\frac{1}{D_2}\right)^2=\int\frac{d^2\mathbf{r}}{2\pi}\left|1-e^{i\mathbf{k}\cdot\mathbf{r}}\right|^2K_0^2(N_1r), \tag{C.9}$$

$$\int\frac{d^2\boldsymbol{\kappa}_t}{2\pi}\left(\frac{\boldsymbol{\kappa}_t}{D_1}-\frac{\boldsymbol{\kappa}_t-\mathbf{k}_t}{D_2}\right)^2=N_1^2\int\frac{d^2\mathbf{r}}{2\pi}\left|1-e^{i\mathbf{k}\cdot\mathbf{r}}\right|^2K_1^2(N_1r). \tag{C.10}$$

Eqs. (C.9) and (C.10) can be used for Eqs. (1.153) and (1.154), only if one assumes there is no implicit dependence on $\boldsymbol{\kappa}_t$ other than the factors considered here.

# Bibliography


[1] G. Dissertori, I. G. Knowles, and M. Schmelling, High energy experiments and theory. 2003.

[2] J. C. Collins, D. E. Soper, and G. F. Sterman, "Factorization of Hard Processes in QCD," Adv. Ser. Direct. High Energy Phys., vol. 5, pp. 1–91, 1989.

[3] J. Collins, Foundations of perturbative QCD, vol. 32. Cambridge University Press, 11 2013.

[4] R. Brock et al., "Handbook of perturbative QCD: Version 1.0," Rev. Mod. Phys., vol. 67, pp. 157–248, 1995.

[5] M. Neubert, "Renormalization Theory and Effective Field Theories," 1 2019.

[6] S. Sapeta, "QCD and Jets at Hadron Colliders," Prog. Part. Nucl. Phys., vol. 89, pp. 1–55, 2016.

[7] G. Heinrich, "Colourful loops: Introduction to quantum chromodynamics and loop calculations." 2018.

[8] D. M. Capper and G. Leibbrandt, "On a conjecture by 't Hooft and Veltman," Journal of Mathematical Physics, vol. 15, pp. 86–87, 11 1974.

[9] G. Leibbrandt, "Introduction to the Technique of Dimensional Regularization," Rev. Mod. Phys., vol. 47, p. 849, 1975.

[10] T. Kinoshita, "Mass singularities of Feynman amplitudes," J. Math. Phys., vol. 3, pp. 650–677, 1962.

[11] T. D. Lee and M. Nauenberg, "Degenerate Systems and Mass Singularities," Phys. Rev., vol. 133, pp. B1549–B1562, 1964.

[12] R. G. Roberts, The Structure of the proton: Deep inelastic scattering. Cambridge Monographs on Mathematical Physics, Cambridge University Press, 2 1994.

[13] R. K. Ellis, W. J. Stirling, and B. R. Webber, QCD and collider physics, vol. 8. Cambridge University Press, 2 2011.

[14] A. De Roeck and R. S. Thorne, "Structure Functions," Prog. Part. Nucl. Phys., vol. 66, pp. 727–781, 2011.

[15] R. L. Jaffe, "Deep Inelastic Scattering with Application to Nuclear Targets: Lectures at the 1985 Los Alamos School on Relativistic Dynamics and Quark Nuclear Physics," in Research Program at CEBAF (I): Report of the 1985 Summer Study Group, 7 1985.

[16] J. C. Collins, Renormalization: An Introduction to Renormalization, The Renormalization Group, and the Operator Product Expansion, vol. 26 of Cambridge Monographs on Mathematical Physics. Cambridge: Cambridge University Press, 1986.

[17] G. Altarelli, "The Physics of Deep Inelastic Phenomena," Riv. Nuovo Cim., vol. 4, p. 335, 1974.

[18] Y. L. Dokshitzer, "Calculation of the Structure Functions for Deep Inelastic Scattering and e+ e- Annihilation by Perturbation Theory in Quantum Chromodynamics.," Sov. Phys. JETP, vol. 46, pp. 641–653, 1977.

[19] V. N. Gribov and L. N. Lipatov, "Deep inelastic e p scattering in perturbation theory," Sov. J. Nucl. Phys., vol. 15, pp. 438–450, 1972.

[20] V. N. Gribov and L. N. Lipatov, "e+ e- pair annihilation and deep inelastic e p scattering in perturbation theory," Sov. J. Nucl. Phys., vol. 15, pp. 675–684, 1972.

[21] G. Altarelli and G. Parisi, "Asymptotic Freedom in Parton Language," Nucl. Phys. B, vol. 126, pp. 298–318, 1977.

[22] M. A. Kimber, A. D. Martin, and M. G. Ryskin, "Unintegrated parton distributions and prompt photon hadroproduction," Eur. Phys. J. C, vol. 12, pp. 655–661, 2000.

[23] D. E. Soper, "Parton distribution functions," Nucl. Phys. B Proc. Suppl., vol. 53, pp. 69–80, 1997.

[24] M. Beneke and V. A. Smirnov, "Asymptotic expansion of Feynman integrals near threshold," Nucl. Phys. B, vol. 522, pp. 321–344, 1998.

[25] V. A. Smirnov, "Applied asymptotic expansions in momenta and masses," Springer Tracts Mod. Phys., vol. 177, pp. 1–262, 2002.

[26] B. Jantzen, "Foundation and generalization of the expansion by regions," JHEP, vol. 12, p. 076, 2011.

[27] T. Becher, A. Broggio, and A. Ferroglia, Introduction to Soft-Collinear Effective Theory, vol. 896. Springer, 2015.

[28] C. W. Bauer, S. Fleming, D. Pirjol, and I. W. Stewart, "An Effective field theory for collinear and soft gluons: Heavy to light decays," Phys. Rev. D, vol. 63, p. 114020, 2001.

[29] C. W. Bauer, D. Pirjol, and I. W. Stewart, "Soft collinear factorization in effective field theory," Phys. Rev. D, vol. 65, p. 054022, 2002.

[30] M. Beneke, A. P. Chapovsky, M. Diehl, and T. Feldmann, "Soft collinear effective theory and heavy to light currents beyond leading power," Nucl. Phys. B, vol. 643, pp. 431–476, 2002.

[31] A. V. Manohar, T. Mehen, D. Pirjol, and I. W. Stewart, "Reparameterization invariance for collinear operators," Phys. Lett. B, vol. 539, pp. 59–66, 2002.

[32] T. Becher, "Soft-Collinear Effective Theory," 3 2018.

[33] T. Becher and M. Neubert, "Drell-Yan Production at Small $q_T$, Transverse Parton Distributions and the Collinear Anomaly," Eur. Phys. J. C, vol. 71, p. 1665, 2011.

[34] T. Becher and M. Neubert, "Infrared singularities of scattering amplitudes in perturbative QCD," Phys. Rev. Lett., vol. 102, p. 162001, 2009. [Erratum: Phys.Rev.Lett. 111, 199905 (2013)].

[35] T. Becher and M. Neubert, "Infrared singularities of QCD amplitudes with massive partons," Phys. Rev. D, vol. 79, p. 125004, 2009. [Erratum: Phys.Rev.D 80, 109901 (2009)].

[36] T. Becher and M. Neubert, "On the Structure of Infrared Singularities of Gauge-Theory Amplitudes," JHEP, vol. 06, p. 081, 2009. [Erratum: JHEP 11, 024 (2013)].

[37] J. C. Collins, "What exactly is a parton density?," Acta Phys. Polon. B, vol. 34, p. 3103, 2003.

[38] T. Gehrmann, T. Luebbert, and L. L. Yang, "Calculation of the transverse parton distribution functions at next-to-next-to-leading order," JHEP, vol. 06, p. 155, 2014.

[39] T. Becher and G. Bell, "Analytic Regularization in Soft-Collinear Effective Theory," Phys. Lett. B, vol. 713, pp. 41–46, 2012.

[40] J. C. Collins, D. E. Soper, and G. F. Sterman, "Transverse Momentum Distribution in Drell-Yan Pair and W and Z Boson Production," Nucl. Phys. B, vol. 250, pp. 199–224, 1985.

[41] M. Czakon and D. Heymes, "Four-dimensional formulation of the sector-improved residue subtraction scheme," Nucl. Phys. B, vol. 890, pp. 152–227, 2014.

[42] S. Catani, "The Singular behavior of QCD amplitudes at two loop order," Phys. Lett. B, vol. 427, pp. 161–171, 1998.

[43] T. Binoth and G. Heinrich, "Numerical evaluation of multiloop integrals by sector decomposition," Nucl. Phys. B, vol. 680, pp. 375–388, 2004.

[44] G. Heinrich, "Sector Decomposition," Int. J. Mod. Phys. A, vol. 23, pp. 1457–1486, 2008.

[45] S. Frixione, Z. Kunszt, and A. Signer, "Three jet cross-sections to next-to-leading order," Nucl. Phys. B, vol. 467, pp. 399–442, 1996.

[46] S. Frixione, "A General approach to jet cross-sections in QCD," Nucl. Phys. B, vol. 507, pp. 295–314, 1997.

[47] S. Frixione, "Colourful FKS subtraction," JHEP, vol. 09, p. 091, 2011.

[48] Y. V. Kovchegov and E. Levin, Quantum Chromodynamics at High Energy, vol. 33. Oxford University Press, 2013.

[49] E. Iancu, "The Color glass condensate," Nucl. Phys. A, vol. 715, pp. 219–232, 2003.

[50] K. J. Golec-Biernat, L. Motyka, and A. M. Stasto, "Diffusion into infrared and unitarization of the BFKL pomeron," Phys. Rev. D, vol. 65, p. 074037, 2002.

[51] B. L. Ioffe, V. S. Fadin, and L. N. Lipatov, Quantum chromodynamics: Perturbative and nonperturbative aspects. Cambridge Univ. Press, 2010.

[52] L. V. Gribov, E. M. Levin, and M. G. Ryskin, "Semihard Processes in QCD," Phys. Rept., vol. 100, pp. 1–150, 1983.

[53] A. H. Mueller and J.-w. Qiu, "Gluon Recombination and Shadowing at Small Values of x," Nucl. Phys. B, vol. 268, pp. 427–452, 1986.

[54] I. Balitsky, "Operator expansion for high-energy scattering," Nucl. Phys. B, vol. 463, pp. 99–160, 1996.

[55] Y. V. Kovchegov, "Small x F(2) structure function of a nucleus including multiple pomeron exchanges," Phys. Rev. D, vol. 60, p. 034008, 1999.

[56] Y. V. Kovchegov, "Introduction to the Physics of Saturation," Nucl. Phys. A, vol. 854, pp. 3–9, 2011.

[57] J. L. Albacete, N. Armesto, J. G. Milhano, C. A. Salgado, and U. A. Wiedemann, "Numerical analysis of the Balitsky-Kovchegov equation with running coupling: Dependence of the saturation scale on nuclear size and rapidity," Phys. Rev. D, vol. 71, p. 014003, 2005.

[58] S. Munier and R. B. Peschanski, "Geometric scaling as traveling waves," Phys. Rev. Lett., vol. 91, p. 232001, 2003.

[59] A. M. Stasto, K. J. Golec-Biernat, and J. Kwiecinski, "Geometric scaling for the total gamma* p cross-section in the low x region," Phys. Rev. Lett., vol. 86, pp. 596–599, 2001.

[60] L. A. Harland-Lang, A. D. Martin, P. Motylinski, and R. S. Thorne, "Parton distributions in the LHC era: MMHT 2014 PDFs," Eur. Phys. J. C, vol. 75, no. 5, p. 204, 2015.

[61] S. Bailey, T. Cridge, L. A. Harland-Lang, A. D. Martin, and R. S. Thorne, "Parton distributions from LHC, HERA, Tevatron and fixed target data: MSHT20 PDFs," Eur. Phys. J. C, vol. 81, no. 4, p. 341, 2021.

[62] M. Kimber, Unintegrated parton distributions. PhD thesis, Durham U., 2001.

[63] S. Catani, M. Ciafaloni, and F. Hautmann, "GLUON CONTRIBUTIONS TO SMALL x HEAVY FLAVOR PRODUCTION," Phys. Lett. B, vol. 242, pp. 97–102, 1990.

[64] S. Catani, M. Ciafaloni, and F. Hautmann, "High-energy factorization and small x heavy flavor production," Nucl. Phys. B, vol. 366, pp. 135–188, 1991.

[65] J. C. Collins and R. K. Ellis, "Heavy quark production in very high-energy hadron collisions," Nucl. Phys. B, vol. 360, pp. 3–30, 1991.

[66] S. Catani, M. Ciafaloni, and F. Hautmann, "High-energy factorization in QCD and minimal subtraction scheme," Phys. Lett. B, vol. 307, pp. 147–153, 1993.

[67] S. Catani and F. Hautmann, "Quark anomalous dimensions at small x," Phys. Lett. B, vol. 315, pp. 157–163, 1993.

[68] S. Catani and F. Hautmann, "High-energy factorization and small x deep inelastic scattering beyond leading order," Nucl. Phys. B, vol. 427, pp. 475–524, 1994.

[69] N. N. Nikolaev and B. G. Zakharov, "Color transparency and scaling properties of nuclear shadowing in deep inelastic scattering," Z. Phys. C, vol. 49, pp. 607–618, 1991.

[70] J. Bartels, K. J. Golec-Biernat, and H. Kowalski, "A modification of the saturation model: DGLAP evolution," Phys. Rev. D, vol. 66, p. 014001, 2002.

[71] B. Badelek, M. Krawczyk, K. Charchula, and J. Kwiecinski, "Small x physics in deep inelastic lepton hadron scattering," Rev. Mod. Phys., vol. 64, pp. 927–960, 1992.

[72] V. Barone, M. Genovese, N. N. Nikolaev, E. Predazzi, and B. G. Zakharov, "Unitarization of structure functions at large 1/x," Phys. Lett. B, vol. 326, pp. 161–167, 1994.

[73] K. J. Golec-Biernat and M. Wusthoff, "Saturation effects in deep inelastic scattering at low Q**2 and its implications on diffraction," Phys. Rev. D, vol. 59, p. 014017, 1998.

[74] J. Kwiecinski, A. D. Martin, and A. M. Stasto, "A Unified BFKL and GLAP description of F2 data," Phys. Rev. D, vol. 56, pp. 3991–4006, 1997.

[75] K. J. Golec-Biernat and M. Wusthoff, "Saturation in diffractive deep inelastic scattering," Phys. Rev. D, vol. 60, p. 114023, 1999.

[76] K. Golec-Biernat and S. Sapeta, "Saturation model of DIS : an update," JHEP, vol. 03, p. 102, 2018.

[77] K. Deja, V. Martinez-Fernandez, B. Pire, P. Sznajder, and J. Wagner, "Prospects for GPDs extraction with Double DVCS," in 29th Cracow Epiphany Conference on Physics at the Electron-Ion Collider and Future Facilities, 4 2023.

[78] H. Moutarde, B. Pire, F. Sabatié, L. Szymanowski, and J. Wagner, "On the importance of gluon contributions to timelike and spacelike DVCS," PoS, vol. DIS2013, p. 220, 2013.

[79] F. Dominguez, B.-W. Xiao, and F. Yuan, "$k_t$-factorization for Hard Processes in Nuclei," Phys. Rev. Lett., vol. 106, p. 022301, 2011.

[80] F. Dominguez, C. Marquet, B.-W. Xiao, and F. Yuan, "Universality of Unintegrated Gluon Distributions at small x," Phys. Rev. D, vol. 83, p. 105005, 2011.

[81] P. Kotko, K. Kutak, C. Marquet, E. Petreska, S. Sapeta, and A. van Hameren, "Improved TMD factorization for forward dijet production in dilute-dense hadronic collisions," JHEP, vol. 09, p. 106, 2015.

[82] E. Iancu and D. N. Triantafyllopoulos, "JIMWLK evolution in the Gaussian approximation," JHEP, vol. 04, p. 025, 2012.

[83] A. van Hameren, P. Kotko, K. Kutak, C. Marquet, E. Petreska, and S. Sapeta, "Forward di-jet production in p+Pb collisions in the small-x improved TMD factorization framework," JHEP, vol. 12, p. 034, 2016. [Erratum: JHEP 02, 158 (2019)].

[84] B.-W. Xiao, "Low-$x$ Physics in $pA$ Collisions and at the EIC," Nucl. Phys. A, vol. 967, pp. 257–264, 2017.

[85] C. Marquet, "A Unified description of diffractive deep inelastic scattering with saturation," Phys. Rev. D, vol. 76, p. 094017, 2007.

[86] E. Iancu and R. Venugopalan, The Color glass condensate and high-energy scattering in QCD, pp. 249–3363. 3 2003.

[87] H. Weigert, "Evolution at small x(bj): The Color glass condensate," Prog. Part. Nucl. Phys., vol. 55, pp. 461–565, 2005.

[88] B.-W. Xiao, F. Yuan, and J. Zhou, "Transverse Momentum Dependent Parton Distributions at Small-x," Nucl. Phys. B, vol. 921, pp. 104–126, 2017.

[89] C. J. Bomhof, P. J. Mulders, and F. Pijlman, "The Construction of gauge-links in arbitrary hard processes," Eur. Phys. J. C, vol. 47, pp. 147–162, 2006.

[90] A. van Hameren, H. Kakkad, P. Kotko, K. Kutak, and S. Sapeta, "Searching for saturation in forward dijet production at the LHC," 6 2023.

[91] T. Altinoluk, R. Boussarie, and P. Kotko, "Interplay of the CGC and TMD frameworks to all orders in kinematic twist," JHEP, vol. 05, p. 156, 2019.

[92] T. Gehrmann, T. Lubbert, and L. L. Yang, "Transverse parton distribution functions at next-to-next-to-leading order: the quark-to-quark case," Phys. Rev. Lett., vol. 109, p. 242003, 2012.

[93] M.-x. Luo, T.-Z. Yang, H. X. Zhu, and Y. J. Zhu, "Quark Transverse Parton Distribution at the Next-to-Next-to-Next-to-Leading Order," Phys. Rev. Lett., vol. 124, no. 9, p. 092001, 2020.

[94] M. A. Ebert, B. Mistlberger, and G. Vita, "Transverse momentum dependent PDFs at N$^3$LO," JHEP, vol. 09, p. 146, 2020.

[95] M.-x. Luo, T.-Z. Yang, H. X. Zhu, and Y. J. Zhu, "Unpolarized quark and gluon TMD PDFs and FFs at N$^3$LO," JHEP, vol. 06, p. 115, 2021.

[96] K. Melnikov, R. Rietkerk, L. Tancredi, and C. Wever, "Triple-real contribution to the quark beam function in QCD at next-to-next-to-next-to-leading order," JHEP, vol. 06, p. 033, 2019.

[97] A. Behring, K. Melnikov, R. Rietkerk, L. Tancredi, and C. Wever, "Quark beam function at next-to-next-to-next-to-leading order in perturbative QCD in the generalized large-$N_c$ approximation," Phys. Rev. D, vol. 100, no. 11, p. 114034, 2019.

[98] K. Melnikov, R. Rietkerk, L. Tancredi, and C. Wever, "Double-real contribution to the quark beam function at N$^3$LO QCD," JHEP, vol. 02, p. 159, 2019.

[99] T. Goda and P. Müllender, "Sector Decomposition Scheme for N$^3$LO Beam Function," Acta Phys. Polon. B, vol. 52, no. 8, p. 947, 2021.

[100] V. Del Duca, C. Duhr, R. Haindl, A. Lazopoulos, and M. Michel, "Tree-level splitting amplitudes for a quark into four collinear partons," JHEP, vol. 02, p. 189, 2020.

[101] S. Catani and M. Grazzini, "Infrared factorization of tree level QCD amplitudes at the next-to-next-to-leading order and beyond," Nucl. Phys. B, vol. 570, pp. 287–325, 2000.

[102] S. Catani, D. de Florian, and G. Rodrigo, "The Triple collinear limit of one loop QCD amplitudes," Phys. Lett. B, vol. 586, pp. 323–331, 2004.

[103] S. Catani, D. de Florian, and G. Rodrigo, "Space-like (versus time-like) collinear limits in QCD: Is factorization violated?," JHEP, vol. 07, p. 026, 2012.

[104] R. Mertig and J. Kublbeck, "Feyn Arts and Feyn Calc: Computeralgebraic generation and calculation of Feynman diagrams for radiative corrections," in International Workshop on Software Engineering, Artificial Intelligence and Expert Systems for High-energy and Nuclear Physics, pp. 565–572, 3 1990.

[105] R. Mertig, M. Bohm, and A. Denner, "FEYN CALC: Computer algebraic calculation of Feynman amplitudes," Comput. Phys. Commun., vol. 64, pp. 345–359, 1991.

[106] J. Kublbeck, M. Bohm, and A. Denner, "Feyn Arts: Computer Algebraic Generation of Feynman Graphs and Amplitudes," Comput. Phys. Commun., vol. 60, pp. 165–180, 1990.

[107] V. Shtabovenko, R. Mertig, and F. Orellana, "New Developments in FeynCalc 9.0," Comput. Phys. Commun., vol. 207, pp. 432–444, 2016.

[108] V. Shtabovenko, R. Mertig, and F. Orellana, "FeynCalc 9.3: New features and improvements," Comput. Phys. Commun., vol. 256, p. 107478, 2020.

[109] M. Czakon, "A novel subtraction scheme for double-real radiation at NNLO," Phys. Lett. B, vol. 693, pp. 259–268, 2010.

[110] A. van Hameren, "PARNI for importance sampling and density estimation," Acta Phys. Polon. B, vol. 40, pp. 259–272, 2009.

[111] W. R. Inc., "Mathematica, Version 13.3." Champaign, IL, 2023.

[112] H. Kowalski and D. Teaney, "An Impact parameter dipole saturation model," Phys. Rev. D, vol. 68, p. 114005, 2003.

[113] A. Kovner and J. G. Milhano, "Vector potential versus color charge density in low x evolution," Phys. Rev. D, vol. 61, p. 014012, 2000.

[114] A. Kovner, J. G. Milhano, and H. Weigert, "Relating different approaches to nonlinear QCD evolution at finite gluon density," Phys. Rev. D, vol. 62, p. 114005, 2000.

[115] E. Iancu, A. Leonidov, and L. D. McLerran, "Nonlinear gluon evolution in the color glass condensate. 1.," Nucl. Phys. A, vol. 692, pp. 583–645, 2001.

[116] J. Jalilian-Marian, A. Kovner, and H. Weigert, "The Wilson renormalization group for low x physics: Gluon evolution at finite parton density," Phys. Rev. D, vol. 59, p. 014015, 1998.

[117] J. Jalilian-Marian, A. Kovner, A. Leonidov, and H. Weigert, "The Wilson renormalization group for low x physics: Towards the high density regime," Phys. Rev. D, vol. 59, p. 014014, 1998.

[118] J. Jalilian-Marian, A. Kovner, A. Leonidov, and H. Weigert, "The BFKL equation from the Wilson renormalization group," Nucl. Phys. B, vol. 504, pp. 415–431, 1997.

[119] J. L. Albacete and Y. V. Kovchegov, "Solving high energy evolution equation including running coupling corrections," Phys. Rev. D, vol. 75, p. 125021, 2007.

[120] J. L. Albacete, N. Armesto, J. G. Milhano, P. Quiroga-Arias, and C. A. Salgado, "AAMQS: A non-linear QCD analysis of new HERA data at small-x including heavy quarks," Eur. Phys. J. C, vol. 71, p. 1705, 2011.

[121] K. Kutak and A. M. Stasto, "Unintegrated gluon distribution from modified BK equation," Eur. Phys. J. C, vol. 41, pp. 343–351, 2005.

[122] M. Derrick et al., "Measurement of the proton structure function F2 at low x and low q**2 at HERA," Z. Phys. C, vol. 69, pp. 607–620, 1996.

[123] J. Breitweg et al., "Measurement of the proton structure function F2 and sigma-tot (gamma* p) at low q**2 and very low x at HERA," Phys. Lett. B, vol. 407, pp. 432–448, 1997.

[124] S. Aid et al., "A Measurement and QCD analysis of the proton structure function f2 (x, q**2) at HERA," Nucl. Phys. B, vol. 470, pp. 3–40, 1996.

[125] C. Adloff et al., "A Measurement of the proton structure function f2 (x, q**2) at low x and low q**2 at HERA," Nucl. Phys. B, vol. 497, pp. 3–30, 1997.

[126] J. Kwiecinski and A. M. Stasto, "Geometric scaling and QCD evolution," Phys. Rev. D, vol. 66, p. 014013, 2002.

[127] K. J. Golec-Biernat and S. Sapeta, "Heavy flavour production in DGLAP improved saturation model," Phys. Rev. D, vol. 74, p. 054032, 2006.

[128] M. A. Kimber, J. Kwiecinski, A. D. Martin, and A. M. Stasto, "The Unintegrated gluon distribution from the CCFM equation," Phys. Rev. D, vol. 62, p. 094006, 2000.

[129] A. H. Mueller, B.-W. Xiao, and F. Yuan, "Sudakov Resummation in Small-$x$ Saturation Formalism," Phys. Rev. Lett., vol. 110, no. 8, p. 082301, 2013.

[130] A. H. Mueller, B. Wu, B.-W. Xiao, and F. Yuan, "Probing Transverse Momentum Broadening in Heavy Ion Collisions," Phys. Lett. B, vol. 763, pp. 208–212, 2016.

[131] A. Prokudin, P. Sun, and F. Yuan, "Scheme dependence and transverse momentum distribution interpretation of Collins–Soper–Sterman resummation," Phys. Lett. B, vol. 750, pp. 533–538, 2015.

[132] P. Sun, J. Isaacson, C. P. Yuan, and F. Yuan, "Nonperturbative functions for SIDIS and Drell–Yan processes," Int. J. Mod. Phys. A, vol. 33, no. 11, p. 1841006, 2018.

[133] T. Goda, K. Kutak, and S. Sapeta, "Sudakov effects and the dipole amplitude," Nucl. Phys. B, vol. 990, p. 116155, 2023.

[134] I. Abt, A. M. Cooper-Sarkar, B. Foster, V. Myronenko, K. Wichmann, and M. Wing, "Investigation into the limits of perturbation theory at low $Q^2$ using HERA deep inelastic scattering data," Phys. Rev. D, vol. 96, no. 1, p. 014001, 2017.

[135] K. Kutak and S. Sapeta, "Gluon saturation in dijet production in p-Pb collisions at Large Hadron Collider," Phys. Rev. D, vol. 86, p. 094043, 2012.

[136] K. Kutak, "Hard scale dependent gluon density, saturation and forward-forward dijet production at the LHC," Phys. Rev. D, vol. 91, no. 3, p. 034021, 2015.

[137] A. van Hameren, P. Kotko, K. Kutak, and S. Sapeta, "Sudakov effects in central-forward dijet production in high energy factorization," Phys. Lett. B, vol. 814, p. 136078, 2021.

[138] L. Motyka, M. Sadzikowski, and T. Stebel, "Lam-Tung relation breaking in $Z^0$ hadroproduction as a probe of parton transverse momentum," Phys. Rev. D, vol. 95, no. 11, p. 114025, 2017.

[139] N. Timneanu, J. Kwiecinski, and L. Motyka, "Saturation model for two photon interactions at high-energies," Eur. Phys. J. C, vol. 23, pp. 513–526, 2002.

[140] J. Lyness, "Integrating some infinite oscillating tails," Journal of Computational and Applied Mathematics, vol. 12-13, pp. 109–117, 1985.

[141] A. Łuszczak, M. Łuszczak, and W. Schäfer, "Unintegrated gluon distributions from the color dipole cross section in the BGK saturation model," Phys. Lett. B, vol. 835, p. 137582, 2022.

[142] B. G. Giraud and R. Peschanski, "Fourier-positivity constraints on QCD dipole models," Phys. Lett. B, vol. 760, pp. 26–30, 2016.

[143] D. Levin, "Development of non-linear transformations for improving convergence of sequences," International Journal of Computer Mathematics, vol. 3, no. 1-4, pp. 371–388, 1972.

[144] E. J. Weniger, "Nonlinear sequence transformations for the acceleration of convergence and the summation of divergent series," Comput. Phys. Rept., vol. 10, no. 5-6, pp. 189–371, 1989.

[145] H. Homeier and E. Weniger, "On remainder estimates for levin-type sequence transformations," Computer Physics Communications, vol. 92, no. 1, pp. 1–10, 1995.

[146] C. W. Clenshaw and A. R. Curtis, "A method for numerical integration on an automatic computer," vol. 2, 12 1960.

[147] K. S. Kolbig, "PROGRAMS FOR COMPUTING THE LOGARITHM OF THE GAMMA FUNCTION AND THE DIGAMMA FUNCTION FOR COMPLEX ARGUMENT," 4 1972.

[148] M. Galassi, J. Davies, J. Theiler, B. Gough, and G. Jungman, GNU Scientific Library - Reference Manual, Third Edition, for GSL Version 1.12 (3. ed.). 01 2009.

[149] T. Hahn, "CUBA: A Library for multidimensional numerical integration," Comput. Phys. Commun., vol. 168, pp. 78–95, 2005.

[150] R. Brun and F. Rademakers, "ROOT: An object oriented data analysis framework," Nucl. Instrum. Meth. A, vol. 389, pp. 81–86, 1997.

[151] F. James, "MINUIT Function Minimization and Error Analysis: Reference Manual Version 94.1," 1994.

[152] F. James and M. Winkler, "MINUIT User's Guide," 6 2004.

[153] A. van Hameren, P. Kotko, K. Kutak, S. Sapeta, and E. Żarów, "Probing gluon number density with electron-dijet correlations at EIC," Eur. Phys. J. C, vol. 81, no. 8, p. 741, 2021.

[154] M. Hentschinski, K. Kutak, and R. Straka, "Maximally entangled proton and charged hadron multiplicity in Deep Inelastic Scattering," Eur. Phys. J. C, vol. 82, no. 12, p. 1147, 2022.

[155] A. van Hameren, "KaTie : For parton-level event generation with $k_T$-dependent initial states," Comput. Phys. Commun., vol. 224, pp. 371–380, 2018.

[156] A. H. Mueller, B.-W. Xiao, and F. Yuan, "Sudakov double logarithms resummation in hard processes in the small-x saturation formalism," Phys. Rev. D, vol. 88, no. 11, p. 114010, 2013.

[157] N. A. Abdulov et al., "TMDlib2 and TMDplotter: a platform for 3D hadron structure studies," Eur. Phys. J. C, vol. 81, no. 8, p. 752, 2021.

[158] I. Balitsky, "Quark contribution to the small-x evolution of color dipole," Phys. Rev. D, vol. 75, p. 014001, 2007.